



---

**Forschungszentrum Karlsruhe**  
in der Helmholtz-Gemeinschaft

---

**Wissenschaftliche Berichte**  
FZKA 7121

# **Theory of Electronic Transport Through Molecular Nanostructures**

**M.B. Köntopp**  
Institut für Nanotechnologie

**Mai 2005**

**Impressum der Print-Ausgabe:**

**Als Manuskript gedruckt  
Für diesen Bericht behalten wir uns alle Rechte vor**

**Forschungszentrum Karlsruhe GmbH  
Postfach 3640, 76021 Karlsruhe**

**Mitglied der Hermann von Helmholtz-Gemeinschaft  
Deutscher Forschungszentren (HGF)**

**ISSN 0947-8620**

**urn:nbn:de:0005-071217**

# Theory of electronic transport through molecular nanostructures

---

## Theorie des Elektronentransports durch molekulare Nanostrukturen

Zur Erlangung des akademischen Grades eines  
DOKTORS DER NATURWISSENSCHAFTEN

der Fakultät für Physik der  
Universität Karlsruhe (TH)  
genehmigte

DISSERTATION

von

Dipl.-Phys. Max B. Köntopp

aus

Karlsruhe

Tag der mündlichen Prüfung:

11. Februar 2005

Referent:

Prof. Dr. Peter Wölfle

Korreferent:

Prof. Dr. Matthias Vojta



## Abstract

The main issue of this work is to describe electronic transport through single molecule junctions. We implemented the “standard” approach to molecular conductance, namely transport calculations in a Landauer–Büttiker framework based on Kohn–Sham orbitals extracted from density functional theory (DFT). Our particular implementation ensures, that apart from approximations inherent in the exchange–correlation functional in DFT no further approximations are made.

Comparison of our numerical calculations with available experimental data shows, that, while in some cases qualitative information on transport can be gained, the experimental conductance is two to three orders of magnitude below the theoretical estimate. Changes in bond geometry can not account for this discrepancy.

We are led to the conclusion that approximations in the exchange–correlation functional may be the major underlying reason for the discrepancy. To this end, we formulated the condition under which the “standard” approach would be exact.

Furthermore, we investigated three situations where despite these shortcomings quantitative results can be obtained. Thereby we, for first time, calculated the step positions in the I–V characteristics of a “diode–type” molecule quantitatively.

## Zusammenfassung

Ziel dieser Arbeit ist die Beschreibung des Elektronentransports durch Einzelmoleküle. Als erstes wird die Implementierung der derzeitigen *Standard*–Methode zur parameterfreien Beschreibung des elektronischen Transports durch Moleküle vorgestellt: Basierend auf effektiven Ein–Teilchen Orbitalen (Kohn–Sham Orbitalen) aus DFT Rechnungen, wird der Leitwert unter Verwendung des Landauer–Büttiker Formalismus berechnet. Die hier verwendete spezielle Implementierung hat den besonderen Vorteil, dass, abgesehen von den Näherungen im verwendeten DFT Austausch–Korrelationsfunktional, keine weiteren Näherungen gemacht werden.

Der Vergleich von Modellrechnungen an zwei Molekülen, zu denen experimentelle Daten vorliegen, zeigt, dass zwar in manchen Fällen qualitativ richtige Resultate erzielt werden können, der theoretisch berechnete Leitwert jedoch zwei bis drei Größenordnungen über den experimentell gemessenen Werten liegt. Änderungen der Bindungsgeometrie können diese Diskrepanz nicht erklären.

Aufgrund dieser Ergebnisse vertreten wir die Auffassung, dass Näherungen innerhalb des Austauschkorrelationsfunktionals ein wesentlicher Grund für diese Diskrepanz zwischen Theorie und Experiment sind. Daher haben wir untersucht, unter welchen Bedingungen eine exakte Formulierung der Methode möglich ist.

Des weiteren haben wir drei Situationen untersucht, in denen wir mittels DFT–basierten Rechnungen quantitative Ergebnisse erzielen können. Hierbei ist es uns insbesondere gelungen, erstmals die Position der Stufen in der Strom–Spannungs–Kennlinie eines Moleküls quantitativ zu berechnen.

---

# Deutsche Zusammenfassung

Bauelemente eines integrierten Schaltkreises auf einem handelsüblichen Mikrochip haben zur Zeit typische Abmessungen von ca. 100 nm. Wenn man annimmt, dass sich das gegenwärtige Tempo, mit dem die Miniaturisierung vorangetrieben wird, auch in Zukunft durchhalten lässt, dann werden in 12 Jahren Abmessungen von nur noch 10 nm erreicht sein. Eine darüber hinausgehende Miniaturisierung ist nur möglich, wenn es gelingt, Schaltelemente aus einzelnen Atom- oder Molekülkomplexen zu konstruieren (Molekulare Elektronik). Die Erforschung von Molekülen und molekularen Drähten z.B. im Bezug auf ihre Eigenschaften als elektrische Leiter und Schaltelemente ist daher nicht nur von fundamentalem wissenschaftlichen Interesse sondern auch technologisch geboten.

Die funktionalen Eigenschaften — insbesondere solche die mit dem Ladungstransport zusammenhängen — eines kontaktierten, d.h. chemisch an die Elektroden gebundenen, Moleküls lassen sich nicht unabhängig von der Natur des Kontaktes verstehen. Das ist leicht einzusehen, wenn man bedenkt, dass nur Hybride aus Molekül- und Elektrodenzuständen den Strom leiten können, da nur diese die eine mit der anderen Elektrode verbinden. Daher muss eine vollständige Beschreibung des Transportes auch die Zuleitungen mit einbeziehen. Hier liegt eine der Herausforderungen in der Beschreibung des elektronischen Transports durch Einzelmoleküle.

Eine zweite Herausforderung ist eng damit verknüpft, dass auf dem Molekül die Coulombwechselwirkung der Elektronen untereinander die Energie und die räumliche Gestalt der elektronischen Zustände wesentlich mitbestimmt. Korrelationseffekte spielen eine viel größere Rolle als beispielsweise in einfachen Metallen und müssen ebenfalls mit in die Theorie einbezogen werden.

Zur Zeit stellt die Dichtefunktionaltheorie (DFT) die einzige praktikable Methode dar, mit der man gleichzeitig zumindest einen Teil der wichtigen Korrelationseffekte berücksichtigt, sowie eine ausreichende Zahl an Elektronen in

die Rechnung einbeziehen kann, um die Ankopplung makroskopischer Zuleitungen richtig zu beschreiben.

Die vorliegende Arbeit wurde motiviert durch den enormen Einfluss, den solche *ab initio* basierte Rechnungen in der Molekularen Elektronik voraussichtlich haben werden. Die zur Zeit drängendste theoretische Frage auf dem Gebiet ist die große Diskrepanz zwischen theoretischen Vorhersagen und tatsächlich gemessenen Leitwerten von Einzelmolekülen. Die Werte unterscheiden sich oft um mehrere Größenordnungen.

Als erstes wurde in dieser Arbeit die derzeitige *Standard*-Methode zur parameterfreien Beschreibung des elektronischen Transports durch Moleküle implementiert: Basierend auf effektiven Ein-Teilchen Orbitalen (Kohn-Sham Orbitalen) aus DFT Rechnungen, wird der Leitwert unter Verwendung des Landauer-Büttiker Formalismus berechnet. Die hier vorgestellte spezielle Implementierung hat den besonderen Vorteil, dass, abgesehen von den Näherungen im verwendeten DFT Austausch-Korrelationsfunktional, keine weiteren Näherungen gemacht werden. Insbesondere können wir eine ausreichende Anzahl von Elektrodenatomen in die Rechnung einbeziehen um eine korrekte Extrapolation in den thermodynamischen Limes sicherzustellen.

Mit dem implementierten Formalismus wurden zwei Modellrechnungen anhand von Molekülen, zu denen experimentelle Daten vorliegen, durchgeführt: Benzol-dithiol sowie ein größeres, auf Anthrazin aufbauendes Molekül. Die dabei gewonnenen wichtigsten Schlussfolgerungen sind:

- Im Fall des größeren Moleküls liefern Rechnungen das qualitativ (und für die Peakpositionen auch quantitativ) richtige Resultat.
- Der theoretisch berechnete Leitwert liegt zwei bis drei Größenordnungen über den experimentell gemessenen Werten, in Übereinstimmung mit Rechnungen anderer Gruppen. Die Verbreiterung der Molekülzustände durch die Ankopplung an die Zuleitung wird stark überschätzt.
- Änderung der Bindungsgeometrie, die oft als ein möglicher Grund für die gefundenen Abweichungen angeführt werden, haben nur einen geringen Einfluss: Ändert man z.B. den Bindungsabstand, den Bindungswinkel, die Anzahl der Atome an die der Schwefel bindet, usw. innerhalb physikalisch vernünftiger Grenzen, so sind die damit verbundenen Leitwertänderungen viel zu klein um die Abweichungen zu erklären.

Aufgrund dieser Ergebnisse vertreten wir die Auffassung, dass Näherungen innerhalb des Austauschkorrelationsfunktionals ein wesentlicher Grund für diese Diskrepanz zwischen Theorie und Experiment sind. Daher haben wir

untersucht, unter welchen Bedingungen eine exakte Formulierung der Methode möglich ist: Dies ist nur im quasi-statischen Grenzfall unter Verwendung des exakten (nicht-Gleichgewichts-) Austauschkorrelationsfunktionals der *zeitabhängigen* DFT gegeben. Jedoch wird in den zur Zeit im Feld der molekularen Elektronik durchgeführten Rechnungen ein Gleichgewichtsfunktional benutzt, meist im Rahmen der *Lokalen* Dichte Näherung (LDA). Bei Verwendung dieses Funktionals werden viele wichtige, nichtlokale Effekte vernachlässigt. In einer Beispielsrechnung mit Hartree-Fock Orbitalen statt der DFT Wellenfunktionen haben wir gezeigt, dass diese Effekte für den Transport von großer Bedeutung sein können. So ergibt sich durch die exakte Berücksichtigung der Austauschwechselwirkungs-Effekte, die das Selbstwechselwirkungsproblem der DFT vermeidet, eine realistischere Beschreibung der Verbreiterung der Molekülzustände. Allerdings ist dies mit einem großen Qualitätsverlust bei den Resonanzenergien aufgrund fehlender Korrelationseffekte in der Hartree-Fock Beschreibung verbunden.

Leider sind zur Zeit keine besseren, praktikablen Funktionale verfügbar, die Korrelationseffekte, den exakten Austauschterm sowie weitere langreichweitige Effekte enthalten. Wir müssen deshalb fragen, in welchen Situationen wir mittels DFT basierten Rechnungen dennoch quantitative Ergebnisse für den Stromtransport durch einzelnen Moleküle gewinnen können. Dazu haben wir drei Beispielsfälle untersucht, in denen dies erfolgreich möglich ist:

- **Einfluss der Symmetrie auf den Stromtransport**

Moleküle können ausgeprägte Symmetrieeigenschaften aufweisen. Insbesondere wenn der Stromtransport entlang des Schnittes von zwei Symmetrieebenen erfolgt, kann die Art der Ankopplung des Moleküls an die Elektroden großen Einfluss haben: Falls die Stromeinkopplung diese Spiegelsymmetrie verletzt (indem z.B. der Schwefel als Bindeglied zu den Elektroden in einem Winkel zur Symmetrieachse sitzt) wird die Ankopplung und damit der gemessene Leitwert stark reduziert. Wir haben ein solches Beispiel mittels unserer DFT Rechnungen untersucht und Ergebnisse in sehr guter Übereinstimmung mit den experimentellen Daten erhalten.

- **Auswirkungen externer Parameter**

DFT-Rechnungen mit Gleichgewichtsfunktional erlauben es, die Veränderung der Elektronendichte unter Einfluß eines externen Parameters, wie z.B. einer Gate-Spannung zu untersuchen. Wenn die Energie eines Molekülzustands durch die Gate-Spannung den Wert der Fermi-Energie passiert kann sich die Elektronendichte auf dem Molekül stark ändern. Diese "Resonanzen" in der Zustandsdichte sind mit einem deutlich erhöhten Stromfluss durch das Molekül verbunden. Auf diese Weise

ist es möglich, trotz der Verwendung eines Gleichgewichtsfunktionals, exakte Ergebnisse für die Oszillation der Leitfähigkeit mit der Gatespannung zu erhalten. Die Untersuchung solcher Coulomb-Blockade Effekte haben wir anhand eines Beispielmoleküls (Benzol-dithiol) demonstriert.

- Verschiebung der Molekülzustände durch Polarisierung  
Eine weitere Anwendung dieser Methode besteht darin, zu untersuchen, wie sich die Kohn-Sham Zustände des Moleküls verschieben, wenn man eine endliche Spannung anlegt. Es ist uns so gelungen, für das "Diodenmolekül" aus Abbildung 1.1 die Position von sieben der neun niedrigsten Stufen in der gemessenen Strom-Spannungscharakteristik quantitativ zu berechnen. Dies ist nach unserem Wissen das erste Mal, dass der "Leitwert-Fingerabdruck" eines Moleküls in einer Transportmessung quantitativ berechnet werden konnte.

Da bisher noch nicht abzusehen ist, wie die Fortschritte im Bereich der Entwicklung besserer Funktionale für die Dichtefunktionaltheorie in der nächsten Zeit aussehen werden, ist es sinnvoll, mehrere verschiedene Strategien gleichzeitig zu verfolgen, um Fortschritte in der theoretischen Beschreibung der Transporteigenschaften von Einzelmolekülen zu machen:

- Implementierung von derzeit verfügbaren Austauschkorrelationsfunktionalen mit nichtlokalen Anteilen und Vergleich der Ergebnisse mit Experimenten und anderen Rechnungen.
- Untersuchen, ob es weitere experimentelle Transporteigenschaften gibt, die sich im Rahmen der Gleichgewichtsfunktionale berechnen lassen. Dies könnten z.B. Phononenfrequenzen oder Oszillatorstärken sein.
- Hybrid-Methoden: Verknüpfung von exakten Methoden wie *Configuration Interaction* oder CC2, angewandt auf das "nackte" Molekül mit DFT Rechnungen für das kombinierte System Molekül plus Elektroden.

Insgesamt gesehen werden noch viele Forschungsbeiträge aus Numerik, Theorie und Experiment nötig sein, bis ein umfassendes Verständnis des Stromtransports durch Moleküle erreicht ist und ein systematisches Design von funktionalen molekularen Schaltelementen möglich wird.

# Contents

<b>Deutsche Zusammenfassung</b>	<b>iii</b>
<b>1 Introduction</b>	<b>1</b>
1.1 Molecular electronics . . . . .	1
1.2 About this work . . . . .	4
<b>2 Experimental techniques</b>	<b>7</b>
2.1 History: pioneering ideas and experiments . . . . .	7
2.2 Mechanically controlled break-junctions (MCBJ) . . . . .	8
2.3 Electromigration . . . . .	10
2.4 Electrochemical techniques . . . . .	11
2.4.1 Electrochemical etching . . . . .	11
2.4.2 Electrochemical deposition . . . . .	12
2.5 Molecular monolayer devices . . . . .	13
2.5.1 Langmuir-Blodgett films . . . . .	13
2.5.2 Self-assembled monolayers (SAM) . . . . .	14
2.6 STM experiments . . . . .	14
2.6.1 Single-molecule device structured on a STM tip . . . . .	16
2.7 Crossed wire devices . . . . .	17
2.8 Nanopores . . . . .	17
<b>3 Molecular transport based on Density Functional Theory</b>	<b>19</b>

3.1	Introduction . . . . .	19
3.2	Landauer–Büttiker transport formalism . . . . .	20
3.2.1	Non–interacting electrons . . . . .	20
3.2.2	Landauer formula with Green’s–functions . . . . .	24
3.2.3	Interacting electrons: the Meir–Wingreen formula . . . . .	29
3.3	Transport through single molecules: our implementation . . . . .	31
3.3.1	The matrix equations . . . . .	31
3.3.2	Self–energies and Green’s–functions from DFT . . . . .	34
<b>4</b>	<b>Density Functional Theory (DFT)</b>	<b>41</b>
4.1	Introduction: why do we need DFT? . . . . .	41
4.2	Hohenberg–Kohn theorems . . . . .	43
4.2.1	Hohenberg–Kohn theorem I . . . . .	43
4.2.2	Hohenberg–Kohn theorem II . . . . .	45
4.3	Kohn–Sham equations . . . . .	47
4.4	Extensions: Spin Density Functional Theory (SDFT) . . . . .	50
4.5	The derivative discontinuity . . . . .	51
4.6	Practical implementation of the Kohn–Sham scheme in TURBOMOLE . . . . .	53
4.6.1	Optimized basis sets for DFT . . . . .	54
4.6.2	Effective core potentials . . . . .	56
4.6.3	The use of fractional occupation numbers to improve convergence . . . . .	56
4.7	Different approximations for DFT functionals . . . . .	57
4.7.1	Local Density Approximation (LDA) . . . . .	58
4.7.2	Beyond LDA: Generalized Gradient Approximation (GGA) . . . . .	59
4.7.3	Extensions: exact exchange and hybrid functionals . . . . .	61
4.7.4	Functionals used within this work . . . . .	62

---

4.8	Physical quantities given exactly in Density Functional Theory . . . . .	63
4.9	Other quantities . . . . .	64
4.10	Time-dependent Density Functional Theory (TD-DFT) . . . . .	65
4.10.1	Runge-Gross theorem . . . . .	66
4.10.2	Time-dependent Kohn-Sham equations . . . . .	66
4.10.3	Adiabatic approximation (ALDA) . . . . .	67
<b>5</b>	<b>Testing our implementation</b>	<b>69</b>
5.1	Band structure of a gold cluster from DFT — testing a tight-binding representation . . . . .	69
5.2	The conductance of atomic wires of gold . . . . .	71
<b>6</b>	<b>DFT-based transport calculations: numerical results and comparison to experiments</b>	<b>77</b>
6.1	Benzene . . . . .	78
6.2	Symmetric, anthracene-based molecule . . . . .	83
6.3	Influence of stress on the conductance . . . . .	85
6.3.1	Sulfur-gold bond distance $d$ . . . . .	86
6.3.2	Tilting the molecule: angle $\beta$ between molecule and gold . . . . .	87
6.3.3	Rotating the molecule: angle $\alpha$ . . . . .	88
6.3.4	Strong distortion of the coupling geometry . . . . .	89
6.3.5	Summary . . . . .	90
6.4	Influence of the sulfur-gold coupling: coupling to 1, 2 and 3 Au atoms . . . . .	90
6.5	Conclusions . . . . .	94
<b>7</b>	<b>Exact description of transport within TD-DFT and Landauer-Büttiker theory for interacting electrons</b>	<b>95</b>
7.1	Transport properties in LDA and Hartree Fock . . . . .	95
7.2	Exact transport formalism using TD-DFT . . . . .	99

7.3	Time-dependent DFT in the quasistationary limit and scattering formalism . . . . .	102
<b>8</b>	<b>Symmetry and transport</b>	<b>109</b>
8.1	Motivation . . . . .	109
8.2	<i>Para</i> and <i>meta</i> couplings and the conductance . . . . .	109
8.2.1	Numerical conductance calculations . . . . .	111
8.2.2	Structure of the molecular orbitals . . . . .	113
8.2.3	Experimental results . . . . .	114
8.2.4	Summary . . . . .	116
<b>9</b>	<b>Three terminal devices: describing a gate electrode</b>	<b>117</b>
9.1	Motivation and idea . . . . .	117
9.2	How the gate is realized within DFT . . . . .	122
9.2.1	Implementation . . . . .	122
9.2.2	Finding the right geometry . . . . .	123
9.3	Results and discussion . . . . .	128
<b>10</b>	<b>Transport through a molecular double dot system</b>	<b>131</b>
10.1	Motivation . . . . .	131
10.1.1	The Aviram-Ratner diode . . . . .	131
10.1.2	Reasons for an asymmetric I-V characteristics . . . . .	133
10.2	Molecular double quantum dot system . . . . .	138
10.2.1	Design of the molecule . . . . .	139
10.2.2	Experimental results . . . . .	140
10.2.3	Double dot system: principle mechanism . . . . .	142
10.2.4	Evolution of the Kohn-Sham levels . . . . .	144
10.2.5	Peak positions in the I-V characteristics . . . . .	148
10.2.6	Discussion . . . . .	150
10.2.7	Summary . . . . .	152

<b>11 Conclusions</b>	<b>153</b>
11.1 Summary . . . . .	153
11.2 Outlook . . . . .	155
<b>A The Meir–Wingreen Formula</b>	<b>157</b>
Lebenslauf	161
Danksagung	163
List of Figures	164
References	168



# Chapter 1

## Introduction

### 1.1 Molecular electronics

Currently, commercially manufactured active components of integrated circuits (e.g., transistors) have typical dimensions of about 100 nanometers. Assuming the current rate of miniaturization can also be achieved in the future, device dimensions of only 10 nanometers will be reached in about 12 years. Smaller active elements can only be realized, if one manages to make use of the atomistic structure of matter. Then, active devices will have to be built up of single atom or molecule complexes.

The computer manufacturer Hewlett–Packard has already taken a first step in this direction: in the year 2006, an innovative memory chip is announced to be sold commercially. Data bits in this chip will be stored using molecules, organized in self-assembled monolayers (of about 1000 molecules). Further miniaturization of such a memory chip can be achieved by using less and less molecules to store the information. In principle, a single molecule would be sufficient. From this point of view, the concept of a computer, where the integrated circuits are, at least partially, realized by (macro-) molecules, loses its futuristic character. In consequence, the scientific investigation of molecules and molecular wires with respect to their properties for possible use for data storage or as building blocks for electronic devices in general is not only of fundamental scientific interest but also of large technological relevance.

The carrier, most easily controlled in molecular systems, is the electrical charge. Hence, a rapidly growing number of research groups worldwide is concentrating for now on the measurement of current–voltage curves (I–Vs) that, ideally, offer a precise fingerprint of the investigated molecules. Single molecules of dimensions of only a few nanometers can be contacted using,

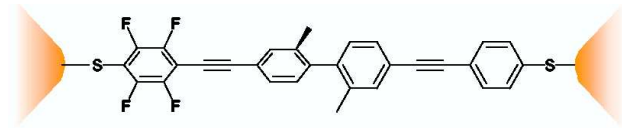


Figure 1.1: Schematic view of a molecule designed to act as a diode in between two gold contacts. (Design and synthesis by M. Elbing and M. Mayor [1].)

e.g., the *mechanically controlled break-junction technique*: a lithographically produced, thin gold bridge is broken by controlled mechanical deformation, resulting in an open contact where the electrode distance can be adjusted with sub-Ångström precision, so that single molecules can be contacted. Fig. 1.1 depicts a molecule (designed by M. Mayor and M. Elbing, INT) where the I–V characteristics have been obtained in a break-junction experiment (by H. Weber and R. Ochs, INT), see fig. 1.2 [1]. The current increases in a stepwise fashion with the applied bias voltage. These steps are a fingerprint of the energy levels of the molecule, which, one after the other, enter the voltage window opened by the applied bias and give an individual contribution to the current.

A lot of the physics, relevant to the understanding of charge transport through single molecules, can be borrowed from the mesoscopic physics of quantum dots. In fact, a molecule chemically bound to two electrodes is nothing else

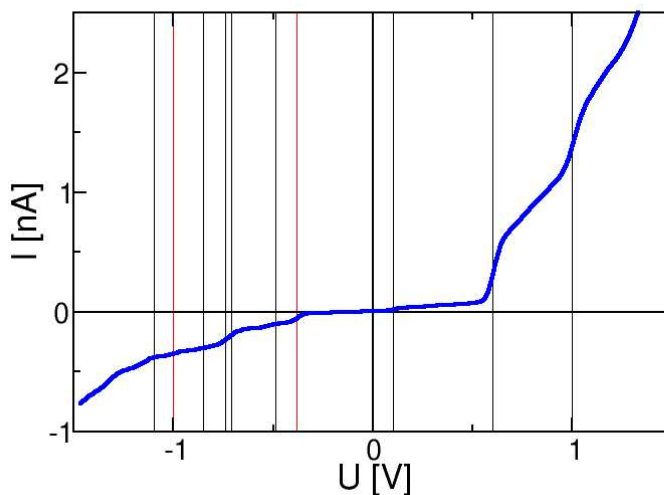


Figure 1.2: Experimentally measured current voltage characteristics of the molecule shown in fig. 1.1 [1]. Vertical lines indicate the theoretical prediction for the step positions based on a methodology developed in the present work.

but a particular realization of a quantum dot. Physical concepts like resonant and off-resonant transmission through individual energy levels of the molecule, sequential tunneling, Coulomb-blockade and even correlation driven physics like the Kondo-effect apply to molecular transport as well as to quantum dots in a very similar manner.

This list of aspects of physics important to transport in molecular structures is by no means exhaustive, however, as molecules are a very special kind of quantum dot: typical molecules that have been investigated are at least one order of magnitude smaller than the smallest “conventional” quantum dot systems. In other words, molecules are quantum dots in new and possibly very interesting parameter regimes. Furthermore, molecules can exhibit exact geometrical symmetry properties which can lead to analogues of *selection rules* for quantum transport. Moreover, molecules tend to have relatively flexible structures. Therefore, in general, the coupling of electronic degrees of freedom to the atomic “lattice” structure of the molecule should be quite strong. In particular, an electron-rotor coupling and a strong electron-vibron coupling exists, which can result in polaron formation. This is quite unusual compared to the situation in conventional quantum dots. Finally, molecular structures can be designed at will, offering an almost unlimited playground not only for exotic physical effects, but also for functionality. As an example we only mention the field of *molecular magnetism* where genuine many body effects can be studied in custom tailored systems, that at the same time may also offer functionality for information processing.

All physical phenomena listed above can be subsumed under the heading of *Molecular Electronics*.

## **Transport theory for molecular electronics based on DFT**

Transport properties of a contacted molecule, chemically bound to the electrodes, cannot be understood without taking into account the properties of the contact itself. Obviously only those orbitals, connecting one electrode with the other, can contribute to the current. These states are thus hybridized orbitals built up of molecular states in combination with states in the leads. In consequence, a complete description of transport must also include the properties of the leads. This is one of the challenges that lie ahead of us.

A second challenge stems from the Coulomb interaction of the electrons on the molecule, which strongly influences the energy as well as the spacial structure of the electronic states on the molecule. Correlation effects are far more important in a molecular system than in simple metals and have to be included in the theoretical description of transport through molecules.

In order to predict the parameters relevant for the transport properties of an individual molecule, like the energy levels and their broadening, these challenges — the full many body problem together with the thermodynamic limit — have to be met simultaneously and on the same footing. This is why transport calculations for single molecules turn out to be so difficult.

At present, density functional theory (DFT) is the only method that a) can incorporate (at least some of) the important parts of the correlation physics governing the excitation spectrum of the molecule and b) can deal with sufficiently many electrons to allow for a reliable extrapolation to the thermodynamic limit. Therefore, DFT based transport calculations have become *the* standard tool in the field of molecular electronics.

## 1.2 About this work

### Motivation and goals

Although DFT-based transport calculations have proven to be quite useful in the past, e.g., for understanding the conductance of single atom contacts, they are still far from perfect. In fact, up to now reproducible, quantitative results for molecular wires with an experimental conductance below  $0.1 g_0$  (where  $g_0$  is the quantum of conductance,  $2e^2/h$ ) have never been obtained, so far, and even a qualitative agreement with the experimental current-voltage (I-V) characteristics can not always be achieved. Arguably, understanding the reasons underlying this discrepancy — which in some cases can exceed two orders of magnitude — and how to fix this problem are at present the two most pressing issues in the field of theoretical molecular electronics. Furthermore, without a theoretical description allowing to reliably predict the response properties of molecules including transport, it is hard to imagine how a *systematic* design of functional molecules can be achieved.

In this work we set out in order to make a contribution to resolve these fundamental issues. Let us emphasize already at this point that a full solution cannot be obtained in a single shot. We will see in our analysis, that DFT based transport calculations yield conductance values that differ the more from the experimental data the better the extrapolation procedure is, that takes one into the thermodynamic limit. Amongst other, possibly also experimental reasons, the quality of the DFT functionals used in standard calculations has to be questioned. Therefore, really solving the puzzle necessarily implies to improve, but also to go beyond computational issues and deal with the full many body problem in depth.

## Outline

We will begin our work with a brief review of experimental works and techniques. Thereby we will focus on methods for contacting single or small assemblies of molecules.

In the subsequent chapter 3 we will describe the present “standard method” for DFT based conductance calculations, which is (basically) a Landauer–Büttiker theory in Green’s function formulation based on Kohn–Sham orbitals and energies. The latter are obtained from a standard calculation based on DFT. We will present in detail our implementation of the method. In order to remind to what DFT calculations can provide reliably, and which practices do not have a firm foundation based on the Hohenberg–Kohn theorems, we give a brief summary of the basics of DFT in chapter 4. In particular, we will emphasize there, that a proper treatment of the non-equilibrium situation requires — strictly speaking — the use of time dependent (TD)DFT.

In chapter 5 we will describe how our implementation has been tested against other known results. Thereafter, in chapter 6, we apply our machinery to two molecules and analyze the transmission in great detail. The selected molecules have also been thoroughly studied experimentally. The most important findings of this section are twofold: a) the experimental conductance is several orders of magnitude below its value based on the standard DFT approach. b) changing the microscopic parameters of the DFT calculations, like bonding angle, bond length etc., in reasonable limits does not bring down the DFT-conductance by orders of magnitude.

The numerical findings of chapter 6 motivate an analysis of the approximations in the exchange–correlation functional that has been used in the DFT procedure. In chapter 7 we will demonstrate that any functional local in the electron density (like LDA, GGA etc.) is going to miss the corrections that account for the difference between the true density (and current) response of the molecule and its “Kohn–Sham–response”. The exact exchange–correlation functional is known to be non–local in the density however, and by means of an exemplary Hartree–Fock calculation we can show that including non–localities can indeed decrease the conductance by an order of magnitude or more.

Unfortunately, at the moment transport calculations with non–local exchange–correlation functionals are not feasible, even with advanced DFT codes like TURBOMOLE. Therefore, we have to consider for practical purposes, whether some limited aspects of the results from the standard (equilibrium) DFT calculations for transport can actually be trusted. The next three chapters (8–10) will deal with cases where the answer to this question is yes: in chapter 8 we will

show that symmetry related aspects of transport can be described qualitatively in a correct way.

In chapter 9, we will go beyond qualitative aspects and argue, that a *parametrical* dependence of the conductance, e.g. the peak distance of Coulomb oscillations (the peak height cannot be obtained this way), can be given (in principle) exactly even by an *equilibrium* DFT calculation. As an illustration we calculate the dependence of the transmission of benzene-1,4-di-thiol on an external gate voltage.

A somewhat unorthodox application of the same idea will be given in chapter 10. Here, we will consider the parameter to be the external voltage bias and analyze, how the energy levels of the molecule in fig. 1.1 shift when the gate voltage is tuned. This procedure will allow us to identify those voltages at which level crossings occur, that leave a step as their signature in the current-voltage characteristics. The vertical lines plotted in fig. 1.2, which fit the experimentally observed step positions almost perfectly well, have been obtained this way.

Finally, we conclude our work in chapter 11 with a more detailed summary of the results obtained together with future perspectives.

# Chapter 2

## Experimental techniques

In this chapter we will give a brief overview over some of the numerous techniques used to measure the conductance of organic molecules. A detailed discussion of all methods of this very diverse, and fast growing field is beyond the scope of this thesis. We will only describe a selection of popular methods.

Our main focus will be on single-molecule methods as these offer the best insight into the underlying transport mechanisms. Several different approaches exist to measure conductance through a single molecule, each one offering specific advantages. But note, that so far, none of them can be viewed as a “standard method” to contact single molecules and all are far away from being implemented on an industrial scale to yield commercial devices. Contacting and manipulating single molecules on the nanometer scale in a reliable and reproducible fashion still constitutes a scientific challenge.

### 2.1 History: pioneering ideas and experiments

Historically, the field of molecular electronics experiments started off in the late 60s with experiments on Langmuir–Blodgett films (see below), done by Kuhn and Möbius [3].

A few years later, Aviram and Ratner [4] published their pioneering paper suggesting in a *Gedankenexperiment* how to realize a single-molecule diode. The proposed design consisted of a donor and acceptor part of the molecule, divided by a tunneling barrier, see chapter 10 for further discussion.

But due to the limited experimental methods on the nanoscale available at that time, no further progress in the field was made. Only recently, after techniques like scanning tunneling microscopy and nanofabrication techniques had been developed, it became possible to really contact single molecules.

The breakthrough was reported by M. Reed *et al.* in 1997 [5]: using the *mechanically controlled break-junction technique* a single molecule was contacted in between the tips of a broken gold bridge and current-voltage curves were recorded. This experiment started off an enormous experimental effort in the field, resulting in the development of many different techniques some of which we will present in the next sections.

## 2.2 Mechanically controlled break-junctions (MCBJ)

The use of mechanically controlled break-junctions (MCBJ) [6, 7] for contacting single molecules is a further development of single-atom contact conductance experiments [8–10]. In these experiments, metal wires are elongated until they break. Shortly before breaking, the diameter of the smallest constriction reduces to one single atom and—in the case of gold—further elongation yields an atomic chain of gold atoms until the wire finally breaks.

The design principle of MCBJ devices is simple: a thin gold film is structured, using e-beam lithography, on an elastic substrate. The substrate usually consists of phosphor bronze covered by a few  $\mu\text{m}$  of polyimide for insulation between gold and substrate. The gold film is designed to have a constriction of 50 by 50 nanometers. By underetching this constriction, a freestanding bridge is created, see fig. 2.1, (a).

At the INT, the following protocol is applied to contact single molecules: the obtained chip, about  $15 \times 7 \text{ mm}^2$  in size, is placed in a bending mechanism as depicted in fig. 2.1,(b) and (c). The three-point geometry of the bending mechanism allows for a very precise control of the bending. To avoid contaminations, the bending mechanism is placed in a vacuum chamber (pressure  $10^{-7} - 10^{-8}$  mbar). The pushing rod is moved upward until the bridge breaks. Due to the conversion of the upward movement into a bending of the substrate, the distance between the two ends of the broken gold wire can be controlled with 0.1 Ångström precision. Now, the contact is opened and closed repeatedly until quantized conductance values are observed, corresponding to the formation of an atomic point contact, i.e. the contact ends are now atomically sharp.

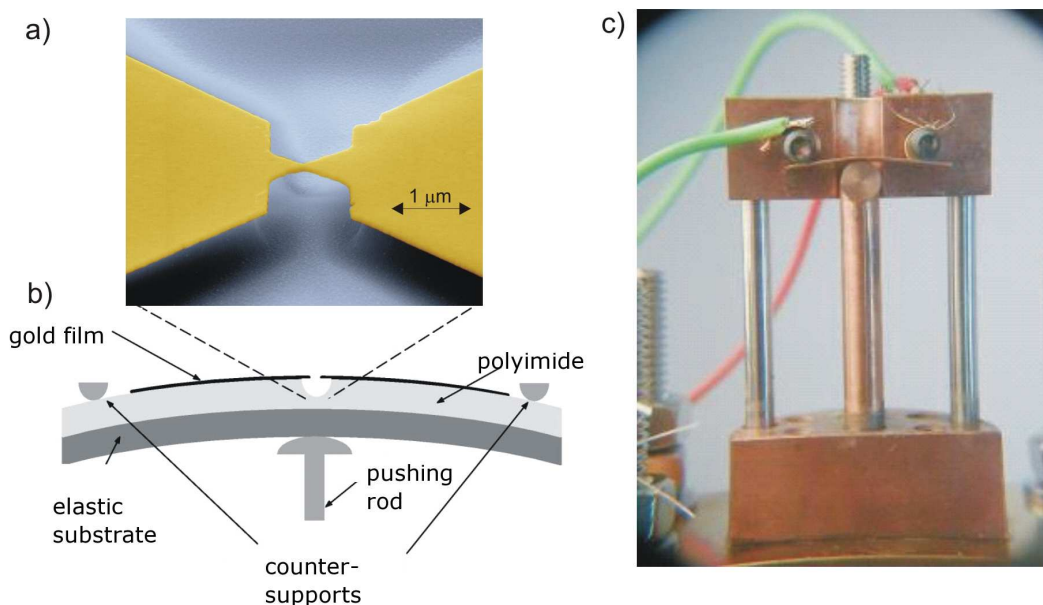


Figure 2.1: (a) Scanning electron microscope (SEM) image of a freestanding (underetched) gold bridge used for a MCBJ experiment. (b) Schematic representation of the MCBJ setup. (c) Image of the experimental setup. The counter-supports are visible in the upper part (black) holding the sample (thin bronze sheet).

Then, the chamber is filled with nitrogen and a diluted solution of the molecule (with acetyl-protected terminal thiol groups) to be measured is applied on the opened contact. The acetyl group prevents the molecules from forming clusters and only deprotects in contact with the gold forming a stable covalent bond between the sulfur and the gold, see section 6.4 for details. Some of the molecules will lose their acetyl protection group and the sulfur will chemically bond to one electrode. To remove molecules that are not chemically bonded to the gold, the junction is rinsed with the solvent THF. After evacuation, the bridge is slowly closed with a bias voltage applied. Due to the small distance between the electrodes, a high electric field is present, in which the molecules orient themselves towards the opposite electrode. At one point, the first molecules will reach the second electrode and chemically bond to it. This situation can be recognized by a plateau in the current. Now, current-voltage curves can be recorded. Some results of conductance measurements at our institute will be discussed in §6.

One disadvantage of the MCBJ technique is the difficulty in obtaining low-temperature measurements: the electrode distance changes when the sample is cooled down, thereby breaking the contact. Also, devices requiring a gate

electrode can not be constructed using break-junctions. Due to the large diameter of the breaking wire, electric fields are effectively screened and can not penetrate to the molecule in the junction, see also chapter 9. But apart from this, break-junctions offer the best control for single-molecule experiments.

In consequence, a large amount of experiments are reported using this technique [5, 11–19]

## 2.3 Electromigration

Devices fabricated by electromigration offer the possibility to study the influence of a gate electrode.

Usually, a 10 to 15 nm wide wire is fabricated on a  $SiO_2$  insulating layer using e-beam lithography [20]. A doped Si substrate underneath the  $SiO_2$  can be used as a gate electrode. After adding a solution of the molecules to be investigated onto the wire, the single-molecule contact is then created by breaking the wire through electromigration: at low temperature the applied bias voltage is increased to large values until the wire breaks.

This produces a gap of about 1 to 2 nanometers, across which in about 10 % of the samples a molecule is found, so that I-V characteristics can be recorded [16].

Using the electromigration technique, J. Park *et al.* [16] managed to observe Kondo effect and Coulomb blockade effects in single molecules consisting of a Co ion trapped in a polypyridyl cage, see fig. 2.2, see also chapter 9.

For the longer, less conducting molecule, a conductance gap for small bias voltages was observed. In dependence of the gate voltage, different threshold bias values were necessary until the current increased, corresponding to Coulomb blockade behavior. 2D plots of conductance in dependence of applied bias and gate voltage yielded Coulomb diamonds.

In case of the shorter molecule, where the Co-ion acted as an “impurity spin” a Kondo resonance was observed: at zero bias, a peak in the differential conductance is reported, that has a logarithmic temperature dependence between 3 K and 20 K. As a second test, a magnetic field was applied which resulted in a split of the peak, as would be expected from Kondo physics.

A second group, H. Park *et al* [21], also observed a Kondo resonance in single molecules using electromigration techniques to contact the molecules.

There are many other experiments that make use of the electromigration technique to contact single molecules, e.g., [20, 22–24]

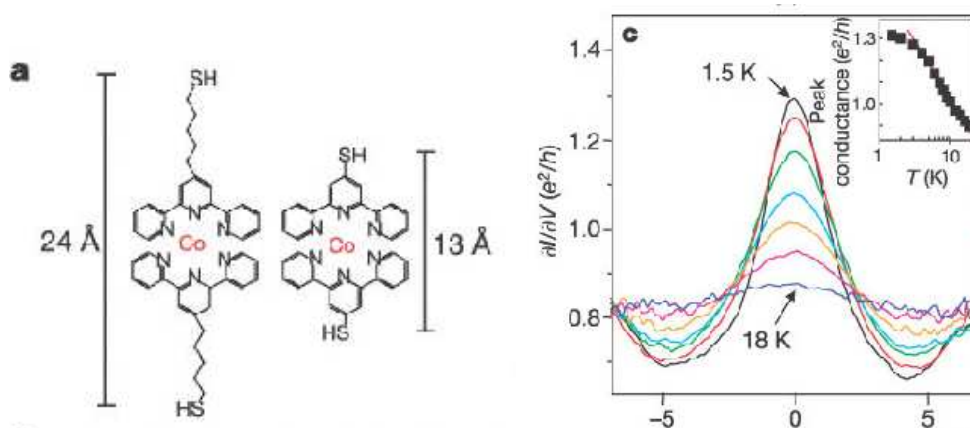


Figure 2.2: Kondo effect in a single molecule device. Experiment by J. Park *et al.* [16] using electromigration contacts. Left: Molecules investigated, consisting of a Co ion trapped in a cage of benzene rings. Right: Observed Kondo peak in the shorter molecule. Displayed is the differential conductance over bias voltage in V. Different traces correspond to different temperatures. The inset shows the decrease of the peak height with temperature.

## 2.4 Electrochemical techniques

### 2.4.1 Electrochemical etching

The electrochemical etching technique is an excellent technique to fabricate gated single-molecule junctions. The use of very thin planar electrodes allows the incorporation of a gate only a few nanometers away from the electrode [25,26]. The device fabrication consists of two major steps: evaporation of the contact structure, and electrochemical etching of the gold to form a nanogap, see fig 2.3.

On top of an aluminum gate electrode, covered with about 2 nm aluminum oxide, the contact geometry is defined using e-beam lithography [25]. After evaporation of a thin adhesion layer of titanium, the gold electrodes are deposited. In the central region of the contact, only a very thin ( $\approx 15$  nm) gold layer is deposited using shadow evaporation techniques.

Then, the actual nanogap is formed by electrochemical etching: using a counter-electrode in a bath of  $\text{KAuCN}_2$ , the thin gold layer is etched and a gap forms. The gap distance is measured via the tunneling current between the electrodes during the etching process.

Using this method, it was possible to fabricate nanogaps with sub-Ångström precision in the electrode distance, where at the same time the gate electrode

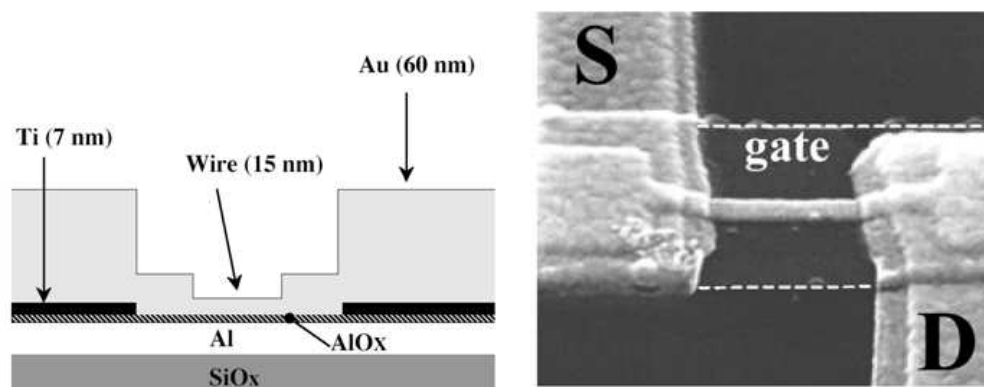


Figure 2.3: Gated single-molecule contact: electrochemical etching technique. Device by Kervennic *et al.* [25, 26]. Left: schematic representation of the sample before electrochemical etching. The gate electrode (Al) is separated from the contact by a thin aluminum oxide layer. The 15 nm thin wire region is obtained by small-angle evaporation of gold. Right: SEM picture of the sample. S and D denote the source and drain electrode.

is only a few nanometers away from the molecule. Kervennic *et al.* reported the observation of a gate effect in organic molecules using this technique [26]. The experiment will be discussed in more detail in chapter 9.

## 2.4.2 Electrochemical deposition

A second electrochemical method can be used to structure nanogaps for single-molecule measurements: by electrochemical deposition of gold, a gap of desired length can be produced [27].

The process is relatively simple. Two electrodes with a relatively large separation ( $\approx 25 \mu\text{m}$ ) are lithographically structured on a substrate. Then the device is put in an electrolyte and a voltage is applied between the electrodes. In consequence, gold atoms are etched off from one electrode and deposited on the other, thereby decreasing the gap width. By measuring the current between the contacts, the distance can be estimated and the process is terminated, when the desired distance is reached [27].

Several measurements of single molecules using electrochemical deposition have been reported [28, 29].

## 2.5 Molecular monolayer devices

Molecular film devices are far easier to produce than single-molecule experiments. The device consists of a monolayer of molecules, with the substrate acting as one of the electrodes. The second electrode is then either evaporated on, yielding a film device, or a STM tip is used as the second electrode, resulting in a single-molecule device (which will be discussed in the next section §2.6).

Due to their simplicity in the fabrication, film devices are promising candidates for first real-life applications of molecular electronics in the near future. However, in case of film devices, a controlled deposition of the second electrode is a difficult task. The monolayer can be damaged during the process. Although working devices are achieved in most cases, the actual microscopies of the measured device (structural integrity of the monolayer, defects) is not clear [30]. Several devices based on sandwiching molecular films between two electrodes have been reported [31–35].

Different techniques can be applied to produce a molecular monolayer: Langmuir–Blodgett films and self-assembled monolayers.

### 2.5.1 Langmuir–Blodgett films

Langmuir–Blodgett films [36] are obtained by pulling a chip covered with a hydrophilic substrate (e.g. metals like Al, Cr) out of a solution containing a monolayer of molecules. The technique is depicted in fig. 2.4.

The organic molecules have to contain a hydrophilic group, e.g. acid or alcohol group, and a hydrophobic group, usually an aliphatic chain, to allow film formation on the surface of water (*Langmuir film*). In water, all molecules will then align in the same direction with the hydrophilic end at the water side. A continuous monolayer, which can later be transferred on the substrate is formed by compression of the film using a movable barrier. The substrate is slowly removed from the bath while at the same time the barrier is shifted to keep the monolayer intact. This way, a well-ordered monolayer of the organic molecule is formed on the surface of the substrate.

The big disadvantage of this method is, that the molecules are not chemically bond to the substrate, as a hydrophilic group is required on the substrate side of the molecule and thus thiol endgroups can not be used.

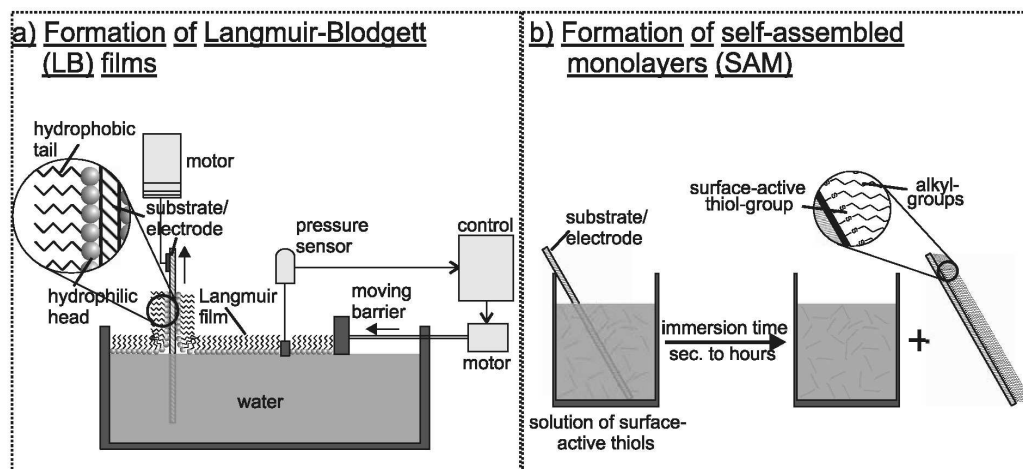


Figure 2.4: Obtaining molecular film devices. Left: Technique to obtain Langmuir-Blodgett films. Right: How self assembled monolayers are obtained. From [31]

## 2.5.2 Self-assembled monolayers (SAM)

For self-assembled monolayers, the technique is simpler, and chemical bonds to the substrate can and have to be achieved. The spontaneous arrangement of (organic) molecules on a surface to, ideally, defect-free structures is called self-assembly. Here, the monolayer forms from molecules in solution on the substrate itself, due to the properties of the molecules [31]. See [37] for a review on the formation of SAMs.

Usually SAMs are obtained by dipping the substrate, later used as one of the electrodes in the conductance experiment, into a dilute solution of the molecules to be measured. These do in general have an end group that binds covalently to the metal of the substrate on one side. After a layer has formed, the substrate is removed from the solution, see fig. 2.4. The second electrode can then be evaporated on top of the molecular layer. Many measurements molecular sandwich devices using SAMs have been reported [16, 32, 33, 35, 38–40].

## 2.6 STM experiments

Using monolayer film devices, it is also possible to conduct measurements on single molecules. A scanning tunneling microscope (STM) tip is used as second electrode. Often films, consisting of a matrix of spacer molecules plus

the molecules to be measured are used. By using these smaller, insulating molecules (usually based on alkyl chains) as spacers, the molecules of interest are separated spatially from each other enhancing the probability to contact a single molecule with the STM tip.

As di-thiol SAMs (with sulfur groups on both ends) are difficult to produce, the molecules can usually only be chemically bound to the substrate, the second contact then is a tunneling contact. In consequence, STM based single-molecule measurements always have strongly asymmetric coupling to the electrodes, which makes interpretation of the experimental data more complicated.

The first demonstration of a single-molecule measurement based on STM techniques was done by Bumm and Tour [41]. Here, longer molecules consisting of several benzene rings in a SAM with shorter, insulating molecules as spacers, were contacted using the STM tip. The molecules were covalently bound to the substrate via thiol groups, whereas the contact to the STM tip was a tunneling contact. Since then, many other STM based conductance measurements have been reported [15, 31, 38, 42, 42].

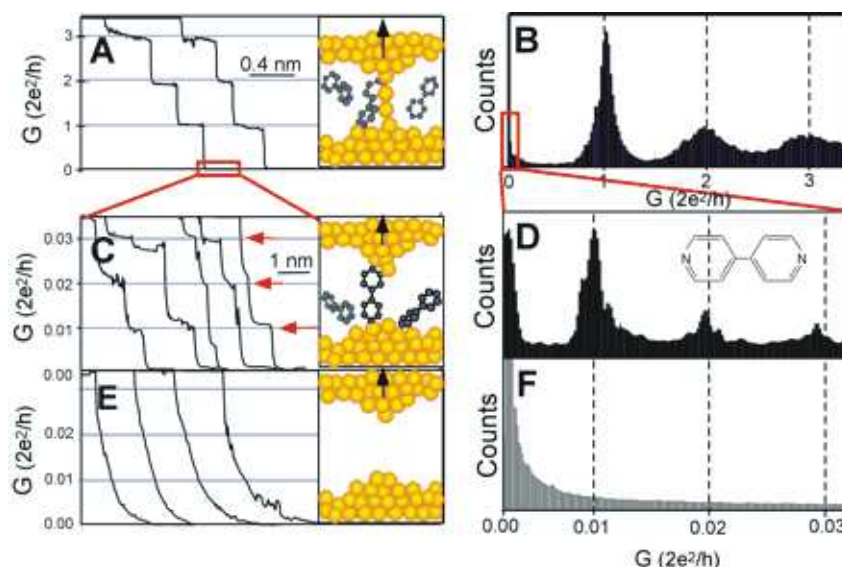


Figure 2.5: Measurement of the conductance of bipyridine using an STM tip, from [42]. The repeated formation of single-molecule junctions makes the statistical analysis of conductance measurements possible.

Left: current over electrode displacement during two stages of opening the contact. A) atomic wire, B) conductance of molecules, C) control experiment without molecules.

Right: Statistical analysis of the conductance values.

In 2003, *Tao* and coworkers developed a method that allows the repeated formation of molecular junctions using a gold STM tip in fast succession [42].

The STM tip is moved into and out of contact with a gold substrate in a solution containing the sample molecules. When the tip is pulled out of contact, a stepwise decrease in the conductance is observed, see fig. 2.5. These steps are the usual conductance steps observed in metallic point contacts (see §5.2). When the tip is pulled out further, additional plateaus appear, corresponding to a resistance two orders of magnitude higher. By statistical analysis it was possible to attribute these steps to the measurement of a distinct number of molecules between the contact.

### 2.6.1 Single-molecule device structured on a STM tip

A completely different approach to achieve single-molecule contacts based on STM tips has been reported by Zhitenev *et al.* [43]: the fabrication of the single-molecule device on the STM tip itself.

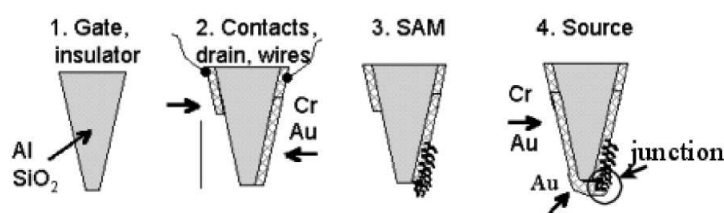


Figure 2.6: Single molecule device fabricated on a STM tip, from [43]. Schematic of the fabrication process. The contact is formed by evaporating electrodes on two sides of a square-shaped STM tip. The contact is formed by evaporating gold from underneath the electrode after the molecules have been applied.

Using a STM tip of square shape (about 20–30 nm diameter), the two electrodes were evaporated on two sides of the tip, see fig. 2.6. Then, the tip can be dipped into a solution of thiol-terminated molecules that will bond to the electrodes. To form the actual contact, gold is evaporated from underneath the tip while the conductance of the contact is monitored. Evaporation is stopped, when conductance values suggest, that a stable contact with one or a few molecules has formed.

This method offers one special advantage: in STM based experiments, the sample can be cooled down to low temperatures, which makes the measurement of vibrational modes or electron-phonon interaction possible. In other approaches, cooling often is a problem.

Zhitenev *et al.* observed vibrational modes in molecules consisting of thiophene rings [43].

## 2.7 Crossed wire devices

A different promising technique is based on crossed wires: Kushmerick *et al.* [44,45] reported the conductance measurement of small assemblies of molecules using two crossed wires of about  $10\ \mu\text{m}$  diameter as depicted in fig. 2.7 to contact the molecules.

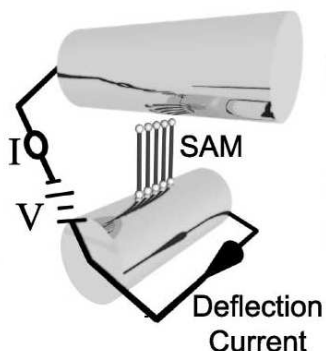


Figure 2.7: Schematic representation of the crossed wire setup to measure the conductance of small assemblies of molecules. A SAM is applied to one of the wires. The distance of the wires is controlled by the Lorentz force caused by running a deflection current through the wires, [44].

Thereby, a SAM is applied on one of the wires. The distance of the second wire, perpendicular to the first one, is controlled via the Lorentz force caused by a small current ( $< 5\ \text{mA}$ ) through the wire. This way, the two wires can be approached to each other until the molecules of the SAM come in contact with the second wire.

Using this technique, I–Vs of organic molecules consisting of several benzene rings, were reported [44].

## 2.8 Nanopores

Nanopores promise the possibility to measure a very small assembly of molecules—far less than in a monolayer device. In the same year they published their break-junction experiment, Zhou and Reed [46] also presented the first results of molecule conductance measurements using nanopores.

The nanopore is a very small hole which is etched into a freestanding silicon nitride layer by reactive ion etching. After the etching process, gold is evaporated onto the hole from underneath, then a SAM is allowed to form on the

evaporated gold. Finally, titanium and gold are evaporated from above to yield the molecular device, see fig. 2.8.

The big advantage of using nanopore contacts is their stability, the samples can for example be cooled down without problems. The big disadvantage is the same as for all monolayer devices, it is not clear how the SAM is damaged in the second evaporation step. Also it is unclear, how the titanium interacts with the molecules.

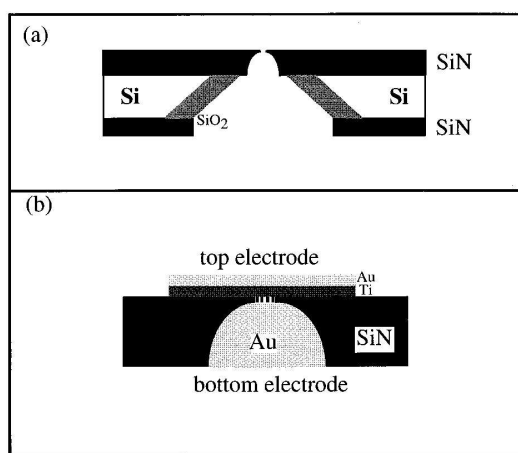


Figure 2.8: Schematic representation of a nanopore device for the measurement of small assemblies of organic molecules. From Zhou *et al.* [46]. Top: empty device. Bottom: device after the molecules have been applied and the top and bottom electrodes have been deposited.

However, several experiments on the conductance of molecules using nanopores have been reported [46–53].

# Chapter 3

## Molecular transport based on Density Functional Theory

### 3.1 Introduction

The idea behind the “standard” approach of DFT based transport calculations is, to construct scattering states from the Kohn–Sham orbitals of the DFT calculation and combine those with the Landauer–Büttiker scheme. The concept of DFT will be described later, in chapter 4.

The Landauer–Büttiker approach to transport is based on the concept to view the conductance through a mesoscopic system as a scattering process. Possible scatterers include an atomic point contact, a quantum dot, an atomic wire or a molecule. Electrons are injected into and extracted from the wire/contact with ballistic leads. All required information about the *dc*-transport properties is encoded in the scattering matrix of the contact. The Landauer–Büttiker formula [54, 55] then expresses the conductance in terms of transmission amplitudes through the scattering region.

In the following section, we will revisit the ideas behind the Landauer–Büttiker transport description. We will discuss in detail its practical application to molecular systems in the noninteracting case and to a lesser extend to interacting systems, where we will describe the Meir–Wingreen approach (§3.2.3) using the non-equilibrium Green’s-function formalism (NEGF). Then, our implementation of calculating transport through single molecules in the scattering approach will be presented. In chapter 7, we will come back to the NEGF formalism to discuss our results on the range of applicability and on the limitations of the DFT approach in describing transport through mesoscopic contacts.

## 3.2 Landauer–Büttiker transport formalism

### 3.2.1 Non-interacting electrons

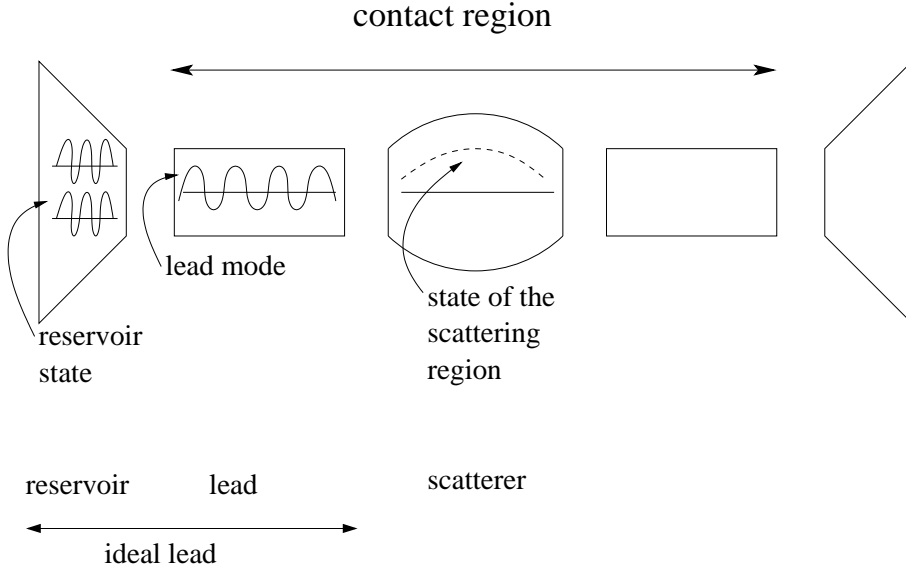


Figure 3.1: Schematic representation of a mesoscopic contact. In the contact region the lead has the width  $w$ , limiting the number of transverse modes.

The Landauer formula [56, 57] allows to express the transport of non-interacting electrons through a mesoscopic scattering region (e.g., a molecule) in terms of its transmission function  $T(E)$  and the Fermi distribution functions of the connected leads. A schematic representation of the contact is given in fig.3.1.

For a strictly one-dimensional system, where the transverse dimensions  $w$  of the leads are small enough such that only the lowest transverse eigenstate is occupied, resulting in only one conduction channel, the conductance,  $G$ , at zero bias takes the form

$$G = \frac{2e^2}{h} T(E_F).$$

$T$  thereby is the probability with which an electron entering from one side is transmitted through the scattering region to the other side with an energy equal to the Fermi energy,  $E_F$ . Assuming perfect transmission ( $T = 1$ ) the conductance takes the value of the quantum of conductance

$$G_0 = \frac{2e^2}{h} = 77.48 \mu S \quad (3.1)$$

(which is per definition the conductance of one single, perfect channel with two degenerate spin states). Eq. 3.1 can be generalized to leads involving

more than one transverse eigenstate below the Fermi energy, leading to the well known formulation of the Landauer–Büttiker formula [54, 55].

The derivation of the Landauer–Büttiker formula, even for non-interacting electrons, is nontrivial. Baranger and Stone [58] together with others clarified its relation to the Kubo formula, and the regime where they are equivalent. In section §3.2.3 we will describe its derivation from the Keldysh formalism, where the validity is extended beyond the linear response regime. Several key conceptual ideas are required:

- The leads are considered to be ideal Fermi liquids. Electrons entering the contact region from the left or right have a distribution according to the Fermi distribution  $f_l, f_r$  at the time-independent chemical potentials  $\mu_l, \mu_r$  in the left and right lead, respectively.
- The reservoirs are reflectionless. An electron can exit from the contact region into the reservoirs with no probability of reflection — it will be “swallowed” completely.
- Transport is coherent. There is no inelastic scattering in the contact, dissipation takes place only in the reservoirs. In an actual experiment, the role of reservoirs is assumed to be taken over by the leads.

With these assumptions we will now sketch the derivation of the formula, relating conduction to transmission using scattering states for the multi-channel, non-interacting case.

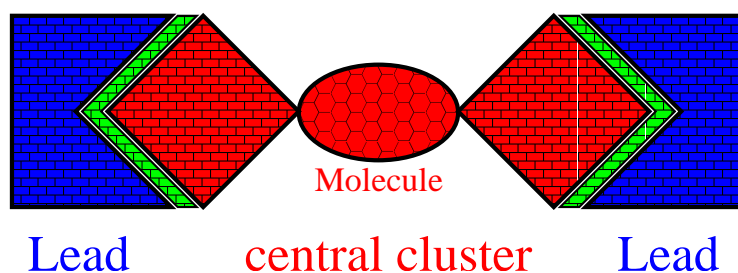


Figure 3.2: Schematic representation of the mesoscopic contact, consisting of the ideal, semi-infinite leads (blue) and the central cluster (red). The coupling between leads and cluster is depicted in green.

The Hamiltonian of our system can be partitioned into three subsystems: left and right lead  $H_L, H_R$ , and the central cluster/molecule  $H_C$ . Figure 3.2 depicts a schematic contact.

It then takes the following form

$$H = \begin{pmatrix} H_L & t_l^\dagger & 0 \\ t_l & H_C & t_r \\ 0 & t_r^\dagger & H_R \end{pmatrix}. \quad (3.2)$$

$H_{L,R}$  describe noninteracting electrons in the left and right leads which are assumed to be perfect ballistic conductors.  $t_l$  and  $t_r$  describe the coupling between the leads and the central cluster. It is assumed, that there is no direct coupling between the two leads.

We will now introduce scattering states to describe the transmission through the molecule. The assumption of perfectly conducting leads assures that the scattering states moving from the left lead to right have a longitudinal momentum  $k$  and a band or channel index  $n$ . The variable  $k$  is continuous as we consider an open system with semi-infinite leads, so that the spectrum of the leads is smooth. The channel index  $n$  stems from the quantization of the transverse momentum due to the finite width  $w$  of the lead. A right moving scattering state  $\Psi_{nk}$  can thus be written as

$$\Psi_{nk}(x, \mathbf{x}_\perp) = \begin{cases} e^{ikx} \chi_n(\mathbf{x}_\perp) + \sum_{n'} \hat{r}_{n'n} e^{-ik'x} \chi_{n'}(\mathbf{x}_\perp) & \text{(in the left lead)} \\ \sum_{n'} \hat{t}_{n'n} e^{ik'x} \chi_{n'}(\mathbf{x}_\perp) & \text{(in the right lead).} \end{cases} \quad (3.3)$$

where  $k, k' > 0$  (and  $k, k' < 0$  for left moving scattering states — moving out of the right lead towards the left lead).  $\hat{t}_{n'n}$  is the probability for the state in channel  $n$  in the left lead to be transmitted into channel  $n'$  in the right lead, whereas  $\hat{r}_{n'n}$  is the respective reflection probability. The wavenumbers are fixed by energy conservation under the condition that there is no inelastic scattering, thus for the energies applies  $\varepsilon_{nk} = \varepsilon_{n'k'}$ . The wavefunction component in transverse direction ( $\mathbf{x}_\perp$ ) is expressed by  $\chi_n(\mathbf{x}_\perp)$ .

To calculate the transport properties we need the transmission coefficients  $\hat{t}_{rl}$  where the wavevector  $k$  is fixed by  $E = \varepsilon_r(k') = \varepsilon_l(k)$ , describing now the probability of an electron at the energy  $E$  entering from the left lead with quantum numbers  $l = (n, k)$  to pass through the scattering region and end up in the right lead in a state  $r = (n', k')$ . With these coefficients, the current can be calculated: the contribution of the initial state  $|\Psi_{kn}\rangle = |\Psi_l\rangle$  to the current is proportional to

$$\sum_r |\hat{t}_{rl}|^2 v_r, \quad (3.4)$$

where we sum over all final states  $r$  keeping  $\varepsilon_{n'k'} = \varepsilon_{nk}$ , fixed. The factor  $v_r = d\varepsilon_{n'k'}/dk'$  is due to the fact that the current is proportional to the square of the wavefunction,  $|\Psi|^2$ , times the velocity,  $v_{n'k'} = v_r$ .

To retrieve the usual formulation of the Landauer formula, we need to express the contribution to the current in terms of the incoming particle flux, whereas

eq. 3.4 is normalized with respect to the volume. Therefore we rescale the transmission coefficients

$$t_{rl} = \left( \frac{v_{n'}}{v_n} \right)^{1/2} \hat{t}_{rl}. \quad (3.5)$$

Now,  $|t_{rl}|^2$  constitutes the fraction of the inflowing current in the left lead which is transmitted into the right lead. The next step is to write down the contribution to the current,  $dI$ , injected on the left side in channel  $n$  with a wavenumber between  $k$  and  $k + dk$ , which is transmitted to the right lead:

$$dI = dk \frac{2e^2}{h} v_n \sum_{n'} |t_{n'n}|^2 \quad (3.6)$$

Here, again, we have to sum over all channels  $n'$  in the right lead with the energy  $\varepsilon_{n'k'} = \varepsilon_{nk}$ .

Using  $v_n(k) = d\varepsilon_{kn}/dk|_{k(E)}$ , this transforms into the transmitted current which originates from incoming states with energies between  $E = \varepsilon_{nk}$  and  $E + dE$ . This yields for the transmission

$$T(E) = \frac{dI}{dE} = \frac{2e^2}{h} \sum_{nn'} |t_{n'n}|^2 = \frac{2e^2}{h} \text{Tr}(\mathbf{t}\mathbf{t}^\dagger). \quad (3.7)$$

Usual transport experiments in mesoscopic physics or molecular electronics do not obtain the transmission directly. Instead, the zero bias conductance is measured,

$$G = \left. \frac{dI}{dV} \right|_{V=0}, \quad (3.8)$$

which is the linear response of the combined system consisting of leads and molecule to an applied external voltage, evaluated at zero voltage. Here, the total current  $I$  is just given by the current originating from states from the left lead, as we are at zero temperature and thus there is no contribution from the right in the energy window between the chemical potentials of the two leads. For energies below the chemical potential of both leads, the contributions of the respective leads cancel each other.

The *Landauer Formula* then just constitutes the fact, that the conductance,  $G$ , equals the transmission,  $T$ , evaluated at the Fermi energy

$$G = T(E_F) \quad (3.9)$$

in units of  $\frac{2e^2}{h}$ .

To look at finite bias in the linear response regime and at zero temperature, we have to integrate  $T(E)$  over the energy  $E$  to obtain the current in the Landauer description

$$I = \int_{\mu_l}^{\mu_r} dE T(E) \quad (3.10)$$

$\mu_l$  and  $\mu_r$  denote the chemical potentials in the left and right lead, respectively. The application to finite temperatures and finite bias in the noninteracting case will be described in section §3.2.3. The Landauer formula has been applied successfully to many different problems like universal conductance fluctuations, Anderson localization, integer quantum Hall effect ...

Assuming only perfectly transmitting channels, one would expect a conductance of exactly the quantum of conductance times the number of occupied transverse states. The first experimental verification of conductance steps by changing the number of channels was done in a *Quantum Point Contact* [59], using a 2-D electron gas (2DEG) formed of a GaAs–AlGaAs heterostructure. In the system, the width of the constriction of the 2DEG could be controlled by applying a gate voltage. With increasing width, the number of occupied transverse states increases which leads to an increase in conductance in steps of the quantum of conductance  $G_0$ , as the channels are perfectly transmitting ( $T = 1$ ). Experimental data of the original experiment is shown in fig. 3.3

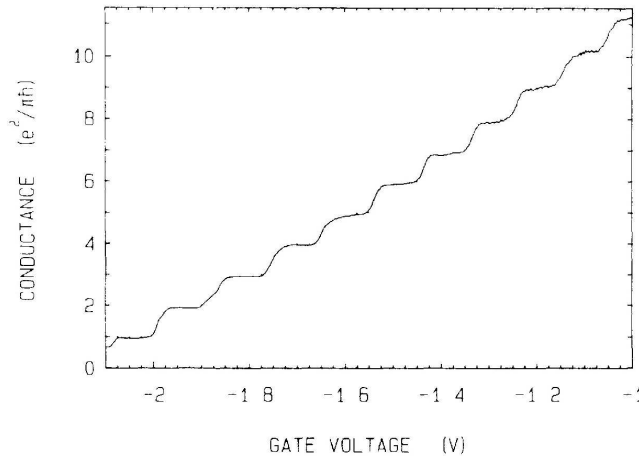


Figure 3.3: Observation of conductance steps in a quantum point contact. Original data by van Wees *et. al* [59]. Using a gate voltage, the number of occupied transverse states is changed, leading to a change in the number of perfectly transmitting channels and thereby to steps of  $2\frac{e^2}{h}$  in the conductance.

### 3.2.2 Landauer formula with Green’s–functions

In our transport calculations the electronic structure of the scattering region is obtained from Density Functional Theory (DFT). DFT yields the ground–state effective single–particle Kohn–Sham wavefunctions. These are stationary states in a cluster Hilbert–space, whereas we would need scattering states defined in the infinite Hilbert–space of the leads to use the Landauer formalism. The underlying concept of DFT will be explained in chapter 4.

Green’s–functions are a convenient concept to relate the stationary states of the DFT calculation to the scattering description. By rewriting the Landauer formula in terms of Green’s–functions, we can construct the scattering states implicitly. In addition, the Green’s–function technique allows us to incorporate the continuum character of the leads (thus dissipative mechanisms) into the discrete set of states of the central cluster through the damping. A first orientation about the concept of the Landauer–formula in Green’s functions is given in [60, 61].

First, we introduce the concept of the scattering matrix  $S$ , which we need in order to do the transformation. The scattering matrix relates states of an incoming wave-packet of the leads to outgoing states after the interaction with the scattering region. If we consider a Hamiltonian  $H = H_0 + H'$ , the  $S$ –matrix quantifies the probability amplitude for a scattering transition from an initial incoming plane wave eigenstate  $|nk\rangle$  of the Hamiltonian  $H_0$  (as described above),

$$\langle \mathbf{x} | nk \rangle = e^{ikx} \chi_n(\mathbf{x}_\perp), \quad (3.11)$$

to a final state  $|n'k'\rangle$  of this Hamiltonian after the perturbation  $H'$  has acted on it. This can be written using the time–evolution operator  $U(t', t) = \exp(iH(t' - t))$  as

$$\langle n'k' | \hat{S} | nk \rangle = \lim_{t_f \rightarrow \infty} \lim_{t_i \rightarrow -\infty} \langle n'k'(t_f) | U(t_f, t_i) | nk(t_i) \rangle. \quad (3.12)$$

The transmission coefficients  $\hat{t}_{n'n}$  are related to the  $S$ –matrix by

$$\hat{t}_{n'n} = \int_{-\infty}^{\infty} dk' \langle n'k' | S(\varepsilon_{nk}) | nk \rangle. \quad (3.13)$$

(Specifications for the directions of the  $k$ –vectors are not needed, as the  $S$ –matrix automatically selects the correct sign for  $k, k'$  for the incoming and outgoing states in both leads.)

We can rewrite expression (3.13) by using the following identity for the  $S$ –matrix (see e.g. [62]):

$$\langle n'k' | \hat{S} | nk \rangle = \delta_{n'k', nk} - 2i\pi \delta(\varepsilon_{n'k'} - \varepsilon_{nk}) \langle n'k' | T(\varepsilon_{nk} + i\eta) | nk \rangle. \quad (3.14)$$

This results in a golden rule type expression which, due to the definition of the transmission matrix,  $T$ , is exact:

$$\hat{t}_{n'n} = -2i\pi \int dk' \delta(\varepsilon_{nk} - \varepsilon_{n'k'}) \langle n'k' | T(\varepsilon_{nk} + i\eta) | nk \rangle \quad (3.15)$$

As we only consider elastic scattering,  $E = \varepsilon_{nk} = \varepsilon_{n'k'}$ , the evaluation of the  $\delta$ –function gives

$$\hat{t}_{n'n} = -2i\pi v_{n'}^{-1} \langle n'k' | T(E) | nk \rangle \quad (3.16)$$

Now, as in the section above, we need to normalize the coefficients  $\hat{t}_{n'n}$  with respect to the incoming particle flux in order to recover the familiar form of the Landauer formula:

$$|t_{n'n}|^2 = (2\pi)^2 (v_n v_{n'})^{-1} |\langle n'k' | T(E) | nk \rangle|^2 \quad (3.17)$$

With  $v_{n'} = \frac{d\epsilon_{n'k'}}{dk'}$  we rewrite this, using  $\delta$ -functions, as

$$|t_{n'n}|^2 = (2\pi)^2 \int dk dk' \delta(E - \epsilon_{nk}) \delta(E - \epsilon_{n'k'}) |\langle n'k' | T(E) | nk \rangle|^2 \quad (3.18)$$

where the energy  $E = \epsilon_{nk}$  as above. Then, summing up the contributions of the different states, a formula for the total transmission  $T(E)$  can be constructed, where in matrix notation, the two diagonal sub-matrices of the Hamiltonian for the left and right lead,  $\mathbf{H}_{L,R}$ , enter instead of the energies  $\epsilon_{nk}$ .

$$T(E) = (2\pi)^2 \text{Tr} [\delta(\mathbf{E} - \mathbf{H}_L) \mathbf{T} \delta(\mathbf{E} - \mathbf{H}_R) \mathbf{T}^\dagger] \quad (3.19)$$

The trace has to be taken over all states in the left lead, ( $\mathbf{E} = E \cdot \mathbf{1}$ ).

To arrive at the Green's-function formulation of the Landauer formula, it remains to replace the  $T$ -matrix by its representation in terms of the retarded Green's-function for the central contact region,  $G_C$ . This way we will be able to write down the transmission as a trace over the Hilbert space of the central cluster which is of *finite* dimension, in contrast to the infinite-dimensional Hilbert space of the combined system of cluster plus leads.

The Hamiltonian matrices for the leads are of infinite dimension. But the coupling matrices,  $t_L, t_R$ , if we consider a representation in a basis of localized atomic orbitals, have non-zero elements only for a small number of orbitals. Namely those, belonging to atoms near the contact region, where the wavefunctions significantly overlap with the wavefunctions of the central cluster. See fig. 3.2, where the coupling layers are depicted in green.

In our Green's-function formulation, the influence of the coupling to the leads will enter in the full Green's-function of the central cluster only through self-energies. These will be of finite dimension due to the finite contributing region. Then, all information on the transport properties of the individual molecule will be contained in the Green's-function of the central cluster and numerical calculations can be performed within this finite set. Thus the calculation of this central cluster Green's-function, that involves the inversion of  $(\mathbf{E} - \mathbf{H}_C)$  becomes achievable.

With our Hamiltonian from eq. 3.2 divided into

$$\mathbf{H}_0 = \begin{pmatrix} H_L & 0 & 0 \\ 0 & H_C & 0 \\ 0 & 0 & H_R \end{pmatrix} \quad \mathbf{H}' = \begin{pmatrix} 0 & t_L^\dagger & 0 \\ t_L & 0 & t_R \\ 0 & t_R^\dagger & 0 \end{pmatrix} \quad (3.20)$$

the  $\mathbf{T}$ -matrix is defined by [62]

$$\mathbf{T}(E) = \mathbf{H}' + \mathbf{H}'\mathbf{G}(E)\mathbf{H}'. \quad (3.21)$$

The following definitions are needed to do the last transformation:

- The unperturbed retarded Green's-functions of the leads and central cluster:

$$\mathbf{g}_{L,R} = (\mathbf{E} - \mathbf{H}_{L,R} + i0)^{-1}; \quad \text{and} \quad \mathbf{g}_C = (\mathbf{E} - \mathbf{H}_C + i0)^{-1}$$

- The self energies in  $\mathbf{g}_C$  that account for the coupling of the leads to the central cluster:

$$\mathbf{\Sigma}_L = \mathbf{t}_L \mathbf{g}_R \mathbf{t}_L^\dagger \quad \text{and} \quad \mathbf{\Sigma}_R = \mathbf{t}_R \mathbf{g}_L \mathbf{t}_R^\dagger$$

- The central block of the full Green's-function:

$$\langle c | \mathbf{G}_C | c' \rangle = \langle c | (\mathbf{E} - \mathbf{H})^{-1} | c' \rangle$$

where  $|c\rangle$  and  $|c'\rangle$  are states of the central cluster. This can be obtained from the self energies and the unperturbed Green's-functions of the central cluster via

$$\mathbf{G}_C = [1 - \mathbf{g}_C(\mathbf{\Sigma}_L + \mathbf{\Sigma}_R)]^{-1} \mathbf{g}_C$$

- The coupling matrices  $\mathbf{\Gamma}_{L,R}$ , which describe the coupling of the central cluster to the leads:

$$\mathbf{\Gamma}_{L,R} = i(\mathbf{\Sigma}_{L,R} - \mathbf{\Sigma}_{L,R}^\dagger) = 2 \cdot \text{Im} \mathbf{\Sigma}_{L,R}$$

And with

$$\delta(\mathbf{E} - \mathbf{H}_{L,R}) = (2\pi)^{-1} (\mathbf{g}_{L,R} - \mathbf{g}_{L,R}^\dagger)$$

using the definition of  $\mathbf{\Sigma}$ , we find the expressions within the states of the central cluster  $|c\rangle$

$$\langle c' | \mathbf{\Gamma}_L | c \rangle = 2\pi \langle c' | \mathbf{t}_L \delta(\mathbf{E} - \mathbf{H}_L) \mathbf{t}_L^\dagger | c \rangle \quad (3.22)$$

$$\langle c' | \mathbf{\Gamma}_R | c \rangle = 2\pi \langle c' | \mathbf{t}_R^\dagger \delta(\mathbf{E} - \mathbf{H}_R) \mathbf{t}_R | c \rangle \quad (3.23)$$

How the terms we have presented above come about, can be easily understood by looking at the definitions of the Green's-functions for the three sub-Hamiltonians of the system,  $H_L$ ,  $H_R$  and  $H_C$ . The defining equations for these Green's-functions can be written as

$$\begin{pmatrix} \mathbf{E} - \mathbf{H}_L & -\mathbf{t}_L & 0 \\ -\mathbf{t}_L^\dagger & \mathbf{E} - \mathbf{H}_C & -\mathbf{t}_R^\dagger \\ 0 & -\mathbf{t}_R & \mathbf{E} - \mathbf{H}_R \end{pmatrix} \begin{pmatrix} \mathbf{G}_L & \mathbf{G}_{LC} & \mathbf{G}_{LR} \\ \mathbf{G}_{CL} & \mathbf{G}_C & \mathbf{G}_{CR} \\ \mathbf{G}_{RL} & \mathbf{G}_{RC} & \mathbf{G}_R \end{pmatrix} = \begin{pmatrix} \mathbf{I} & 0 & 0 \\ 0 & \mathbf{I} & 0 \\ 0 & 0 & \mathbf{I} \end{pmatrix} \quad (3.24)$$

Looking at the equations from the second column, we have

$$(\mathbf{E} - \mathbf{H}_L)\mathbf{G}_{LC} - \mathbf{t}_L\mathbf{G}_C = 0 \quad (3.25)$$

$$-\mathbf{t}_L^\dagger\mathbf{G}_{LC} + (\mathbf{E} - \mathbf{H}_C)\mathbf{G}_C - \mathbf{t}_R^\dagger\mathbf{G}_{RC} = \mathbf{I} \quad (3.26)$$

$$(\mathbf{E} - \mathbf{H}_R)\mathbf{G}_{RC} - \mathbf{t}_R\mathbf{G}_C = 0 \quad (3.27)$$

By substituting  $\mathbf{g}_{L,R}^{-1}$  from above for  $(\mathbf{E} - \mathbf{H}_{L,R})$  we obtain

$$\mathbf{G}_{LC} = \mathbf{g}_L\mathbf{t}_L\mathbf{G}_C \quad (3.28)$$

$$\mathbf{G}_{RC} = \mathbf{g}_R\mathbf{t}_R\mathbf{G}_C \quad (3.29)$$

which we can insert in equation 3.26 leading to

$$-\mathbf{t}_L^\dagger\mathbf{g}_L\mathbf{t}_L\mathbf{G}_C + (\mathbf{E} - \mathbf{H}_C)\mathbf{G}_C - \mathbf{t}_R^\dagger\mathbf{g}_R\mathbf{t}_R\mathbf{G}_C = \mathbf{I}, \quad (3.30)$$

to obtain the Green's-function  $\mathbf{G}_C$  for the central cluster as

$$\mathbf{G}_C = (\mathbf{E} - \mathbf{H}_C - \Sigma_L - \Sigma_R)^{-1}. \quad (3.31)$$

This is now all we need to calculate the transport properties. All quantities can be expressed within the finite dimensional Hilbert space of the central cluster.

We can plug all the ingredients from the list above into equation (3.19) for the transmission to arrive at

$$T(E) = \text{Tr}_C \left[ \Gamma_L \mathbf{G}_C \Gamma_R \mathbf{G}_C^\dagger \right]. \quad (3.32)$$

Now the trace is taken over all states in the central cluster instead of the states in the lead. The semi-infinite leads enter only in an implicit way via the self energy matrices  $\Sigma_{L,R}$ . This makes the dimensions of the matrices equal to the number of states in the central cluster and thus finite in contrast to the formulation within the states in the leads. Calculations in this finite dimensional Hilbert space are now numerically feasible.

### 3.2.3 Interacting electrons: the Meir–Wingreen formula

We will now turn to the finite temperature regime and consider systems that also include interaction. This will be done using the Keldysh/non–equilibrium Green’s–function formalism. An introduction of the formalism can be found in the book by Datta [63] or in [64]. Meir and Wingreen [65] have derived a general expression for the current flowing through a region of space, where the carriers can interact. This can, for example, be a quantum dot, an atomic wire or a molecule.

The Hamiltonian of the system has the same partitioning,

$$H = H_C + H_L + H_R + H', \quad (3.33)$$

as in the noninteracting case above.  $H_C$  describes the central cluster of the system, consisting of the molecule, atomic wire, point contact, or quantum dot, plus in addition, parts of the leads, see fig. 3.2, above. To include a sufficient portion of the leads is of crucial importance to ensure that all information about the scattering region is included in the central cluster (see 3.3 and 7 below for details).

This central cluster, or *extended molecule*, is then coupled to two semi–infinite leads with the Hamiltonians  $H_L$ ,  $H_R$  via the coupling  $H'$ . The bare leads are, as above, assumed to be non–interacting

$$H_{L,R} = \sum_{\alpha=l,r} \epsilon_{\alpha} \mathbf{c}_{\alpha}^{\dagger} \mathbf{c}_{\alpha}, \quad (3.34)$$

where  $\mathbf{c}_{\alpha}$ ,  $\mathbf{c}_{\alpha}^{\dagger}$  are the creation and annihilation operators for an electron in the left or right lead. The indices  $\alpha = l, r$  include all quantum numbers needed to define a state in the leads.

There again is no direct coupling between the leads, so  $H'$  takes the form

$$H' = \sum_{m,(\alpha=l,r)} (t_{\alpha m} \mathbf{c}_{\alpha}^{\dagger} \mathbf{d}_m + \text{h.c.}) \quad (3.35)$$

with the hopping matrix elements,  $t_{\alpha m}$ , describing coupling between the lead and the central cluster, and the creation/annihilation operators  $\mathbf{d}_m$ ,  $\mathbf{d}_m^{\dagger}$  of the central cluster.

The term for the central cluster

$$H_C = H_C(\{\mathbf{d}_m^{\dagger}\}; \{\mathbf{d}_m\})$$

now—in contrast to the Landauer case above—does in general include electron–electron interaction. Its detailed structure will be of no importance to the derivation of the Meir–Wingreen formula:

$$I = \int dE \operatorname{Tr}(f_l \mathbf{\Gamma}_L - f_r \mathbf{\Gamma}_R)(\mathbf{G}_C - \mathbf{G}_C^\dagger) + \operatorname{Tr}(\mathbf{\Gamma}_L - \mathbf{\Gamma}_R) \mathbf{G}_C^<. \quad (3.36)$$

The formula connects the retarded (advanced) Green’s functions  $\mathbf{G}_C$  ( $\mathbf{G}_C^\dagger$ ) and the lesser Green’s–function  $\mathbf{G}_C^<$  of the full many-body problem including the coupling to the leads. These are again defined in the Hilbert space of the *extended molecule*.

$f_{l,r} = f(E - \mu_{l,r})$  denote the Fermi distribution functions for the left/right lead, respectively, which are assumed to be at chemical potentials  $\mu_{l,r}$ .  $\mathbf{\Gamma}_{L,R}$  describes the coupling of the molecule to the external leads. The dependence on energy  $E$  has been omitted.

The coupling matrices,  $\mathbf{\Gamma}_{L,R}$ , are known from the non–interacting case above, whereas the Green’s–functions  $\mathbf{G}_C$  and  $\mathbf{G}_C^<$  are now more complicated due to the included interaction effects. Obtaining these, especially the lesser function  $\mathbf{G}_C^<$ , which is more complicated as it depends on the occupation distribution  $f$ , is difficult. The derivation of the Meir–Wingreen formula is sketched in the appendix A.

In the non–interacting case, the lesser Green’s–function can be expressed as

$$\mathbf{G}_C^< = i \mathbf{G}_C (f_L \mathbf{\Gamma}_L + f_R \mathbf{\Gamma}_R) \mathbf{G}_C^\dagger \quad (3.37)$$

and  $\mathbf{G}_C$  is now the Green’s–function of the central cluster from the non–interacting case in the subsection above. Also, we can still write for the couplings,  $\mathbf{\Gamma}_{L,R}$ ,

$$\mathbf{\Gamma}_{L,R} = i(\mathbf{\Sigma}_{L,R} - \mathbf{\Sigma}_{L,R}^\dagger). \quad (3.38)$$

This then reduces equation 3.36 in the non–interacting case to

$$I = \frac{e}{h} \int dE [f_L(E) - f_R(E)] \operatorname{Tr}(\mathbf{G}^\dagger \mathbf{\Gamma}^R \mathbf{G} \mathbf{\Gamma}^L), \quad (3.39)$$

which is the result we have obtained previously in the subsection above — but here it is valid for finite temperatures and in the regime beyond linear response, provided that  $\mathbf{G}$  is calculated self–consistently, i.e., in the presence of a finite current.

## 3.3 Transport through single molecules: our implementation

### 3.3.1 The matrix equations

As the conductance of molecules and atomic wires is very sensitive to details of the molecular structure, spectral and orbital properties of the molecules and their wavefunctions, *ab initio* methods are an indispensable tool for transport calculations. We will see later (§3.3.2), that also parts of the electrodes have to be included into the calculation of the orbital properties. The resulting system to be calculated in general will consist of a large number of electrons ( $\sim 10^3$ ), so that wavefunction based methods, where the numerical effort scales exponentially with the particle number, are too costly. Density Functional Theory currently is the only suitable method for the calculation of the electronic structure of an interacting many electron system with such a large number of electrons. For this reason the current method of choice is to use DFT to obtain an approximation for the Green's-functions of the central cluster (*extended molecule*) for the application of the Landauer scattering formalism. A description of the DFT formalism and used functionals is given in chapter 4.

The DFT calculation yields effective single particle wavefunctions describing the ground state of our system, consisting of molecule/wire plus parts of the leads. From these we can then construct the Green's-functions and other required ingredients to the Landauer-Büttiker formalism. How this is done, will be the focus of this section.

Our approach is similar to others that have been described in detail in [66–68]. Our implementation is special in contrast to previous ones in that we can include a considerably larger number of contact gold atoms in the calculation for the central cluster. This enables us to avoid artefacts from the coupling to the leads. In addition, we treat leads and molecule on the same footing (in contrast to hybrid methods involving tight-binding for the leads). This renders our method fully *ab initio*, no adjustable parameters at all are required.

We make use of the program package TURBOMOLE [69] for our DFT calculations, which is currently one of the most powerful and advanced DFT packages available.

As described in the section above, the transmission  $T(E)$  is given in the Landauer formulation by eq. 3.32 as

$$T(E) = \text{Tr}_C \left[ \Gamma_L \mathbf{G}_C \Gamma_R \mathbf{G}_C^\dagger \right] \quad (3.40)$$

Equation 3.40 is a matrix equation and its numerical solution is a standard procedure. The problem lies in the detail of how the input for the different terms—especially  $\mathbf{g}_0$  and  $\Sigma$ —are obtained.

We already listed the ingredients necessary to calculate the transmission with this formula. Here, we will first discuss how they are constructed from quantum chemical data in general. In the following, a detailed description of our procedures to construct the Green’s-function of the lead as well as the calculation of the coupling matrices will be given. There, we will also elaborate on the advantages this special construction offers.

We need to obtain:

- The full Green’s-function  $\mathbf{G}$  of the molecule,

$$\mathbf{G}_C^{-1} = \mathbf{g}_0^{-1} - \Sigma_L - \Sigma_R \quad (3.41)$$

calculated from

- the unperturbed Green’s-function of the central cluster,  $\mathbf{g}_0$
- the self energies

$$\Sigma_{L,R} = \mathbf{t}_{L,R} \mathbf{g}_{L,R} \mathbf{t}_{L,R}^\dagger$$

- with the hopping matrix elements  $\mathbf{t}_{L,R}$  which describe the hopping between the central cluster and the left/right lead, respectively.
- the unperturbed surface Green’s-function of the lead  $\mathbf{g}_{L,R}$

- The coupling matrices  $\mathbf{\Gamma}_{L,R}$

$$\mathbf{\Gamma}_{L,R} = i(\Sigma_{L,R} - \Sigma_{L,R}^\dagger) \quad (3.42)$$

which describe the coupling of the central cluster to the left/right lead

Quantum chemical DFT calculations usually make use of localized, but non-orthogonal basis sets (for a description see §4.6.1). The output of the program package TURBOMOLE used for our calculations is expanded in a localized, non-orthogonal basis set, as well.

There are two possible approaches to work with this data: we can either stick to the non-orthogonal quantum chemical basis set, which renders calculations in matrix notation more complicated as we have to introduce an overlap matrix. Or, we can orthogonalize the states using a Löwdin transformation.

- **Using a non-orthogonal basis set**

We have to introduce the overlap matrix  $\mathbf{S}$

$$\mathbf{S}_{\mu\nu} = \langle \mu | \nu \rangle \quad (3.43)$$

which is the overlap integral of the basis functions  $\varphi_\mu(\mathbf{r})$  and  $\varphi_\nu(\mathbf{r})$  of the quantum chemical basis, in order to describe matrix operations in a non-orthogonal basis.

The orthonormality relation for states in an orthonormal basis set,  $\langle n | m \rangle = \delta_{nm}$ , takes for states

$$|\Psi_n\rangle = \sum_{\mu} c_{\mu n} |\mu\rangle \quad (3.44)$$

in non-orthogonal basis a different shape as

$$\langle \Psi_n | \Psi_m \rangle = \langle \Psi_n | \mu \rangle \mathbf{S}_{\mu\nu}^{-1} \langle \nu | \Psi_m \rangle = \delta_{nm}. \quad (3.45)$$

- **Orthogonalizing the basis set**

Using the overlap matrix, we can perform a *Löwdin transformation* [70, 71] to obtain a localized and orthogonal basis set. The new basis states are defined by

$$|\varphi_\nu\rangle_{\text{orth}} = \mathbf{S}^{-\frac{1}{2}} |\varphi_\nu\rangle \quad (3.46)$$

For more information on the use of nonorthogonal basis sets see, e.g., [71].

### The unperturbed Green's-function of the central cluster

The DFT calculation yields effective single-particle wavefunctions, the Kohn-Sham states,

$$\Phi_\mu = \sum_{\nu} c_{\mu\nu} \varphi_\nu, \quad (3.47)$$

expanded in a finite basis set  $\{\varphi_\nu\}$ .

Due to the non-orthogonality of the quantum chemical basis sets, the equation for the unperturbed Green's-function takes a different form. In matrix notation, it can be calculated as

$$\mathbf{g}_{\nu\mu}(E) = \sum_n \frac{c_{n\nu} c_{n\mu}^*}{E - \varepsilon_n + i\eta} \quad (3.48)$$

where the coefficients  $c_{n\nu}$  are given by

$$c_{n\nu} = \sum_{\mu} [\mathbf{S}^{-1}]_{\nu\mu} \langle \mu | \psi_n \rangle, \quad (3.49)$$

and  $|\psi_n\rangle = c_{n\nu}|\nu\rangle$  are the orthogonal Kohn–Sham ground–state wave–functions from the quantum chemical output with the non–orthogonal basis–functions  $|\mu\rangle$ .

This notation can be verified by using equation 3.45 for the overlap matrix on the modified definition of the Green’s–function for a non–orthogonal basis set:

$$\mathbf{g}_0(E) = \frac{1}{(E + i\eta)\mathbf{S} - \mathbf{H}} \quad (3.50)$$

where the Hamiltonian  $H$  in the notation of the (non–orthogonal) chemical basis fulfills

$$H_{nm} = \sum_{\mu\nu} c_{n\mu} H_{\mu\nu} c_{m\nu} = \varepsilon_n \delta_{nm} \quad (3.51)$$

and the eigenstates  $|\psi_n\rangle$  have the energies  $\varepsilon_n$ .

### 3.3.2 Self–energies and Green’s–functions from DFT

Defining the *extended molecule* and the self–energies

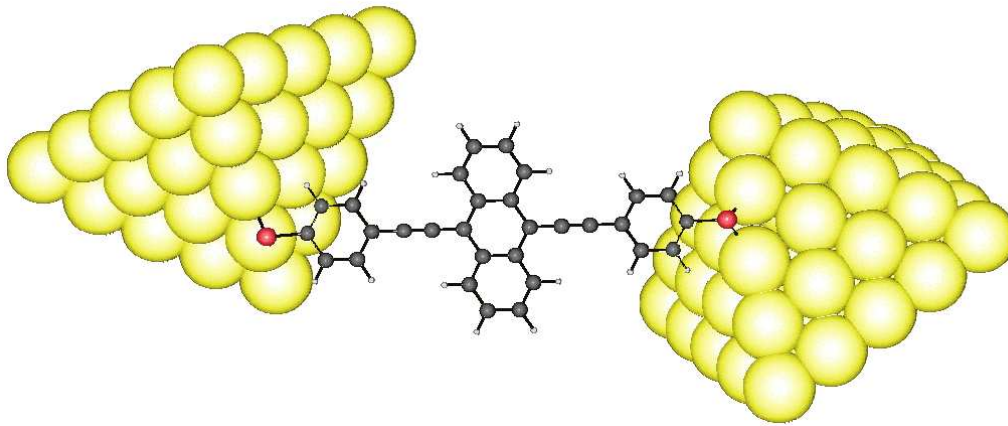


Figure 3.4: Example for the extended molecule: here, two gold–pyramids of 55 atoms each, are added to the molecule (discussed in section 6.2). This combined system constitutes the central cluster / extended molecule as used in our DFT calculations.

With the program package TURBOMOLE we conduct Density Functional Theory calculations of the central cluster (see chapter 4) to obtain the ground–state energy, ground–state density, and the Kohn–Sham wavefunctions—describing the ground–state in an effective single–particle picture. An example for a central cluster is depicted in figure 3.4.

Artefacts originating from the coupling of the molecule to the leads when calculating the full Green's-function of the central cluster,  $\mathbf{G}_C$ , can only be excluded, if portions of the leads are included in the calculation of the central cluster. Therefore, we define an *extended molecule* that comprises parts of the contacts in addition to the molecule.

If we choose the extended molecule large enough, we can arrange the new contact surfaces between the central region and the leads sufficiently far away from the physical contact so that the outer contact atoms do not feel any disturbance due to the molecule. Then the new self-energies again will only depend on the type of the lead and will be completely independent of the actual molecule under consideration. The following inequalities have to be met:

$$\delta_{eM} < \gamma_{eM} \ll \gamma_M. \quad (3.52)$$

The level spacing of the *extended molecule*,  $\delta_{eM}$ , has to be smaller than the level broadening of the *extended molecule*,  $\gamma_{eM}$ , caused by the coupling to the leads. This level broadening,  $\gamma_{eM}$ , again has to be much smaller than the broadening of the bare contact/molecule,  $\gamma_M$ . Only if both conditions are fulfilled, all information on the contact is contained in the central cluster, and we can assure that the details of the coupling to the leads via the self-energies and the modeling of the leads do not lead to implementation dependent artefacts. In many calculations performed previously by other groups, these conditions were not fulfilled (e.g., [67, 72, 73]).

In fact, if such a separation of energy scales is generated, any choice of the coupling  $\gamma_{eM}$ , fulfilling this inequality, will produce a suitable self-energy. We could just use the simple replacement

$$\Sigma_{L,R}(\mathbf{x}, \mathbf{x}') = i\gamma_{eM}\delta_{\mathbf{x}\mathbf{x}'} \quad (3.53)$$

with  $x, x'$  being situated on the contact surface. The results will be completely independent of this choice. This means as well, that if the extended molecule includes sufficiently many lead atoms, the microscopic information carried by the self-energies becomes trivial. Within this limit, all information on the transport properties is carried by the matrix  $\mathbf{G}_C$  of the central cluster.

This insensitivity to the approximations made for the self-energy have a simple experimental correlate: there is a free choice to attach leads of any sort and shape/material to the contact region as long as the voltage drop is occurring in the vicinity of the real molecule — which should quite obviously be the case.

### The unperturbed Green's-function of the leads

The unperturbed Green's-function,  $\mathbf{g}_L$ , describing the electronic structure of the semi-infinite gold leads, is obtained from a second DFT calculation. This time a cluster of pure gold with a large enough number of atoms is used to characterize the structure of bulk gold. The DFT calculation gives us the Kohn-Sham eigenvalues and the Kohn-Sham eigenstates. From these, we can reconstruct a tight-binding Hamiltonian. This Hamiltonian has in general hopping elements from each atom to every other atom. However, we only consider the central atom and its hopping matrix elements with all other atoms. If we then assume to sit in bulk gold, we can reconstruct a bulk Hamiltonian by identifying these hopping matrix elements with the hopping matrix elements of any atom in bulk gold. This way a Fourier transform into  $k$ -space is possible and we can obtain a tight-binding Hamiltonian for bulk gold in  $k$ -space.

Then, the bulk Green's-function,  $\mathbf{g}_L$ , is just given by

$$\mathbf{g}_L = \frac{1}{E - \varepsilon_k + i0} \quad (3.54)$$

where  $\varepsilon_k$  is the spectrum of our tight-binding Hamiltonian.

For each energy value  $E$ , the Green's-functions are calculated in  $k$ -space, where the Brillouin zone is sampled with 61 points per dimension. It turned out to be sufficient to consider the hopping contributions of the 12 nearest neighbors when calculating the Green's-function to achieve convergence (see §5.1 below).

We chose to use an *fcc* bi-pyramid of 146 gold-atoms as an approximation to bulk gold for the calculation. Testing other gold-cluster sizes like 84 atoms, and 184 atoms, 146 proved to be sufficient to obtain an excellent approximation to the band structure. In §5.1, we will present our results obtained from this calculation.

### The self-energies $\Sigma$ and the hopping matrix elements $t$

In principle, in order to construct the self-energies, we need to use the surface Green's-function. However, in view of the large number of gold atoms included in our extended molecule, it is legitimate to approximate the surface Green's-function by the bulk Green's-function, which we will do.

In our calculations, we typically coupled on each side of the central cluster 41 of these gold atoms, i.e., the two outer layers (4x4 and 5x5 layer), to the leads, see fig. 3.5. This number of coupling atoms proved to be sufficient, using a larger coupling area did not change the transmission characteristics any more.

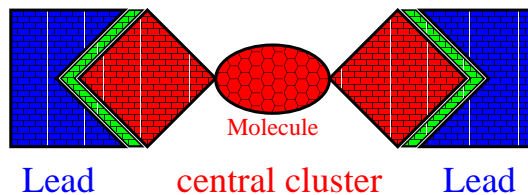


Figure 3.5: Schematic representation of the contact surface. Hopping matrix elements are extracted for a small set of surface atoms (depicted in green) within the gold.

In §5.2 we will discuss in more detail the influence of the coupling region on the conductance.

We assume the coupling to be far inside the leads (as we include a large portion of gold atoms in the central cluster). Thus the calculation of the hopping elements can be done using the large gold cluster representing bulk gold (as for the Green’s–function of the leads).

As described above, the self–energy is obtained via the hopping matrix elements,  $t$ , as

$$\Sigma_{L,R} = \mathbf{t}_{L,R} \mathbf{g}_{L,R} \mathbf{t}_{L,R}^\dagger \quad (3.55)$$

The hopping matrix elements  $t(\mathbf{x}, \mathbf{x}')$ , which describe the hopping of an electron at position  $\mathbf{x}$  in the central cluster to position  $\mathbf{x}'$  in the lead, are the same we extracted from the DFT–calculation for the bulk Green’s–function of the leads.

Thus they, and the resulting self–energy matrices  $\Sigma(E)$  only need to be calculated once per energy, independent of the molecule or wire we want to do the transport calculation for, as long as the geometry of the coupling layers is unchanged. They are then stored, ready to re–use for any future transport calculations of the same or different molecules.

Again, the calculation is done in  $k$ –space, together with the calculation of the bulk Green’s–function, described in the subsection above. The 12 nearest neighbors are considered in the calculation of the hopping terms:

In the atomical basis, with the indices  $\mathbf{x}, \mathbf{y}'$  describing the atom positions and the orbital indices  $i, j, m, n$ , the self–energy is given by

$$\Sigma_{im}(\mathbf{x}, \mathbf{x}') = \sum_{j,n} \sum_{\mathbf{y}, \mathbf{y}'} t_{ij}(\mathbf{x}, \mathbf{y}) g_{L,jn}(\mathbf{y}, \mathbf{y}') t_{nm}^\dagger(\mathbf{y}', \mathbf{x}') \quad (3.56)$$

where  $\mathbf{g}_L$  is the unperturbed Green’s–function of the leads from above. Using the same approach (sit on central atom, assume bulk periodic system) we can

again perform a Fourier transformation for the self-energy. For the Green's-function of the leads,  $\mathbf{g}_L$ , we thus obtain the expression 3.54 from above, and the self-energy takes the form

$$\Sigma_{im}(\mathbf{x}, \mathbf{x}') = \sum_{j,n} \sum_{\mathbf{k}} [t_{ij}(\mathbf{k}) e^{i\mathbf{k}\mathbf{x}}] g_{\mathbf{k}} [e^{-i\mathbf{k}\mathbf{x}'} t_{nm}(\mathbf{k}')], \quad (3.57)$$

where the  $\mathbf{x}, \mathbf{x}'$  are the positions, the Kohn-Sham orbitals of the states  $i, m$  of atomical basis are centered on.

All matrices used in the calculation of the trace in eq. 3.32 for the transmission are of dimension [two times the number of surface states per side], as the ingredients are projected on the surface atoms of the central cluster. Thus the final self-energy matrix  $\Sigma(E)$  is then obtained by combining the matrices  $\Sigma_{L,R}(E)$ , which are identical due to the symmetric definition of the contact surface, into

$$\begin{pmatrix} \Sigma_L & 0 \\ 0 & \Sigma_R \end{pmatrix}, \quad (3.58)$$

which is again of the correct dimension.

### The unperturbed Green's-function of the extended molecule

The unperturbed Green's-function of the *extended molecule* is obtained from the Kohn-Sham states  $|\Psi_n\rangle$ , which are given by the output of the DFT-calculation for the extended molecule. The actual calculation is done as described in §3.3.1 on page 33.

As we have seen above, the coupling between the extended molecule and the leads is described via the self-energies. To obtain the full Green's-function of the device, we do not need to obtain the Green's-function in the full Hilbert space of the extended molecule. Instead the Hilbert space of the surface atoms, where the coupling to the leads via the self-energies is done, is sufficient (usually 16+25 atoms in two layers of gold (4x4 and 5x5 bottom layers of the pyramids) for each side of the extended molecule, as described above).

### The matrices $\Gamma_{L,R}$ and the full device Green's-function $\mathbf{G}_C$

With all ingredients obtained, we can now construct the full Green's-function of the device by simple matrix operations as

$$\mathbf{G}(E) = (\mathbf{G}_0^{-1}(E) - \Sigma(E))^{-1}. \quad (3.59)$$

The couplings  $\Gamma_{L,R}$ , which are also identical due to our symmetric design of the coupling layers on the left and right hand side of the central cluster, are

obtained from  $\mathbf{\Gamma} = \mathbf{\Sigma} - \mathbf{\Sigma}^\dagger$ . With these, again, matrices of the dimension  $2 \cdot (\text{number of surface states per lead})$  are constructed via:

$$\mathbf{\Gamma}_L = \begin{pmatrix} \mathbf{\Gamma} & 0 \\ 0 & 0 \end{pmatrix}, \quad \mathbf{\Gamma}_R = \begin{pmatrix} 0 & 0 \\ 0 & \mathbf{\Gamma} \end{pmatrix} \quad (3.60)$$

After we have calculated all the necessary matrices for every energy value, we can evaluate the transmission contributions of each state from equation 3.32

$$T(E) = \text{Tr} [\mathbf{\Gamma}_L \mathbf{G}_C^r \mathbf{\Gamma}_R \mathbf{G}_C^a]$$

by matrix multiplications and then evaluate the conductance by taking the trace.



# Chapter 4

## Density Functional Theory (DFT)

### 4.1 Introduction: why do we need DFT?

An important goal of the theoretical description of transport through molecules is, to find an *ab initio*, i.e., parameter free approach to the quantitative description of the I–V characteristics of a single molecule with reasonable numerical effort.

Density Functional Theory (DFT), in combination with the Landauer–Büttiker approach to transport is currently *the* standard method for this task and DFT is used for a great variety of problems in the field. This chapter will deal with the basics of DFT in general and the reasons for its application to electronic transport in nanostructures.

DFT is a very effective method for *ab initio* calculations of the ground–state electron density, the ground–state energy, and the ionization potential of an interacting many–electron system in an external potential — usually the potential caused by the ion–cores in the Born–Oppenheimer approximation. It provides the possibility to derive results free of any fitting parameters, thereby lifting many of the restrictions of other methods like, e.g., tight–binding approaches. The foundations were laid by Hohenberg, Kohn and Sham in 1964 and 1965 [74, 75].

The popularity of DFT stems from the fact that it has been applied extremely successfully to the calculation of bond lengths, ionization energies and binding energies of molecular systems. Also, excellent results for ground–state electron densities and band structures of solid state systems and molecular systems were obtained.

There exist many other, and often more accurate *ab initio* wave-function based methods but they are numerically too costly to be applicable for large molecular systems. Examples are *Monte Carlo* or *Configuration Interaction* approaches. Traditional wave-function methods, e.g. *Configuration Interaction* methods, scale exponentially with the number of electrons. This makes them unusable for larger systems ( $N \gg 10$  electrons), a restriction lifted by the numerically efficient density functional approach.

In DFT, computation time goes as  $t \propto N^{2\cdots 3}$  with the number of electrons, with ongoing progress towards linear scaling. This is achieved by using the density instead of the actual many-body wavefunction as the variable to work with when calculating the ground-state electronic structure. The Hohenberg-Kohn Theorems, which we will discuss in the next section, give the justification for this procedure. They allow to uniquely relate the ground-state density  $n_0(\vec{r})$  of an interacting many-body system to the external potential  $V_{ext}(\vec{r})$ .

Expanding the density in a system of effective non-interacting particles and using an orbital picture to describe these particles, the number of variables required is reduced tremendously. The Kohn-Sham equations, which we describe in section §4.3 will provide a numerically efficient scheme to solve this system for the electronic ground-state structure. In contrast to the original many-body system, where, due to interaction, the number of variables required to describe the many-body wavefunction grows exponentially with the number of electrons, the variables describing the states of the effective single-particle system in the orbital picture can be varied independently in the search of the correct electronic structure. This way, DFT calculations for system sizes of up to  $10^3 - 10^4$  electrons become feasible.

This procedure allows to reduce the many-body problem to an effective single particle problem. Provided the correct energy functional for the density, which is needed during this process to establish the effective single-particle system, is known, the equations are in general *exact* and include *all* many-body effects.

## Outline of this chapter

Within this work, we can only give a very brief account of the main underlying ideas of DFT, which will be the subject of this chapter. An overview is given in the Nobel lecture by W. Kohn [76], a more thorough discussion can be found in the book by Dreizler and Gross [77], the manuscript by Burke [78] or the review by Jones and Gunnarson [79]. First, the justification for using the ground-state density instead of the many-body wave-function to describe the interacting system, formulated in the Hohenberg-Kohn Theorem I, will be presented. We will then explain in §4.2.2 why we can apply the variational

principle to obtain the ground–state density of the system. In the following section, §4.3 we will introduce the Kohn–Sham equations, a practical recipe of how to apply the variational principle in a numerically efficient way to find the ground–state density.

Before giving a brief overview over available choices of DFT functionals, basis sets and their physical origin in §4.7, we will shortly describe some extensions to DFT, like spin–DFT in §4.4. Also the derivative discontinuity problem will be addressed (§4.5). This will be followed by a concise description of the practical implementation of the DFT formalism and the program package TURBOMOLE [69] used within this work.

The final section of this chapter, §4.10, will deal with time–dependent DFT, the extension of the DFT scheme to time–dependent interacting electron systems, which is of special interest to us as it is in many cases the more appropriate formalism to apply when investigating transport: for time–independent systems in non–equilibrium as well as for time–dependent systems, equilibrium DFT can fail in many cases. Our findings on the applicability of DFT to transport and the problems that arise in non–equilibrium situations will be described later, in chapter 7.

## 4.2 Hohenberg–Kohn theorems

— Or, why we can do it ...

### 4.2.1 Hohenberg–Kohn theorem I

The Hohenberg–Theorem I [74] states:

The ground–state density  $n(\vec{r})$  of a bound system of interacting electrons in some external potential  $V_{\text{ext}}(\vec{r})$  determines this potential uniquely (up to a constant).

The proof will be given below.

For atoms, molecules or solids, the external potential usually is the potential produced by the ion cores (at positions  $\mathbf{R}_i$ , with nuclear charge  $Z_i$ ) in the Born–Oppenheimer approximation of fixed nuclei ( $v_{\text{ext}}(\mathbf{r}) = \sum_i \frac{Z_i}{|\mathbf{R}_i - \mathbf{r}|} \frac{\mathbf{r}}{|\mathbf{r}|}$ ). It can include some additional potential from external fields. In case of a degenerate ground–state, the theorem refers to *any* ground–state density.

The ground–state density, by determining the external potential uniquely, in consequence also determines the many–body system in general. We can thus describe the Hamiltonian, and all its ground–state properties with the ground–state density. Thus we can formulate: the ground state expectation value of any observable  $\hat{O}$  is a unique functional of the ground–state density, e.g., the ground–state energy,  $E$ , can be obtained from the ground–state density,

$$E[n(\vec{r})] = \langle \psi[n] | T + V_{ee} + V_{\text{ext}} | \psi[n] \rangle. \quad (4.1)$$

This very powerful theorem enables us to use the density instead of the many–particle wavefunctions to calculate the electronic structure. The functional  $\hat{O}[n]$  is in most cases not known, but in the case of the ground–state energy, the research in DFT resulted in many excellent approximations that yield good results for calculating the *ground–state energy* and *electron density* of an interacting many–body system.

### Proof of Hohenberg–Kohn theorem I

For the nondegenerate case, the bijective map  $n(\vec{r}) \longleftrightarrow v_{\text{ext}}(\vec{r})$  can easily be proven by contradiction:

Let  $n(\vec{r})$  be the nondegenerate ground–state density of  $N$  electrons in the potential  $v_1(\vec{r})$ , with the ground state  $\psi_1(\vec{r})$  and ground–state energy  $E_1$ . With the Hamiltonian  $H_1 = T + V_{ee} + V_1$ , where  $T$  and  $V_{ee}$  are the kinetic and interaction part, respectively, we can write for the energy:

$$E_1 = \langle \psi_1 | H_1 | \psi_1 \rangle = \int d^3r v_1(\vec{r}) n(\vec{r}) + \langle \psi_1 | T + V_{ee} | \psi_1 \rangle \quad (4.2)$$

If we now assume, there exists a second potential,  $v_2(\vec{r}) \neq v_1(\vec{r}) + \text{const.}$ , with the same ground–state density, and the ground–state,  $\psi_2(\vec{r})$ , we can write for the energy of this system

$$E_2 = \langle \psi_2 | H_2 | \psi_2 \rangle = \int d^3r v_2(\vec{r}) n(\vec{r}) + \langle \psi_2 | T + V_{ee} | \psi_2 \rangle. \quad (4.3)$$

As the ground state is nondegenerate, we obtain

$$E_1 < \langle \psi_2 | H_1 | \psi_2 \rangle = \int d^3r v_1(\vec{r}) n(\vec{r}) + \langle \psi_2 | T + V_{ee} | \psi_2 \rangle \quad (4.4)$$

Subtracting eq.(4.3) from eq. (4.4) results in

$$E_1 < E_2 + \int d^3r (v_1(\vec{r}) - v_2(\vec{r})) n(\vec{r}) \quad (4.5)$$

Similarly,

$$E_2 \leq \langle \psi_1 | H_2 | \psi_1 \rangle = E_1 + \int d^3r (v_2(\vec{r}) - v_1(\vec{r}))n(\vec{r}) \quad (4.6)$$

(4.2.1) in (4.5) leads to the contradiction  $E_1 < E_1$ .

Therefore,  $n(\vec{r})$  uniquely defines the external potential, and with that, the many-body system, its Hamiltonian and all its ground-state properties (under the given form  $H = T + V_{ee} + V_{\text{ext}}$ ). The requirement of non-degeneracy can easily be lifted [77].

## 4.2.2 Hohenberg–Kohn theorem II

The second Hohenberg–Kohn Theorem [74] provides the justification for the use of the variational principle on the density  $n(\vec{r})$  to obtain the electronic ground-state density  $n_0(\vec{r})$ . It states:

There exists a variational approach for the density,  $n$ , of the form

$$\delta \left[ E[n] - \mu \left( \int d^3r n(\mathbf{r}) - N \right) \right] = 0$$

, with the Lagrange multiplier  $\mu$ , that yields the exact ground-state electron density of the  $N$  electron system.

In general, we could also perform the variation directly in the space of all trial wavefunctions  $\tilde{\psi}(\vec{r})$  with  $\int d^3r |\tilde{\psi}(\vec{r})|^2 = N$ , in order to obtain the ground-state energy and density:

$$E = \min_{\tilde{\psi}} \langle \tilde{\psi} | H | \tilde{\psi} \rangle. \quad (4.7)$$

But this is by far too complex for an interacting electron system with more than a few electrons as the dimension of the trial space growth exponentially with the number of electrons.

### V–representability

The proof of HK II is complicated by a problem called *v–representability*:

In the process of applying a variational principle, trial densities with small changes from the real ground-state density are used. In order to evaluate the energy term in the variation formula, the trial density has to correspond to an external potential  $v(\vec{r})$ . In an actual calculation

of the ground-state electron density within an iterative scheme, as we will establish below with the Kohn–Sham equations in §4.3, we would in general not even start out from a trial density close to the real ground-state density. Thus the following question arises:

Is any well behaved density  $n(\vec{r})$  which integrates to an integer number of electrons, a possible ground state–density corresponding to a potential  $v(\vec{r})$ ? A density which fulfills this, is called *v-representable*.

There exist well-behaved densities that are not v-representable, for examples see [80]. But this issue has so far not appeared as a limitation in practical applications of DFT. The trial-densities needed to obtain a good approximation for the ground state can be chosen in a way that they are all v-representable. For a more detailed discussion on v-representability, see [77].

In order to circumvent some of the problems associated with the v-representability we will not present the original derivation of the Hohenberg–Kohn Theorem II [74], but the a, more succinct derivation of the applicability of the variational principle performed by Levy and Lieb in 1982 [80, 81], called the *constrained search method*. There, the space of trial densities can be restricted to v-representable densities.

### Proof of Hohenberg–Kohn theorem II [80, 81]

We consider a system with the ground-state energy  $E_0$  and ground-state electron density  $n_0$ .

By virtue of the Rayleigh–Ritz principle, it is obvious, that for trial densities  $\tilde{n}(\vec{r})$ ,

$$E_0 < E[\tilde{n}] \quad \text{for} \quad \tilde{n} \neq n_0 \quad \text{and} \quad E_0 = E[n_0]. \quad (4.8)$$

We define the Hohenberg–Kohn functional as

$$F_{HK}[n(\vec{r})] \equiv \langle \psi | T + V_{ee} | \psi \rangle. \quad (4.9)$$

The energy functional,  $E[n]$ , can now be written as

$$E[n] = \int d^3r v(\vec{r})n(\vec{r}) + F_{HK}[n]. \quad (4.10)$$

$F_{HK}[n]$  is, if known explicitly, an extremely powerful universal functional, valid for any number of particles and any external potential — from atoms to molecules and solid state systems. Section 4.7 will deal with the construction of appropriate functionals and the underlying approximations.

The minimization of the energy functional is done in two stages:

- First, the trial density  $\tilde{n}(\vec{r})$  (with  $\int d^3r \tilde{n}(\vec{r}) = N$ ) is fixed. A constrained energy minimum of all trial wavefunctions  $\tilde{\psi}_n^\alpha(\vec{r})$  which yield this density  $\tilde{n}(\vec{r})$  is obtained

$$\begin{aligned} E[\tilde{n}(r)] &\equiv \min_{\alpha} \langle \tilde{\psi}_n^\alpha | H | \tilde{\psi}_n^\alpha \rangle \\ &= \int d^3r v(\vec{r}) \tilde{n}(\vec{r}) + F_{HK}[\tilde{n}(\vec{r})]. \end{aligned} \quad (4.11)$$

As the universal  $F_{HK}$  does not depend on the external potential  $V$ , it can be minimized individually for all trial densities.

- In the second step, equation (4.11) is minimized over all trial densities  $\tilde{n}(\vec{r})$

$$\begin{aligned} E &= \min_{\tilde{n}} E[\tilde{n}(\vec{r})] \\ &= \min_{\tilde{n}} \left\{ \int d^3r v(\vec{r}) \tilde{n}(\vec{r}) + F_{HK}[\tilde{n}(\vec{r})] \right\}. \end{aligned} \quad (4.12)$$

The trial wavefunctions  $\tilde{\psi}(\vec{r})$  from which the density is constructed, are usually expanded in a suitably designed basis set of, e.g., localized atomic orbitals or plane waves. See section 4.6.1 for details on how to choose the appropriate basis sets.

## 4.3 Kohn–Sham equations

— Or, how can we do it ...

In the preceding sections we discussed why we can use the density instead of the many–body wavefunction as an approach to find the ground–state density. In order to do this in a numerically efficient way, we still need an explicit scheme on how to conduct the minimization of the energy in the space of trial densities in a numerically feasible way.

The idea behind the Kohn–Sham formalism is to define an effective single–particle system of electrons moving in an effective external potential that yields exactly the same ground–state electron density as the ground–state density of the interacting system. Then, instead of a direct variation of the density, an orbital picture is used to construct the electron density:

$$n(\mathbf{r}) = \sum_{j=1}^N |\phi_j(\mathbf{r})|^2, \quad (4.13)$$

with the states  $\phi_j(\mathbf{r})$ . This way, variations of the density can be carried out by modifying these states. As we now describe a non–interacting system in

the orbital picture, we have achieved a tremendous gain in numerical efficiency compared to the original interacting system. The different states can be varied independently. For the actual variation an expansion in a finite basis is used.

We will sketch the derivation of this variational scheme in the next subsection. It will allow us to formulate a set of single-particle equations, similar to the self-consistent Hartree equations,

$$\left\{ -\frac{1}{2}\nabla^2 + v_H(\mathbf{r}) \right\} \phi_j(\mathbf{r}) = \epsilon_j \phi_j(\mathbf{r}) \quad (4.14)$$

with  $n(\mathbf{r}) = \sum_{j=1}^N |\phi_j(\mathbf{r})|^2.$

that can be solved numerically. However, the results obtained by this approach go beyond the level of the Hartree-Fock approximation: due to the Hohenberg-Kohn theorems, this set of equations will yield a result that is in principle exact, if the appropriate functional for the energy is used as the effective single-particle system yields the same density as the real system. In terms of numerical effort, the set of single-particle equations makes the effort comparable to a mean field calculation.

## The Kohn-Sham scheme

We will now establish this *Hartree-like* scheme: we define an auxiliary system of  $N$  non-interacting particles in an effective potential yielding the *same* ground-state density as the real system. This non-interacting auxiliary system with the Hamiltonian

$$H_S = T_S + V_{\text{eff}} \quad (4.15)$$

is then mapped onto the original interacting problem. By virtue of the Hohenberg-Kohn theorem I there exists a unique energy functional for the effective single-particle system

$$E_S[n] = T_S[n] + \int d^3r v_{\text{eff}}(\mathbf{r})n(\mathbf{r}) \quad (4.16)$$

with the single-particle kinetic energy functional  $T_S[n]$ . A variation  $\delta E = 0$  yields the ground-state density  $n_0(\mathbf{r})$ .

The corresponding Euler-Lagrange equations

$$\delta E_V[\tilde{n}] = \int d^3r \delta\tilde{n}(\mathbf{r}) \left\{ v_{\text{eff}}(\mathbf{r}) + \frac{\delta T_S[\tilde{n}]}{\delta\tilde{n}(\mathbf{r})} \Big|_{\tilde{n}=n_0} - \epsilon \right\} = 0 \quad (4.17)$$

with the Lagrange–multiplier  $\varepsilon$  conserving the number of electrons  $N$ , lead to single–particle equations of the type of eq. 4.14.

The central assumption needed to define the Kohn–Sham scheme is, that every density of an interacting system that is  $v$ –representable is also non–interacting  $v$ –representable, which means it can also be represented by some non–interacting local effective potential  $V_{\text{eff}}(r)$ . As already mentioned above (§4.2.2), this is usually not a limiting problem in practical applications of DFT to atoms, molecules or metal clusters (see [77] for a thorough discussion). We will therefore just assume, that this always holds.

Let us now consider the interacting system again, the energy functional has the form of equation 4.10. We can rewrite this as

$$E_V[n] = T_S[n(\mathbf{r})] + \int d^3r n(\mathbf{r})v_{\text{ext}}(\mathbf{r}) + \frac{1}{2} \int d^3r' d^3r \frac{n(\mathbf{r})n'(\mathbf{r}')}{|\mathbf{r} - \mathbf{r}'|} + E_{xc}[\tilde{n}(\mathbf{r})], \quad (4.18)$$

where  $T_S[n(\mathbf{r})]$  is the kinetic energy functional for *non*–interacting electrons.

$E_{xc}[n(\mathbf{r})]$ , termed the *exchange–correlation energy functional*, is defined by this equation. Its explicit form is not known completely at this point, it is just implicitly defined by this equation. We will later discuss in §4.7, how approximate expressions are constructed.

The corresponding Euler–Lagrange equations take the form

$$\begin{aligned} \delta E_V[\tilde{n}(\mathbf{r})] &= \int d^3r \delta\tilde{n}(\mathbf{r}) \cdot \\ &\quad \left\{ v_{\text{ext}}(\mathbf{r}) + \int d^3r' \frac{n'(\mathbf{r}')}{|\mathbf{r} - \mathbf{r}'|} \right. \\ &\quad \left. + \frac{\delta}{\delta\tilde{n}(\mathbf{r})} (T_S[\tilde{n}(\mathbf{r})] + E_{xc}[\tilde{n}(\mathbf{r})]) \Big|_{\tilde{n}(\mathbf{r})=n_0(\mathbf{r})} - \epsilon \right\} \\ &= 0 \end{aligned} \quad (4.19)$$

where we can, by comparison with eq. (4.17), easily extract the effective potential

$$v_{\text{eff}}(\mathbf{r}) \equiv v(\mathbf{r}) + \int d^3r' \frac{n(\mathbf{r}')}{|\mathbf{r} - \mathbf{r}'|} + v_{xc}(\mathbf{r}) \quad (4.20)$$

with the exchange–correlation potential

$$v_{xc}(\mathbf{r}) \equiv \frac{\delta}{\delta\tilde{n}(\mathbf{r})} E_{xc}[\tilde{n}(\mathbf{r})] \Big|_{\tilde{n}(\mathbf{r})=n(\mathbf{r})}. \quad (4.21)$$

Now, the Euler–Lagrange equation 4.19 has the same form as equation 4.17 for non–interacting particles, but now it contains the effective external potential

$v_{\text{eff}}(\mathbf{r})$  instead of  $v(\mathbf{r})$ , so we can conclude that the ground-state density can be obtained by solving the effective single-particle equations analogous to the Hartree equations 4.14 above:

$$\left(-\frac{1}{2}\nabla^2 + v_{\text{eff}}(\mathbf{r}) - \varepsilon_j\right)\phi_j(\mathbf{r}) = 0, \quad (4.22)$$

with

$$n(\mathbf{r}) = \sum_{j=1}^N |\phi_j(\mathbf{r})|^2. \quad (4.23)$$

Eq. 4.20, 4.22 and 4.23 are the so-called self-consistent Kohn-Sham equations. Neglecting  $E_{xc}$  and  $v_{xc}$  they reduce to the Hartree equations. With exact knowledge of  $E_{xc}$  and  $v_{xc}$  *all* many-body effects are in principle included and the equations are exact. The quality of the results depends entirely on the approximations made when constructing the exchange-correlation energy.

The wavefunctions  $\phi_j(\mathbf{r})$  are usually expanded in some localized or plane-wave basis set to do the actual iterative variation until self-consistency is achieved. This will be discussed in more detail in section 4.6.1.

Before we discuss the different approximations for the exchange-correlation functional and the basis sets used, we will first give a short introduction into some extensions to DFT like including spin and allowing for fractional particle numbers and briefly discuss the practical implementation of the Kohn-Sham scheme.

## 4.4 Extensions: Spin Density Functional Theory (SDFT)

Up to now, we did not treat the different spins independently. As the ground state energy is a functional of the total electron density  $n(\mathbf{r})$  alone, this is often sufficient with current functionals, as long as no external magnetic field is applied.

However, dealing with spins explicitly can become important in many cases: examples are metallic wires or clusters with an odd number of electrons or clusters and molecules with a ground state with finite spin. The same applies, when molecules are charged between contacts and single electrons are pulled onto the molecule by a gate field as we will investigate in chapter 9.

A second advantage is the possibility of including additional physics into the approximation for the not exactly known exchange-correlation functional  $E_{xc}$ , e.g., relativistic corrections like spin-orbit coupling.

The extension of DFT to the treatment of separate spins is called Spin Density Functional Theory (SDFT) or Unrestricted Kohn–Sham (UKS). The procedure is straightforward (see e.g. [77], a formal justification can be found in [82]).

Two separate densities,  $n_\alpha$  and  $n_\beta$  for spins  $\sigma = \alpha, \beta$ , are introduced, which sum up to the total electron density,  $n = n_\alpha + n_\beta$ . With these, the energy functional can be extended to two spin subspaces, taking the form

$$E[n_\alpha, n_\beta] \equiv T_S[n_\alpha, n_\beta] + V_H[n_\alpha, n_\beta] + E_{xc}[n_\alpha, n_\beta] + \int d^3r v(\mathbf{r})(n_\alpha + n_\beta) \quad (4.24)$$

with expressions for  $T_S, V_H$  analogous to the standard DFT case above. The exchange–correlation functional  $E_{xc}[n]$  is modified to account for the spin, and additional corrections (like spin–orbit coupling) can be included therein. For calculations in an applied external magnetic field,  $v(\mathbf{r})$  can be modified to include a Zeeman term for the interaction with a magnetic field.

The functional can be minimized in the same fashion as for the spin–unresolved case. Two effective potentials  $v_{\text{eff}}^\sigma(\mathbf{r})$  are introduced, yielding two sets of coupled Kohn–Sham equations of the form

$$\begin{aligned} \left(-\frac{1}{2}\nabla^2 + v_{\text{eff}}^\alpha(\mathbf{r}) - \varepsilon_j^\alpha\right) \phi_j^\alpha(\mathbf{r}) &= 0 \\ \left(-\frac{1}{2}\nabla^2 + v_{\text{eff}}^\beta(\mathbf{r}) - \varepsilon_j^\beta\right) \phi_j^\beta(\mathbf{r}) &= 0. \end{aligned} \quad (4.25)$$

The coupling is done via the effective potential

$$v_{\text{eff}}^\sigma(\vec{r}) = v(\vec{r}) + v_H(\vec{r}) + \frac{\delta E_{xc}[n_\alpha, n_\beta]}{\delta n_\sigma(\vec{r})} \quad (4.26)$$

When solving the self–consistent equations 4.25, now in addition to the variation of the trial wavefunctions  $\phi_j^\sigma(\mathbf{r})$  the number of  $\alpha$ – and  $\beta$ –spin electrons has to be varied under the constraint of particle conservation.

## 4.5 The derivative discontinuity

A known problem of currently used functionals in Density Functional Theory is the incorrect value for the energy gap between the highest occupied molecular orbital (HOMO) and the lowest unoccupied molecular orbital (LUMO). This gap,  $E_g$ , is defined as the difference between the ionization potential,  $E_I$ , and the electron affinity,  $E_A$ .

The ionization potential and the electron affinity are defined as the total energy difference between the  $(N - 1)$  and  $N$  electron system and the  $N$  and  $(N + 1)$

electron system, respectively. Therefore, the gap can be calculated from the ground-state energies of the systems with  $(N - 1)$ ,  $N$ , and  $(N + 1)$  electrons by

$$E_g = E_I - E_A = E(N + 1) + E(N - 1) - 2E(N) \quad (4.27)$$

One of the reasons for the incorrect value of the gap in DFT is the *derivative discontinuity* [83, 84]. This can be understood by looking at the chemical potential  $\mu$ , defined

$$\mu_N = \frac{\partial E_V[n_N]}{\partial N}. \quad (4.28)$$

Looking at this equation, we have to generalize the DFT scheme to fractional particle numbers in order to calculate the chemical potential. The simplest way to do this, is to introduce a statistical superposition of the  $N$  and  $(N + 1)$  electron states in the energy functional. In ensemble DFT (see e.g. [77]) the restriction to integer occupation numbers is lifted in general, and ensembles with fractional occupation numbers are treated. For a superposition of two states to represent a system of  $N + \eta$  particles, the energy functional,  $E_V[n]$ , of eq. 4.10 can be generalized by modifying the Hohenberg–Kohn functional,  $F_{HK}$ , in the following way:

$$F_{HK}[n] \equiv \min_{\tilde{\psi}_N, \tilde{\psi}_{N+1}} \left\{ (1 - \eta) \langle \tilde{\psi}_N | T + V_{ee} | \tilde{\psi}_N \rangle + \eta \langle \tilde{\psi}_{N+1} | T + V_{ee} | \tilde{\psi}_{N+1} \rangle \right\} \quad (4.29)$$

The variation is restricted to those combinations of  $|\tilde{\psi}_N\rangle$  and  $|\tilde{\psi}_{N+1}\rangle$  that yield the prescribed density  $n$ .

If we now examine the chemical potential  $\mu(N)$  more closely, we see that it is linear for values of  $N$  between two neighboring integer particle numbers, but at integer values a discontinuity is observed as the slopes are different:

$$\mu(N - \eta) = E(N) - E(N - 1) = -E_I \quad (4.30)$$

$$\mu(N + \eta) = E(N + 1) - E(N) = -E_A \quad (4.31)$$

This discontinuity is similar to a situation encountered in solid state physics, where in a semiconductor the chemical potential  $\mu$  jumps if one goes through a gap in the spectrum when adding electrons. In the case of DFT, the discontinuity implies that the functional derivative of the total energy functional  $E[n]$  itself, shows a discontinuity at integer values. This is the so-called *derivative discontinuity*.

The gap can also be expressed as the gap of the Kohn–Sham system,  $E_g^{KS} = \varepsilon_{N+1} - \varepsilon_N$  for the  $N$ -electron system plus additional corrections

$$E_g = E_g^{KS} + \Delta_{xc} \quad (4.32)$$

where the corrections are termed *derivative discontinuity*,  $\Delta_{xc}$ , and are given by

$$\Delta_{xc} = \lim_{\eta \rightarrow 0^+} \left( \frac{\delta E_{xc}[n]}{\delta n} \Big|_{N+\eta} - \frac{\delta E_{xc}[n]}{\delta n} \Big|_{N-\eta} \right). \quad (4.33)$$

The derivative discontinuity will become important when we are investigating charging effects on single molecules between gold contacts via gate electrodes (see chapter 9). In that situation it can partially obfuscate Coulomb blockade effects — since the particle number on the only weakly coupled molecule might increase gradually in non-integer steps when varying the gate voltage.

## 4.6 Practical implementation of the Kohn–Sham scheme in TURBOMOLE

As we have seen above in §4.3, the tremendous gain in numerical efficiency in DFT stems from going from the direct variation of the density to a representation of the density in an orbital picture, where the particles are non-interacting.

The Kohn–Sham equations are written in terms of wavefunctions instead of a direct variation of the density. These self-consistent equations (4.20, 4.22, and 4.23) have to be solved in an iterative scheme until convergence is reached. To do this in a numerically efficient way, the wavefunctions  $\phi_i$  are expanded in a predefined *finite* basis set  $\{\varphi_i\}$ .

$$\phi_i = \sum_{\nu} c_{\nu i} \varphi_{\nu} \quad (4.34)$$

This finite basis set has to be as small as possible — but still large enough to span the space of possible, and “important” trial densities sufficiently well — to be able to cope with the numerical effort. We will describe below, in §4.6.1, how such a basis set is chosen in an appropriate way.

Using the wavefunctions  $\phi_i$ , expanded in basis  $\{\varphi_i\}$ , the set of Kohn–Sham equations 4.22 can be written as

$$\hat{o}^{KS}(\mathbf{r}) \sum_{\nu} c_{\nu i} \varphi_{\nu}(\mathbf{r}) = \varepsilon_i \sum_{\nu} c_{\nu i} \varphi_{\nu}(\mathbf{r}) \quad (4.35)$$

with a Kohn–Sham operator

$$\hat{o}^{KS} = \left(-\frac{1}{2}\nabla^2 + v_{\text{eff}}(\mathbf{r})\right). \quad (4.36)$$

The set of equations (4.35) for the wavefunctions  $\phi_i(\mathbf{r})$  can be combined into a matrix notation

$$O^{KS} \cdot C = S \cdot C \cdot \varepsilon \quad (4.37)$$

by defining a Kohn–Sham matrix

$$O_{\nu\mu}^{KS} = \int d^3r \varphi_\nu(\mathbf{r}) \hat{o}^{KS}(\mathbf{r}) \varphi_\mu(\mathbf{r}), \quad (4.38)$$

and an overlap matrix

$$S_{\mu\nu} = \int d^3r \varphi_\nu(\mathbf{r}) \varphi_\mu(\mathbf{r}). \quad (4.39)$$

The matrix  $\mathbf{C}$  consists of the expansion coefficients  $c_{\nu i}$  of the wavefunctions and  $\varepsilon$  is a diagonal matrix containing the eigenenergies  $\varepsilon_i$ .

This set of algebraic equations can then be solved by numerically efficient algorithms. For a description of the program package TURBOMOLE, which was used within this work, see e.g. [69, 85].

### 4.6.1 Optimized basis sets for DFT

In general, the wavefunctions used to construct the electron density can be expanded in any choice of basis set. To minimize the computational effort, a set of as few basis functions as possible is desirable. The quality of the basis set is gauged by how well the constructed wave functions are able to yield the physical density. In many cases, one tries to put physical meaning to the basis sets as well by constructing functions that resemble the real atomic orbitals as closely as possible.

In addition the resulting wave–functions should be easy to treat numerically.

For molecules, this leads to the use of a superposition of gaussians in combination with an angular dependence in the form of spherical harmonics ( $f_\mu(\vartheta, \varphi)$ ). The resulting functions are called *contracted gaussians*:

$$\phi_\mu(\mathbf{r}) = \sum_\nu c_{\mu\nu} N_\nu \mathbf{f}_\mu(\vartheta, \varphi) \mathbf{e}^{(-\alpha_\nu \mathbf{r}^2)} \quad (4.40)$$

with the normalization constant  $N_\nu$  and contraction factor  $c_{\mu\nu}$ . The individual gaussians are characterized by their decay constant  $\alpha_\nu$ .

By contracting several gaussians into one *contracted gaussian* basis function, the numerical effort can be reduced greatly, while at the same time using the appropriate combination makes the resulting loss in accuracy controllable [86].

In most basis sets, the gaussians of the inner electrons are contracted into one single, contracted gaussian basis function without a significant loss in accuracy [87]. The number of basis functions per atom is usually larger than the number of valence orbitals to improve the phase-space of possible electron densities.

We will now describe in brief the basis sets available in TURBOMOLE [85,88,89], which we used for the calculations in this work. More information on the choice of basis sets can be found in [86].

- **Split valence polarization (SV–P)** [89]

This is a fully optimized contracted gaussian basis set for all atoms used in our calculations. It constitutes the smallest possible basis set to yield quantitatively good results in the case of no external fields. The inner electrons are all contracted into one basis function [87].

Beyond, it contains just two (one in the case of hydrogen) uncontracted gaussian orbitals in the valence shell. A basis function accounting for polarization effects is added, as this is necessary to describe the interatomic bonds adequately when molecules instead of single atoms are treated. This function has the angular momentum quantum number equal to the highest of the valence shell plus one [87].

In summary, this constitutes the minimal choice, sufficient for reliable calculation of the electronic structure while at the same time being numerically the most efficient. In accuracy it is comparable (or slightly better) to the *Pople 631-G\** basis sets. For the simple organic molecules used in our calculations, it provides excellent results as long as no external fields are applied.

- **TZVPP** [90]

TZVPP stands for *triple-zeta valence plus double polarization*. Here, in addition to the single contracted gaussian for the inner electrons, three contracted gaussians per valence shell are included [90]. In addition a large set of polarization functions is also incorporated.

This set was originally developed for higher correlated methods like MP2 or Configuration Interaction, but the large amount of polarization basis functions is also well suited to describe molecules in external fields. The lowest angular quantum number of the polarization functions equals the highest angular quantum number of the valence shell plus one, e.g. for carbon this would be *d*-functions. In all, there are 4 polarization functions added per atom (2d2f in the case of carbon) [87].

This constitutes the most complete basis set for our purposes. It is well suited to describe situations, where polarization becomes important,

e.g., when an electric field is applied (as in chapter 10), or when a gate electrode is included in the DFT calculation as described in chapter 9.

### 4.6.2 Effective core potentials

The computational effort grows with the amount of electrons taken into account for a DFT calculation. When treating heavier elements like gold, it is therefore desirable to individually consider only the electrons of the outer shells that take part in the chemistry.

The overlap of the wave-functions of the inner electrons with the inner electron wave-functions of neighboring atoms is extremely small. In addition, orthogonality of these wave-functions with respect to the outer electron wave-functions ensures that they don't change significantly when chemical bonds are formed [77].

These properties make it possible to freeze the inner electrons of the closed shells in a *frozen-core* approximation. Here, these electrons are combined with the atomic nucleus to yield an effective ion-core potential. The used pseudopotentials then lead to orbitals that are equal to the original ones beyond some fixed radius. For distances from the nucleus below that distance, the pseudo-orbitals are chosen to be free of unwanted nodes and oscillations to facilitate construction of the basis set [88, 91]. See e.g. [92] for a discussion on the justification and validity of the use of effective core potentials. In our TURBOMOLE calculations we used effective core potentials [88] only for the gold atoms. Only the 19 outermost electrons per atom were treated explicitly in the DFT calculations.

### 4.6.3 The use of fractional occupation numbers to improve convergence

In our DFT calculations, we made use of a special tool of TURBOMOLE, called *mkfermi*. This allows to calculate the occupation numbers at a fictitious finite “temperature”  $T$ , resulting in fractional occupation of orbitals close to the Fermi energy at each iteration step in the TURBOMOLE scheme. The main purpose of this tool is to increase the convergence performance. By smearing out the occupation, many systems converge much faster, and some only converge when this tool is employed.

The occupation,  $n_i \in [0, 1]$ , of a Kohn–Sham orbital with energy,  $\varepsilon_i$ , is calculated by fitting an error function

$$n_i = \frac{1}{2} \operatorname{erfc} \left( \frac{\varepsilon_i - \mu}{fT} \right), \quad (4.41)$$

where  $\mu$  is the Fermi energy. The factor  $f = \frac{4k}{\sqrt{\pi}}$  ensures that the distribution has the same slope at the Fermi energy as the Fermi distribution.

During the iterative scheme in TURBOMOLE, the calculation of fractional occupation numbers is started, when the current HOMO–LUMO gap drops below a predefined critical value. Starting from an initial “temperature”,  $T_i$ , usually 300 to 500 K, fractional occupation numbers are calculated in each iteration, while the temperature is decreased by a factor of usually 0.9 in each step until it reaches the final “temperature”,  $T_f$ . Choosing  $T_f$  low enough, like 10 to 50 K, ensures, that the final occupation numbers are of integer value.

This scheme turned out to be extremely helpful in calculating the more complex metal–(organic molecule)–metal systems, especially in situations where external fields were present, which will be discussed in chapters 9 and 10.

## 4.7 Different approximations for DFT functionals

The Kohn–Sham formalism is a formal mathematical framework for solving the electronic structure of an interacting electron system. To make practical use of it, we require numerically effective and at the same time physically sufficient approximations to the exchange–correlation energy functional  $E_{xc}[n(\mathbf{r})]$ . Most approximations currently in use are of quasilocall form, as this reduces the numerical effort enormously.

Usually  $E_{xc}[n(\mathbf{r})]$  is written in the form

$$E_{xc}[n(\mathbf{r})] = \int d^3r' d^3r e_{xc}(\mathbf{r}, [n(\mathbf{r}')])n(\mathbf{r}) \quad (4.42)$$

where the exchange energy per particle  $e_{xc}(\mathbf{r}, [n(\mathbf{r}')])$  depends primarily on the density near the point  $\mathbf{r}$ . Near means within a length scale corresponding to the Thomas Fermi screening length  $(\lambda_{TF} = (\frac{4\pi}{\rho_0 e^2})^{\frac{1}{2}})$ , with  $\rho_0$  being the density of states) [76].

### 4.7.1 Local Density Approximation (LDA)

The simplest form for an approximate exchange–correlation functional was already proposed in 1965 by Kohn and Sham [75]: the *Local Density Approximation* (LDA). Here, the exchange–correlation energy  $e_{xc}(\mathbf{r}, [\mathbf{n}])$  is replaced by the exchange correlation energy  $e_{xc}(n)$  of a uniform electron gas of density  $n$ . This leads to the local function

$$E_{xc}^{LDA}[n(\mathbf{r})] \equiv \int d^3r n(\mathbf{r})e_{xc}(n(\mathbf{r})) \quad (4.43)$$

The Dirac exchange (see e.g. [78]) and correlation part [93] are given in atomic units by

$$e_x(n) = -\frac{3k_F}{4\pi} = -\frac{0.458}{r_s} \quad (4.44)$$

$$e_c(n) = -\frac{0.44}{r_s + 7.8} \quad (4.45)$$

where  $r_s$  is the Wigner–Seitz radius ( $n^{-1} = 4\pi/3r_s^3$ ) and  $k_F$  the Fermi wavevector. The correlation part is obtained from an interpolation formula connecting the high density and low density limit of the uniform electron gas [94]. The corresponding fitting parameters can be obtained from Quantum Monte–Carlo simulations [93].

The exchange energy in the LDA approximation is usually accurate to within  $\sim 10\%$ , but the much smaller correlation energy is generally overestimated by a factor of two [76]. These two errors partially cancel each other in most cases in a systematic way and thereby improve the accuracy of LDA [76]. The derivative discontinuity (see §4.5) is a problem in LDA.

The numerical efficiency of the Kohn–Sham equations in LDA is much better than solving the Hartree–Fock equations as the Kohn–Sham equations are effective single–particle equations, whereas Hartree–Fock includes the Coulomb term of the electron–electron interaction.

Even though LDA was expected to be applicable only to electronic systems with slowly (on the scales of the local Fermi wavelength) varying density, it turned out to be much more powerful. In atomic and molecular systems, the density is often strongly inhomogeneous, but still LDA has been found to give very reasonable results [76, 78].

Bond–lengths and geometries of molecules are usually predicted within an error of only 1% [87, 95], but for ionization energies in atoms and molecules, which are only accurate to about 10–20% in LDA, corrections are of utmost importance. For this reason, the use of DFT in quantum chemistry started only

after the development of corrections beyond LDA, like the Generalized Gradient Approximation and later hybrid functionals. Especially in heavy-fermion systems, dominated by electron-electron interaction, LDA is not applicable, it, e.g., gives a wrong band gap. In many solid state systems, however, LDA still proves to be a very useful and often sufficient tool. Especially in metallic structures, the uniform electron gas is a reasonable assumption and results of LDA for the electron density/electronic structure agree very well with experimental values. For a more thorough discussion of the quality of LDA (also in the TD-DFT case) and its deficiencies see, e.g., [96]. In some cases better results can be achieved by using localized Hartree-Fock instead of LDA, see, e.g., [97].

### 4.7.2 Beyond LDA: Generalized Gradient Approximation (GGA)

#### The exchange-correlation hole

To describe the improvements of DFT beyond LDA, we introduce the concept of the *exchange-correlation hole*. The exchange-correlation hole describes, by which amount the electron density  $n(\mathbf{r}')$  is decreased at position  $\mathbf{r}'$  due to the presence of an electron at position  $\mathbf{r}$ <sup>1</sup>.

It is written as a hole-density,

$$n_{xc}(\mathbf{r}, \mathbf{r}') = n(\mathbf{r}') - n_0(\mathbf{r}') \quad (4.46)$$

where  $n(\mathbf{r}')$  is the actual electron density at position  $\mathbf{r}'$  in presence of the other electron at  $\mathbf{r}$ , and  $n_0(\mathbf{r}')$  is the fictional density without presence of the other electron at  $\mathbf{r}'$ .

The hole density is normalized to -1:

$$\int d^3r' n_{xc}(\mathbf{r}, \mathbf{r}') = -1,$$

reflecting the total screening of an electron at position  $\mathbf{r}$  by the surrounding depletion of the electron density.

The exchange-correlation hole density can be separated into the different contributions for exchange and correlation analogous to the separation of the energy functional in its contributions from exchange and correlation,  $n_{xc} = n_x + n_c$ . There, the exchange-correlation part is given by the difference

---

<sup>1</sup>The exchange-correlation hole density is related to the pair distribution function (see, e.g., [98])

of the total contribution of the electron–electron interaction to the energy and the Hartree part. The exchange contribution stems from the Pauli principle. The correlation part is the remaining part of the total energy after kinetic, Hartree and exchange contributions have been subtracted. The two holes have the following properties (see e.g. [78] for details):

- Sum rule for the exchange hole:

$$\int d^3r' n_x(\mathbf{r}, \mathbf{r}') = -\mathbf{1}.$$

This stems from the Pauli principle.

- Sum rule for the correlation hole:

$$\int d^3r' n_c(\mathbf{r}, \mathbf{r}') = \mathbf{0}$$

- negativity constraint:

The exchange hole is always negative, as the electron density at  $\mathbf{r}'$  is always decreased by an electron at  $\mathbf{r}$ .

All these are fulfilled by the simple LDA approximation, which is one of reasons that LDA is that successful. Most approximations for the exchange–correlation functional are obtained from analyzing hole properties of present approximations and suggesting improvements, or are written in terms of the (average) exchange–correlation hole.

## Generalized Gradient Approximation (GGA)

It was identified from early on that LDA is too simplistic to work for many systems with strongly varying density. An extension was already proposed by Hohenberg and Kohn in their original paper on DFT [74]: the *gradient expansion approximation* (GEA). The idea is to expand the functional  $F_{xc}[n]$  in the electron density  $n(\mathbf{r})$  and include first order corrections,  $\nabla n(\mathbf{r})$ .

First implementations for atoms and molecules were a complete failure. In GEA, the sum rule of the exchange–correlation hole as well as the non-negativity constraint were violated, resulting in a incorrect treatment of the correlation and Pauli principle physics, worse than in the simpler LDA. But, experience with GEA provided the basis for the *generalized gradient approximation* (GGA), which is currently one of the most popular types of exchange–correlation functionals.

Based on work by *Langreth and Mehl* [99, 100], this improved functional was developed by Perdew *et al.* [101, 102], who devised a cutoff procedure for the gradient expansion in real space. This procedure sharply terminates the GEA exchange–correlation hole. This way it is possible to ensure the sum rule of the exchange–correlation hole as well as the negativity condition, resulting in a more appropriate treatment of the correlation physics in the functional. The GGA corrections to  $E_{xc}$  can be written as an analytical function, called the enhancement factor  $F_{xc}[n(\mathbf{r}), \nabla n(\mathbf{r})]$  which modifies the LDA density leading to the new exchange–correlation functional

$$E_{xc}^{GGA}[n(\mathbf{r})] = \int d^3r n(\mathbf{r}) e_{xc}^{\text{unif}}[n(\mathbf{r}) F_{xc}[n(\mathbf{r}), \nabla n(\mathbf{r})]]. \quad (4.47)$$

Usually the functional  $F_{xc}$  is written as a function of the Wigner–Seitz radius  $r_s$  and a dimensionless reduced density gradient  $s(\mathbf{r})$ ,

$$s(\mathbf{r}) = \frac{|\nabla n(\mathbf{r})|}{2k_F(\mathbf{r})n(\mathbf{r})} \quad (4.48)$$

with the Fermi wavevector  $k_F$ .

The actual form of  $F_{xc}$  is then derived by fitting the functional to experimental data. A second way is to construct it without any semi–empirical parameters from the limiting case of a slowly varying electron gas [103]. This cutoff–procedure turned out to be very successful in improving DFT. Most notably was the reduction in the over-binding character of the functional for molecules [77, 101]. There, LDA did always overestimate the binding energy, resulting in a HOMO–LUMO gap that was far too big. The derivative discontinuity (§4.5), however, is still a problem in GGA.

### 4.7.3 Extensions: exact exchange and hybrid functionals

#### Exact exchange

In DFT in the LDA or GGA approximation, each electron interacts with itself via the Coulomb electrostatic potential in the Hartree term  $V_H$ . This unphysical interaction is called the *self–interaction problem*. In the exact formalism (using an exact exchange–correlation energy,  $E_{xc}$ ) this fictitious term would be canceled exactly by a contribution from the exchange–correlation energy. In LDA, this cancellation is incomplete. This deficit led to the development of self–interaction corrected functionals [94](see e.g., [77] for an introduction).

Self–interaction errors can be avoided by calculating the exchange part of  $E_{xc}$  exactly. The exact exchange is evaluated using the Hartree–Fock description,

but thereby the Kohn–Sham wavefunctions instead of the wavefunctions from a nonlocal Hartree–Fock potential are used.

$$E_x^{\text{exact}}[n] = -\frac{1}{2} \sum_i^{\text{occ}} \sum_j^{\text{occ}} \int d^3r d^3r' \frac{\phi_i^*([n], \mathbf{r}') \phi_j^*([\mathbf{n}], \mathbf{r}) \phi_j([\mathbf{n}], \mathbf{r}') \phi_i([\mathbf{n}], \mathbf{r})}{|\mathbf{r} - \mathbf{r}'|}. \quad (4.49)$$

There are now no errors from artificial self–interaction contributions, but as the correlation part is still approximated, we now do acquire an additional error due to the fact that the systematic cancellation of errors in  $E_x$  and  $E_c$  no longer applies.

### Hybrid functionals

Many functionals currently in use for DFT calculations of atoms or molecules, are so–called hybrid functionals. Here, several approximations for the exchange–correlation functional are combined with various weights to result in a mixed functional that gives much more realistic results for molecular systems. For example, Hartree–Fock/exact–exchange contributions can be mixed into the functional. Using reference data from experiments, wave–function methods and other highly correlated methods, the combined functional is empirically fitted to yield the best result possible.

One popular functional in this class is B3LYP [104, 105]. This functional consists of GGA plus a 20 % exact–exchange contribution. It delivers excellent results for organic molecules, being better than results from GGA type functional like BP86. Due to the exact exchange contribution, the over–binding is reduced. But, when metal atoms are included (as in the clusters that form the extended molecule in our calculations) B3LYP is much less accurate than Becke–Perdew. This stems from the failure of Hartree–Fock in metallic systems. Some transport calculations for molecules are based on B3LYP, e.g. *Heurich et al.* [72], but when parts of the leads are to be included in the calculation of the central cluster, they are predestined to deliver wrong results.

Popular functionals used in quantum chemistry DFT calculations today are for example BP86 [102, 106], PBE [103, 107, 108] or B3LYP [104–106]. Most DFT program packages allow for the use of several of these functionals.

#### 4.7.4 Functionals used within this work

Within this work, we performed all DFT calculations with the program package TURBOMOLE, which offers a large choice of DFT functionals. In our

calculations we employed, unless otherwise stated, the GGA type functional BP86 (*Becke–Perdew*) [106, 109]. This widely used functional yields good results throughout the whole of chemistry. It constitutes a good balance between correct structure parameters like bond lengths and bond angles on the one hand and bond energies and electron densities on the other hand. There exist many other, often more sophisticated functionals that yield better results for a special task, like structure calculations or bond energies, or that are specialized for a subspace of selected molecules. Most of them belong to the class of hybrid functionals.

For our purposes, however, where we need to calculate combined systems of organic molecules and metal clusters, the balanced Becke–Perdew GGA type functional is suited best. In some cases, we used the PBE functional instead, as this gives a better description of systems where van–der Waals interactions are of importance. For comparison, we also performed some calculations with a *Hartree–Fock* functional [110, 111] (see §7.1).

## 4.8 Physical quantities given exactly in Density Functional Theory

- **Ground–state energy**

The ground–state energy is per construction exact, if the exact exchange–correlation functional is known. This is what DFT was invented for. Currently used functionals give results of very high quality for the ground–state energy.

- **Ground–state density**

As we have discussed in detail above, the Hohenberg–Kohn theorem (§4.2.1) states that the ground–state density is in principle exact, if the exact exchange–correlation potential is known. Even though in practice this is not exactly known, modern functionals give excellent quantitative results for the ground–state electron density of molecular systems [76].

- **Energy of the highest occupied molecular orbital (HOMO)/ionization energy**

In addition to the ground–state density, the Hohenberg–Kohn theorem only makes a statement for the ground–state energy, which is by construction exact. There is no direct conclusion on the physical meaning of the individual eigenvalues of the fictitious Kohn–Sham system.

It was shown in 1985 by *Almbladh* and *van Barth* [112] that in addition to the electron density, DFT in principle also provides exact results for

the ionization energy, which equals the energy of the highest occupied molecular orbital (HOMO). We won't give a derivation here, but will only mention the ideas behind the proof:

The idea is to consider the true many-body system and the corresponding Kohn-Sham system at the same time and derive for both the asymptotic form of the density matrix for large distances  $\mathbf{r}$  from the finite system. For the many body system the density matrix decays exponentially at large distances and the decay constant is determined by the highest lying state only. Thereby the exponent  $\kappa$  relates simply to the ionization potential by

$$\frac{\kappa^2}{2} = E(N - 1) - E(N) = E_{\text{ionisation}}. \quad (4.50)$$

$E(N)$  and  $E(N - 1)$  are the ground-state energies of the  $N$  electron and  $N - 1$  electron system, respectively.

In the case of the effective single-particle system, the decay of the density at large distances is governed by the highest lying eigenstate of the Kohn-Sham system. By comparing these two asymptotic forms with each other, it can be deduced that the HOMO of DFT equals the ionization energy of the corresponding many-body system. Thus, in addition to the density, the energy of the HOMO of the Kohn-Sham system is in principle exact as well.

## 4.9 Other quantities

- **Energy levels of the Kohn-Sham states**

From the Hohenberg-Kohn theorem we can only infer that the ground state energy, obtained from minimizing the Hohenberg-Kohn functional, has a physical meaning. In addition, we have now learned above, that the HOMO energy  $\varepsilon_N$  is in principle exact. All other eigenvalues are strictly speaking of no physical meaning at all.

For metallic systems, the eigenvalues of the states close to the Fermi energy are close to the physical values. For non-metallic systems this is not always true. But still, in many cases these eigenvalues are in close agreement with the experimental values.

- **Kohn-Sham wavefunctions**

In general, the Kohn-Sham wavefunctions of the effective single-particle system that yields the same density as the real many-body system do not have any transparent physical meaning. By definition they are the

wavefunctions  $\phi_i(\mathbf{r})$  of the single-particle system that yield the correct ground-state density  $n(\mathbf{r})$  via

$$n(\mathbf{r}) = \sum_{\mathbf{i}} |\phi_{\mathbf{i}}(\mathbf{r})|^2 \quad (4.51)$$

while minimizing the kinetic energy  $T_s[n(\mathbf{r})]$ .

In DFT-based transport calculations, we approximate the true ground-state by a single Slater-determinant. However, in general the true ground-state will be a superposition of many Kohn-Sham Slater-determinants. Vice versa, the single Slater-determinant approximation then describes a many-body state that is not the real ground-state, but a linear combination of the true ground-state and excitations. The mixture of the latter tends to produce wavefunctions that are more extended than the ground-state of the real system. The observed transport behavior turns out to be too metallic.

- **Energies of the unoccupied orbitals**

In standard DFT calculations, these are usually quite inaccurate. One of the reasons is the derivative discontinuity (see §4.5). Accuracy can be increased tremendously by using DFT methods that include excited states.

## 4.10 Time-dependent Density Functional Theory (TD-DFT)

Under quite general conditions (see 4.10.1 below) a theorem, analogous to the Hohenberg-Kohn theorem of DFT can be formulated for time-dependent external potentials. This extension is called the Runge-Gross theorem of time dependent density functional theory (TD-DFT) [113]. It states, that a one to one correspondence between time-dependent densities  $n(\mathbf{r}, t)$  and time-dependent external single-particle potentials  $v_{\text{ext}}(\mathbf{r}, t)$  can be established.

This then allows again to define a fictitious system of non-interacting electrons moving in an effective Kohn-Sham potential, which yields the same density as that of the real system. The exchange-correlation potential is defined in an analogous way, but now, it depends not only on the density at time  $t$ , but on the entire history of the density  $n(\mathbf{r}, t)$ . It also depends on the initial wavefunction of the interacting system at  $t = 0$ , as well as the initial Kohn-Sham wavefunction. This makes the functional much more complicated to deal with.

### 4.10.1 Runge–Gross theorem

The Hohenberg–Kohn theorem for a system of  $N$  non-relativistic, interacting electrons moving in an external potential can be extended to the time-dependent case in the following way [113]:

We assume two different external potentials  $v_1(\mathbf{r}, t), v_2(\mathbf{r}, t)$ , both Taylor-expandable around their initial values at  $t = 0$ . If they differ by more than a purely time-dependent function

$$\Delta v_1(\mathbf{r}, t) \equiv v_1(\mathbf{r}, t) - v_2(\mathbf{r}, t) \neq c(t) \quad (4.52)$$

then, the two densities  $n(\mathbf{r}, t)$  and  $n'(\mathbf{r}, t)$ , evolving under these two external potentials  $v_1, v_2$  from the common initial state  $\psi_0(t=0)$ , are always different.

This is the *Runge–Gross Theorem* of time-dependent Density Functional Theory [113].

### 4.10.2 Time-dependent Kohn–Sham equations

After establishing the one to one correspondence between density and potential, one can construct again an auxiliary system of non-interacting particles obeying the now time-dependent Kohn–Sham equations [113]

$$i\dot{\phi}_i(\mathbf{r}, t) = \left( -\frac{\nabla^2}{2} + v_{\text{eff}}[n(\mathbf{r}, t)] \right) \phi_i(\mathbf{r}, t) \quad (4.53)$$

with the density given by

$$n(\mathbf{r}, t) = \sum_{i=1}^N |\phi_i(\mathbf{r}, t)|^2. \quad (4.54)$$

Again,  $\phi_i(\mathbf{r}, t)$  are the Kohn–Sham single-particle wavefunctions. The exchange–correlation potential is defined in analogy to eq. 4.20 via the effective potential

$$v_{\text{eff}}(\mathbf{r}, t) = v(\mathbf{r}, t) + v_H(\mathbf{r}, t) + v_{xc}(\mathbf{r}, t). \quad (4.55)$$

But here, the Hartree potential  $v_H$  from eq. 4.20 is time-dependent due to the time-dependent density.

The exchange–correlation functional now is much more complex. It depends on the whole history of the density and the initial state  $\phi(t = 0)$  of the Kohn–Sham system as well as on the initial state  $\psi(t = 0)$  of the physical system.

$$v_{xc}[n(\mathbf{r}, \mathbf{t}), \psi(\mathbf{0}), \phi(\mathbf{0})](\mathbf{r}, \mathbf{t}) = \mathbf{v}_{\text{eff}}[\mathbf{n}, \phi(\mathbf{0})](\mathbf{r}, \mathbf{t}) - \mathbf{v}_{\text{ext}}(\mathbf{r}, \mathbf{t}) - \mathbf{v}_{\mathbf{H}}[\mathbf{n}](\mathbf{r}, \mathbf{t}) \quad (4.56)$$

If it were known exactly, it would provide all information necessary to solve any time-dependent interacting many-electron problems. It is obvious that this functional, even if it were known exactly, would be far too complex to treat numerically, so approximations are needed to render it usable.

For systems starting from a non-degenerate ground-state at  $t = 0$ , the initial wavefunctions are functionals of the initial density (Hohenberg–Kohn theorem I), so the initial state dependence disappears [114]. Then, the exchange–correlation potential only depends on the history of  $n(\mathbf{r}, t)$ . This special case is the so-called *history dependence* case.

In DFT,  $v_{xc}$  is the functional derivative of the exchange–correlation energy  $E_{xc}$  (eq. 4.21), established through the variational principle. It is not as easily possible to establish an analogous term, called exchange–correlation action, in TD-DFT as this leads to causality problems, see e.g. [115], also for methods how to circumvent this problem.

### 4.10.3 Adiabatic approximation (ALDA)

The simplest approximation for the now time-dependent and history-dependent exchange–correlation potential is again done using the uniform electron gas, this results in the *adiabatic local density approximation* (ALDA).

For the adiabatic approximation, we ignore the dependence on the past,  $v_{xc}$  becomes a functional of the instantaneous density. This approximation is applicable for very slowly (adiabatically) varying external potentials. On discussions of the initial-state dependence and history/memory effects see e.g. [114, 116]. Combined with the Local Density Approximation this leads to

$$v_{xc}[n[\mathbf{r}, t]](r_0, t_0) \approx v_{xc}^{\text{unif}}(n(\mathbf{r}_0, t_0)). \quad (4.57)$$

We now neglected all non-locality in time and space. Strictly speaking, this should work only for systems with very small density gradients in  $r$  and  $t$ . However, as we have already seen in the case of ground-state DFT, it here proves again to be useful for a far greater variety of problems, yielding excellent quantitative results.



# Chapter 5

## Testing our implementation

In this chapter we will present a few tests on our implementation to assure that it was correctly done. First, band structure calculations obtained from our Green's function for the leads, which we extracted from the DFT calculation will be compared with reference data. This will ensure, that we have made no technical errors in the calculation of the Green's function. Then, in the second part, we will use the standard benchmark of DFT based transport calculations, namely the investigation of the transmission of atomic gold chains.

### 5.1 Band structure of a gold cluster from DFT — testing a tight-binding representation

Our approach to calculating transport in the scattering approach requires the calculation of the self-energy  $\Sigma$ , describing the coupling to the leads. For the calculation of the self-energy,

$$\Sigma = tg_L t^\dagger \tag{5.1}$$

two ingredients are necessary:

- The unperturbed Green's-function of the semi-infinite, ideal leads,  $g_L$
- The hopping matrix elements,  $t$ .

For details of the calculation, see also §3.3.

The easiest way of obtaining the hopping matrix elements and the Green's-function,  $g_L$  of the semi-infinite leads, would be to use a code with periodic

boundary conditions to model bulk gold, but TURBOMOLE does not support this. As it is desirable to extract all data required for our *ab initio* calculations of transport from the same DFT calculation, we have to go this more complicated way to obtain the ingredients.

The goal of this section is to test the convergence of our construction of the unperturbed Green's-function of the leads as well as for the hopping matrix elements. This will be done by comparing band structure data with reference data from other calculations. This can serve as a check, since the band structure calculations involve the calculation of the hopping matrix elements: in our calculation of the Green's-function, we do reconstruct the hopping Hamiltonian from a large, but finite gold cluster, a *fcc* bi-pyramid.

From DFT calculations, the Kohn-Sham eigenvalues and single-particle states are obtained. As we assume, that the coupling between extended molecule and gold electrodes takes part deep inside the electrodes (due to our large extended molecule), we can use the hopping matrix elements of bulk gold. To calculate those, we reconstruct a tight-binding Hamiltonian from the DFT data, which in general does contain hopping elements from each atom to every other atom. But we restrict ourselves to the central atom and look at the hopping of this atom to the surrounding atoms. To reconstruct a bulk tight-binding Hamiltonian, we assume to sit in the bulk and identify the hopping matrix elements of the central atom with those of all atoms in the bulk. This way a Fourier transform into  $k$ -space is possible. Our band structure data in fig. 5.1 is the result.

There are two parameters, where we have to check the convergence of our procedure:

- We have to check, whether a sufficient number of neighbors is taken into account for the construction of the tight-binding Hamiltonian.
- The size of the gold cluster in DFT has to be large enough for the hopping matrix elements to converge to a bulk value.

Testing several cluster sizes, a bi-pyramid of 146 gold atoms proved to be sufficient to achieve convergence to the bulk limit. The number of neighbors that needed to be considered until convergence was reached, turned out to be 12.

In figure 5.1 we show our results for the band structure obtained from the 146 atom cluster. They agree well with band structure data for bulk *fcc* gold, taken from the Electronic Structure Database (ESDB) [117,118], where the band structure is calculated using DFT with periodic boundary conditions.

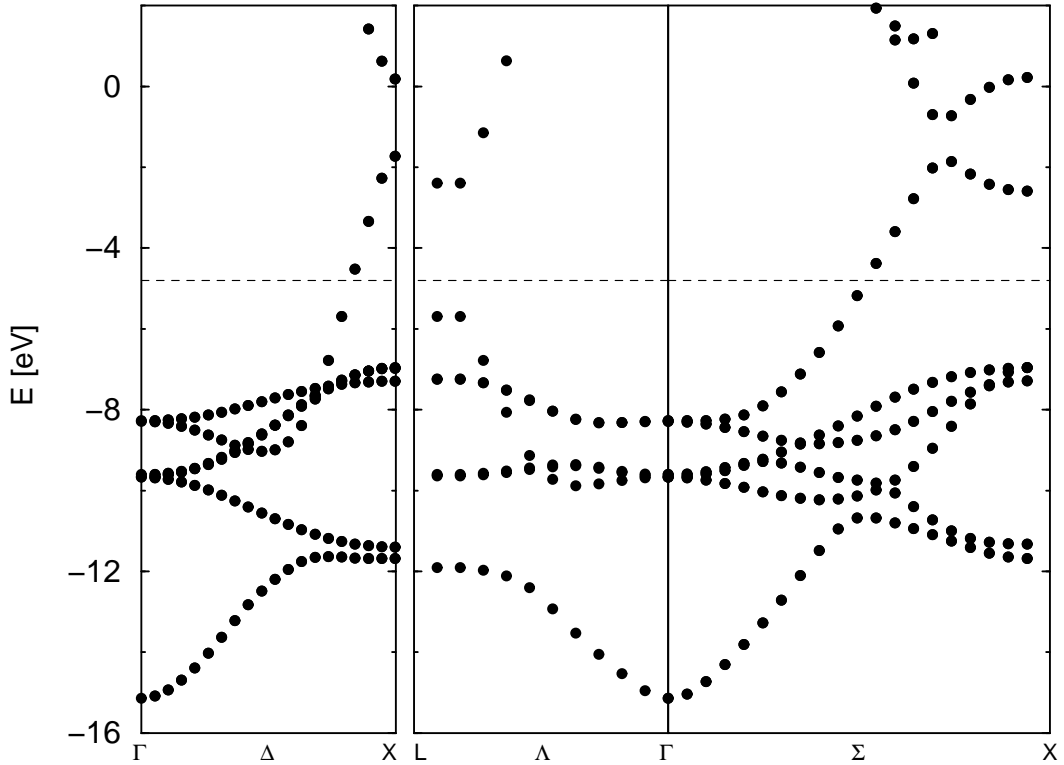


Figure 5.1: Band structure for bulk fcc gold, extracted from our DFT calculation of a fcc bi-pyramid of 146 gold atoms. The Fermi energy / work function ( $-5.1$  eV) is indicated by a dashed line.

The ESDB data is depicted in figure 5.2. Also, the almost constant density of states close to  $E_F$  is well reproduced, see fig. 5.3.

We can conclude that we have obtained a tight binding representation of bulk gold comparable to standard results from periodic boundary condition calculations.

## 5.2 The conductance of atomic wires of gold

Atomic wires are a testing ground for DFT-based transport calculations. The methods of establishing such contacts experimentally have been well established during the last few years so that there exist large amounts of conductance measurements, and investigations on the formation of chains of single atoms using STM techniques or mechanically controlled break junctions, for many different materials like Au, Pt, Nb, Ag, or Al [10, 119–124]. Not all metals do show chain formation. So far, chains have been observed in Au, Pt, and Ir [125]. For gold, the formation of chains stems from relativistic effects.

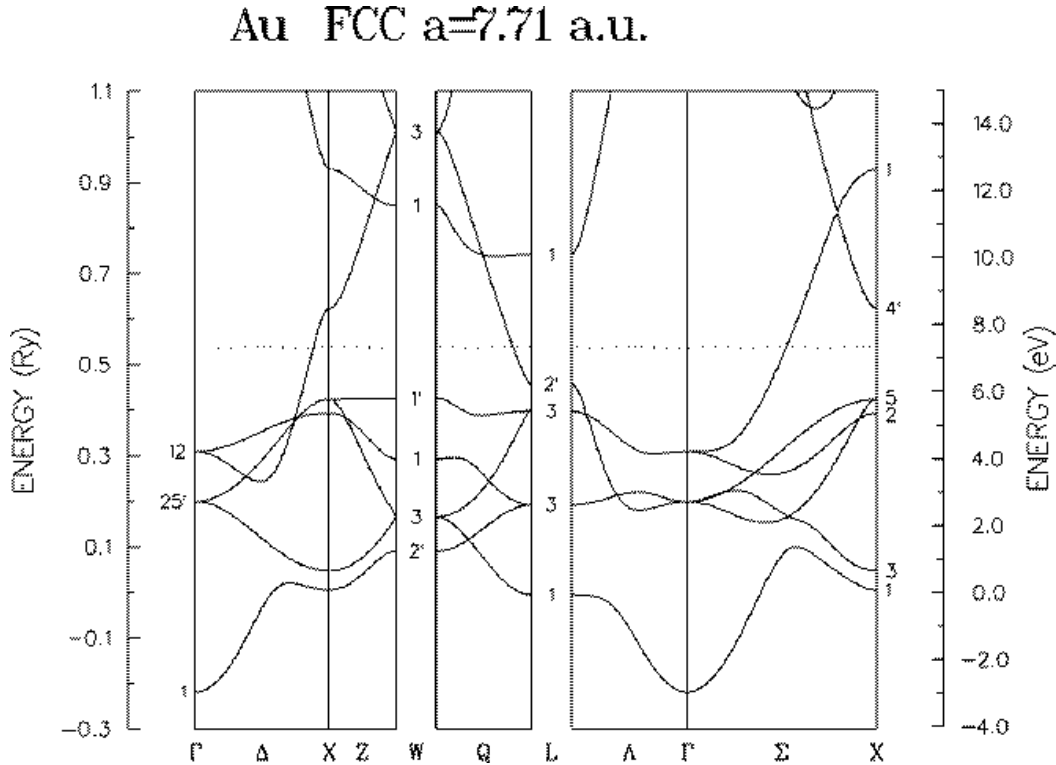


Figure 5.2: Band structure for bulk fcc gold, from the *Electronic Structure Database* [117], tight binding parameterization using the parameters by Papaconstantopoulos [118]. The work function of gold ( $-4.8$  eV) is depicted by a dotted line. For direct comparison with fig. 5.1 an offset of  $12.1$  eV has to be subtracted from the energy values.

Due to the heavy core of the gold atom, relativistic effects lead to  $s$ -orbitals that are closer to the core and energetically closer to the  $d$ -orbitals. They thus hybridize with the  $d$ -orbitals leading to anisotropic  $s$ -orbitals. Due to the anisotropic orbitals, lower coordination numbers are favorable, leading to the formation of chains.

For gold contacts, where chain formation has been observed for the first time [7, 119], the wire exhibits a stepwise decrease in conductance (plateaus), when it is elongated until it breaks (see also §2.2). This has sparked numerous theoretical contributions to explain the observed values of conductance and the steplike conductance behavior when pulling the junctions apart, e.g. [67, 124, 126–128].

On the last plateau, when the contact consists of only a single atom of gold, or a chain of single gold atoms, the contact exhibits a transmission close to  $2\frac{e^2}{h}$  [119–121] over a relatively wide window of bias voltages [121, 125] (up to  $0.5$  V). This indicates the existence of one single propagating mode within the

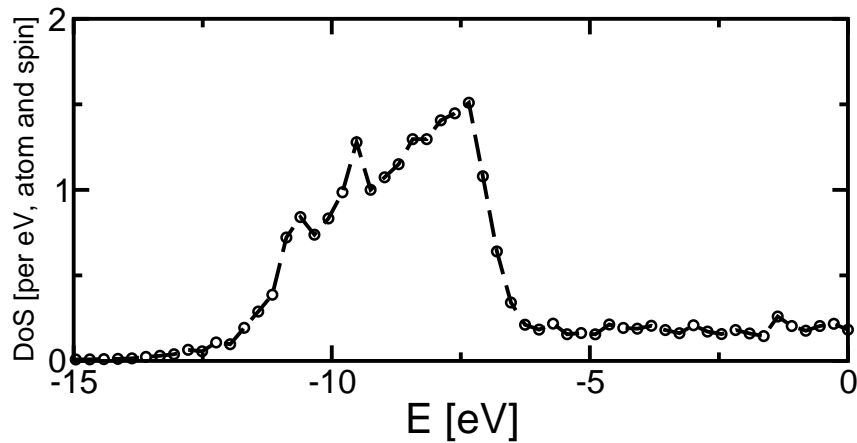


Figure 5.3: Density of States (DoS) for bulk gold. From our DFT calculation of the 146 atom fcc gold bipyramid. Plotted are the states per atom, spin and eV over the energy. Fermi energy,  $E_F \approx -5.1$  eV.

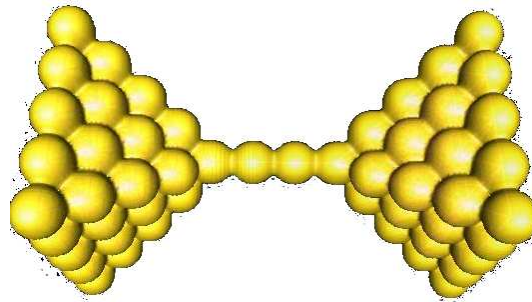


Figure 5.4: 4-atom gold chain. Schematic representation of our extended molecule used in the DFT calculations. The contact consists of the 4-atom chain plus two 54-atom fcc pyramids of gold.

chain, which is contributed by one single valence electron per gold atom (6s electron).

We performed several transport calculations for atomic gold wires of different chain-length and cluster size in order to

- verify that our implementation of transport based on density functional theory reproduces the results of previous calculations published in the literature [67, 127] as well as experimental results [119–121, 125].
- determine the required number of gold atoms to be included in the calculation for the central cluster forming the *extended molecule* (see §3.3.2) to obtain the correct results, and to ensure that the results become independent of the cluster size.
- establish the minimum number of surface atoms that need to be included in the calculation of the self energies: only a portion of the gold atoms included in the extended molecule are required for the coupling, which then strongly reduces the computational effort.

In figure 5.4, we display a picture of the structure used as the central cluster for the ground–state DFT calculation for a 4–atom gold chain. The system consists of the chain itself plus, on both sides, a pyramid of 54 gold atoms each. These pyramids are the additional atoms of the leads that are included in the central cluster to form the *extended molecule*, described in §3.3.2.

Using our Green’s–function formalism, we calculated the transmission  $T$  in dependence of the energy  $E$  in the linear response regime. The structure was allowed to relax completely with the constraint that the 4 central atoms form a chain. Our results for the 4–atom chain of figure 5.4 are displayed in figure 5.5.

Out of the 54 atoms of the pyramids, the two bottom layers, consisting of 41 atoms (4 by 4 and 5 by 5) were used as coupling atoms to define the self–energies for the coupling to the semi–infinite leads. The Fermi energy of the system is about  $-5.1\text{ eV}$ . For comparison, we also plotted the transmission for only 25 coupling atoms (5 by 5 layer). Differences between the two couplings are below 5 %. Using 25 coupling atoms proves to be sufficient to render the transmission independent of the actual number of coupling atoms in the self–energies. In most calculations throughout this work we did indeed even use the larger number of 41 coupling atoms.

For energies around the Fermi energy, the calculated transmission is constant in a wide window and has the value of about  $2\frac{e^2}{h}$  in excellent agreement with the experimental data [120, 121].

In figure 5.6 we display our results for a four atom gold chain with different sizes of contact pyramids. We performed calculations with pyramids of 14, 29, 54 and 84 gold atoms. Using pyramids of 54 gold atoms proved to be more than sufficient. Displayed are the results for 54 ( $\circ$ ) and 84( $\square$ ) atoms. There is no noticeable difference in the conductance for reasonable energy values around the Fermi energy.

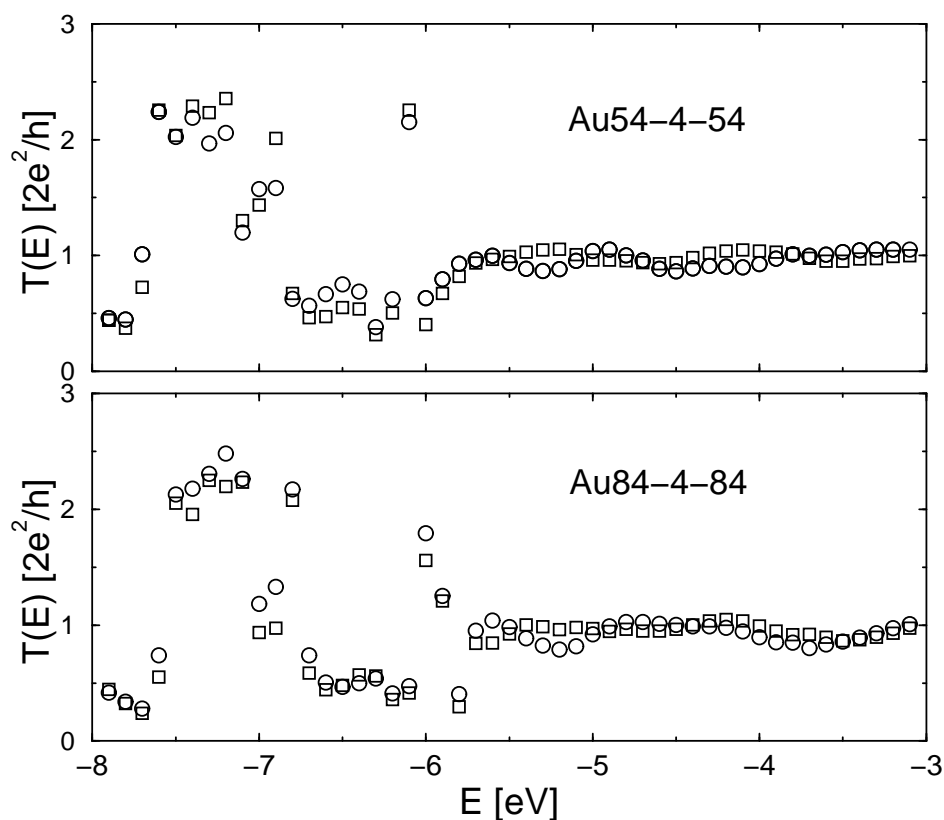


Figure 5.5: Transmission of a 4-atom gold chain. Influence of the number of surface atoms to include in the calculation of the self-energies.

Upper panel: The contacts were made of fcc pyramids of 54 gold atoms each. Out of these, 41 atoms (the 5 by 5 and 4 by 4 bottom layers of the pyramids) were coupled to the leads ( $\square$ ). For comparison, the results with only 25 coupling atoms per contact (5 by 5 layer) are shown as well ( $\circ$ ).

Lower panel: Same as upper panel, but now the contacts consist of pyramids of 84 gold atoms each.

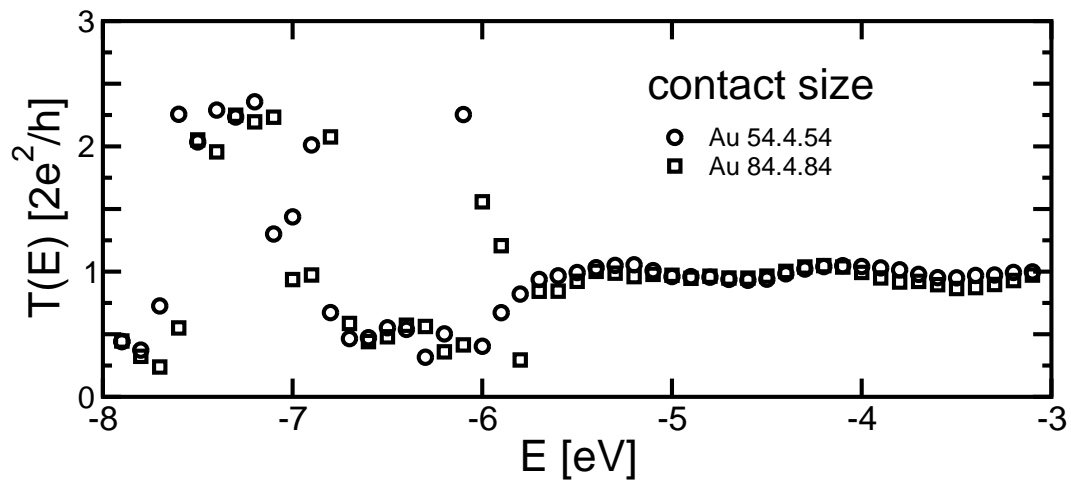


Figure 5.6: Transmission of a 4-atom gold chain (see fig. 5.4). Influence of the contact size on the transmission. The contacts were made of fcc pyramids of 54 ( $\circ$ ) and 84 ( $\square$ ) gold atoms each. Out of these, 41 atoms (the 5 by 5 and 4 by 4 bottom layers of the pyramids) were coupled to the leads. For energies close to the Fermi energy ( $E_F \approx -5.1$  eV), the two traces match perfectly.

## Chapter 6

# DFT-based transport calculations: numerical results and comparison to experiments

This chapter will deal with a selection of our numerical results on the conductance of organic molecules. In the first section we will present data on two example molecules: we will study the paradigm molecule benzene-1,4-dithiol, for which the first single-molecule conductance measurement ever was published [5].

This will be followed by the analysis of a larger, anthracene-based, symmetric molecule that has been measured experimentally at our institute, the Institute for Nanotechnology, Research Center Karlsruhe [11]. This second test case is interesting for several reasons: experiments are expected to be more reliable for larger molecules, as we will see below. Also, DFT is, strictly speaking, only valid close to the uniform electron gas, which is clearly different from the situation in an organic molecule. However, there might be classes of molecules where DFT based calculations yield better and classes where they yield less useful results. Thus, the calculations for this second molecule, exhibiting a larger extended  $\pi$ -system will also be presented.

An analysis of our theoretical data and the comparison with experimental observations will be given. We will see qualitative agreement in one case and point out a quantitative discrepancy between experiment and theory that is inherent to all current DFT based transport calculations.

Several reasons for this discrepancy will be probed. Currently intensely discussed is the influence of the actual microscopics of the contact between the molecule and the electrodes on the transport characteristics. We performed

extensive calculations to provide answers to the key questions arising in this context:

First, in section §6.3 we will present our findings on the influence of mechanical stress on the conductance.

Second, a thorough discussion of the possible types of the chemical bond between the gold electrodes and the terminal sulfur atoms of the measured molecules ( $S - Au_1$ ,  $S - Au_2$  and  $S - Au_3$ ) in a conductance experiment and their influence on the I-V characteristics will be given.

## 6.1 Benzene

The first experiments on the conductance of single molecules were performed on benzene-1,4-di-thiol molecules [5] by *Reed et al.* in 1997. The experiment was conducted using mechanically controlled break-junctions of gold. In the following years, several groups repeated the measurement of transport through benzene using various single-molecule techniques like break-junctions [6, 129], scanning tunneling microscopes (STM) [15], or multi-molecule techniques like nanopores or self-assembled monolayers (SAM)s [130].

One of the reasons for the popularity of the benzene molecule is its simplicity: It contains a highly symmetric, stable extended  $\pi$ -system of just one benzene ring. Also, it is easy to synthesize. Because of its simplicity, one might suspect that the underlying processes that govern the transport through this molecule could be easily understood. However, this turns out not to be the case.

For theoretical calculations, benzene-1,4-di-thiol is an attractive molecule: being small and highly symmetric it reduces the calculational effort. This enables us to compare different approaches (like Hartree-Fock) with DFT based calculations. Also, it is numerically affordable to run many calculations varying parameters like the microscopics of the coupling to the leads. It also constitutes one of the most simple conjugated molecules that forms reliable junctions, to test theoretical calculations against.

Unfortunately, in experiments the small size can be an obstacle: in break-junction experiments, the surface of the gold electrodes is rough due to the breaking of the wire to form the electrodes. For a break-junction experiment to be successful, the molecule needs to be of rigid, rod like structure [11, 12]. Benzene is the limiting case for this condition, as its size is comparable to the surface roughness. Thus, parallel conduction/short-circuits are possible.

Benzol might be a useful simple molecule for understanding fundamental processes in transport through single molecules, but it can only constitute a first

step, as for functionalized molecules acting as diodes or switches, larger structures are needed. Nonetheless, for theoretical works benzene-di-thiol remains the paradigm molecule to test implementations of transport formalisms for molecules.

### Theoretical results

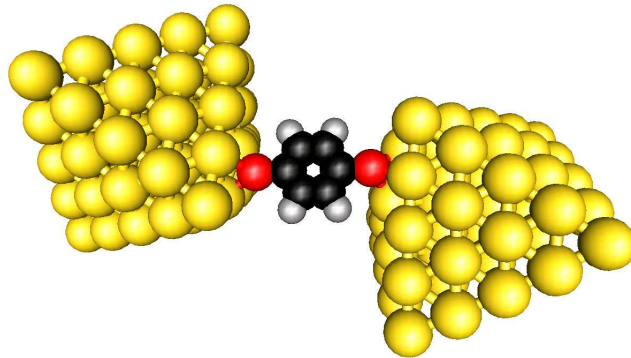


*Figure 6.1: Structure of the relaxed extended molecule for our benzene-1,4-dithiol transport calculations. The gold electrodes consist of 55 gold atoms each. The structure of the molecule was allowed to relax in the DFT calculations. Red: sulfur, black: carbon, grey: hydrogen, yellow: gold.*

Currently, ground-state density functional theory in combination with the Landauer–Büttiker formalism is the most widely used approach to numerical transport calculations for single molecule junctions [60, 61, 66–68, 72, 73, 131–138]. For the molecule benzene, many calculations can be found in the literature [72, 133, 135, 136].

For our transport calculations of the molecules, we used pyramids of 55 gold atoms each as parts of the leads to include in the DFT calculation of the *extended molecule* as we have described above in §3.3.2. This proved sufficient to avoid artefacts from the coupling to the leads via the self-energies. Fig. 6.1 depicts the geometry of the benzene molecule in between the gold contacts. The structure of the molecule and the geometry of the coupling to the gold pyramids was allowed to relax completely in the DFT. The sulfur is coupled to three gold atoms in the hollow position, the coupling distance is  $\approx 2.4 \text{ \AA}$ . Our results for the transmission in dependence of the energy for benzene-1,4-dithiol are presented in fig. 6.2, left.

The zero bias transmission in our calculation is about  $0.22 g_0$ . A broad minimum around the Fermi energy,  $E_F \approx -5.1 \text{ eV}$ , is observed. The broad peak in

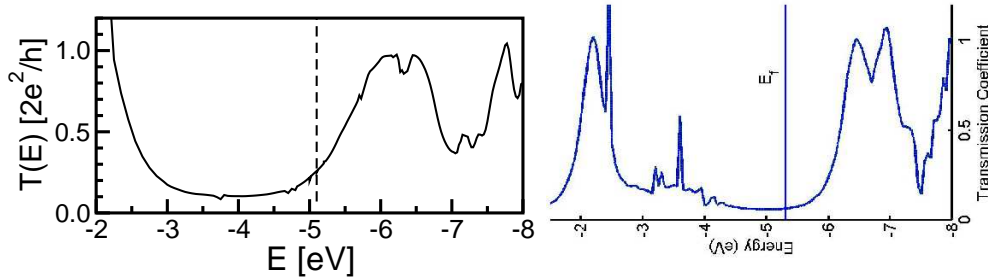


Figure 6.2: Transmission of benzene-1,4-di-thiol. Left: our data, for the transmission in units of  $g_0 = 2\frac{e^2}{h}$  over energy. Right: For comparison of different theoretical calculations, data by Xue and Ratner is depicted [136]. The Fermi energy ( $\approx -5.1$  eV) is depicted as a vertical line in both calculations.

the transmission at about  $-6$  eV is caused by the highest occupied molecular orbitals, broadened by the hybridization with the d-band of the gold contacts.

On the theory side, results for the conductance of benzene-1,4-di-thiol, obtained from DFT based calculations, have recently converged: with increasing level of sophistication in the implementation of the DFT based calculations, the conductance increased, converging to values equivalent to those obtained by us [134, 136]. To illustrate this, we depict the data by Xue *et al.* in the right hand side plot of fig. 6.2. The shape of the curve as well as the absolute value are in excellent agreement with our results.

## Experimental data

In general, experimental measurements of benzene turn out to be very challenging due to the small size of the molecule. The method of choice to conduct the measurements of such a small molecule is the mechanically controlled break-junction technique, as it offers the best control of the electrode distance allowing for the measurement of molecules of very small dimension.

But still, reproducible data are extremely difficult to obtain. Often, empty break-junctions, or contaminated junctions (presence of  $H_2$ ,  $H_2O$ ,  $O_2$  or parallel conductance through rough gold surface) are measured. Since it is one of the most popular molecules to be studied theoretically, we present data here. However, one should keep in mind that the reliability of experimental data of larger molecules is much higher. For this reason, we will also discuss the comparison between experiment and theory for the larger, symmetric, anthracene-based molecule of fig. 6.6, which was measured at our institute [11], in the next section.

We will present in this section the experimental data of the first experiment, done by M. Reed *et al.* [5], see fig. 6.3, as well as the data obtained recently in our institute by M. Di Leo [129], fig. 6.4. We consider the more recent data of fig. 6.4 to be more reliable due to improvements in the experimental technique, e.g. in the distance control and sample preparation. The early experiment has also been criticized for the large voltage window (up to 4.5 V) in which the I–V was recorded, whereas in more recent experiments, very rarely stable I–Vs are observed for bias voltages of more than 1.5 V in break–junction experiments [139].

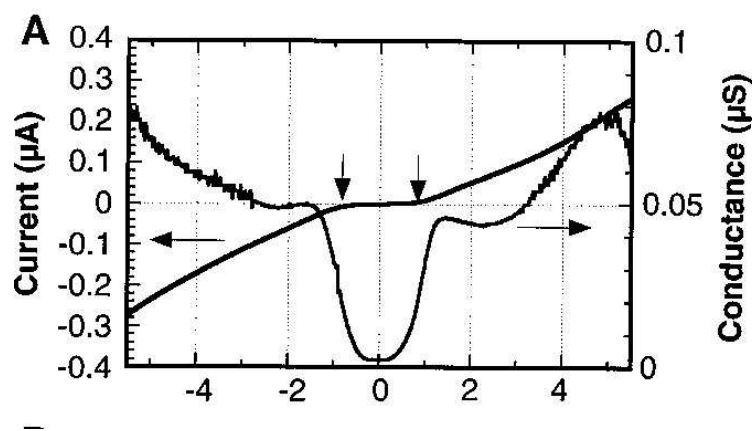


Figure 6.3: *I–V* characteristics of benzene-1,4-di-thiol. Measurement by M. Reed [5]. Shown are current over applied bias voltage in  $\mu\text{A}$  and the differential conductance,  $\frac{dI}{dV}$  in  $\mu\text{S}$ .

Figure 6.3 shows the conductance measurement by Reed [5]. The measurements for benzene-1,4-di-thiol by M. Di Leo [129] at our institute are presented in fig. 6.4.

Both curves show a pronounced conductance gap at low bias, and first peaks in the differential conductance at symmetric bias voltages, when the first molecular level, most likely the highest occupied molecular orbital (HOMO), comes into the bias voltage window. This gap is due to Coulomb blockade. The zero bias conductance in Reeds experiment is of the order of  $10^{-5}g_0$  and even lower in the experiment by Di Leo,  $\approx 0.3 \text{ nS} = 4 \cdot 10^{-6}g_0$ .

In the position of the peaks, the experiments differ significantly. Whereas Reeds data exhibits a peak in the differential conductance at 1.75 V, the measurements by Di Leo put the peak at about 0.75 V. Di Leo obtained measurements for several samples, resulting in peak positions between 0.6 and 1.0 V. The gap width for low bias voltages is similar in both experiments, about 0.75 V.

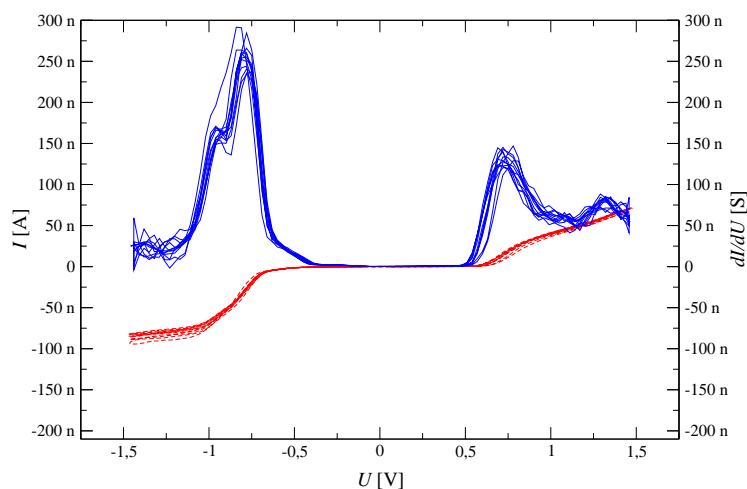


Figure 6.4:  $I$ - $V$  characteristics of benzene-1,4-di-thiol. Red: Current in  $nA$  over applied bias voltage. Blue: differential conductance  $dI/dV$  measured in  $nS$ . Different traces correspond to different voltage sweeps. Measurements by M. Di Leo, INT [129].

The asymmetry, pronounced to a different extent in the two experiments, has to be attributed to asymmetric coupling to the gold due to the contact microscopies.

### Comparison with theory

In fig. 6.5, the differential conductance is plotted rather than the transmission for better comparison with experimental data. It has been obtained using formula 3.10 ignoring polarization corrections that may exist.

The theoretical data exhibits a broad minimum near zero bias, but neither its width nor the zero-bias conductance itself bear any resemblance to the experimental results presented above. Neither do the theoretical calculations exhibit a conductance gap for low bias nor do the peak positions match the experimental data.

In all, conductance values are overestimated by several orders of magnitude: whereas the calculated zero-bias conductance is about  $0.22 g_0$ , the experimental values are  $10^{-5} g_0$  or even lower. Thus we must conclude that not even qualitative agreement is reached in the case of benzene-di-thiol.

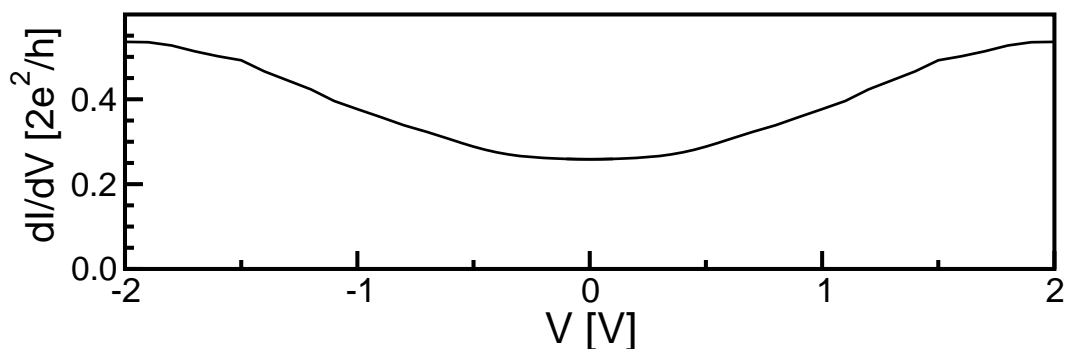


Figure 6.5: Differential conductance of benzene-1,4-di-thiol. Theoretical calculations. Pyramids of 55 gold atoms each were included in the extended molecule for the DFT calculations (see fig. 6.1).

This large quantitative discrepancy of several orders of magnitude is inherent to all other numerical calculations based on DFT as well [66, 68, 72, 73, 133, 134, 136, 138]. Various explanations for this drastic discrepancy have been brought up and will be discussed in section 6.3 as well as in chapter 7.

## 6.2 Symmetric, anthracene-based molecule

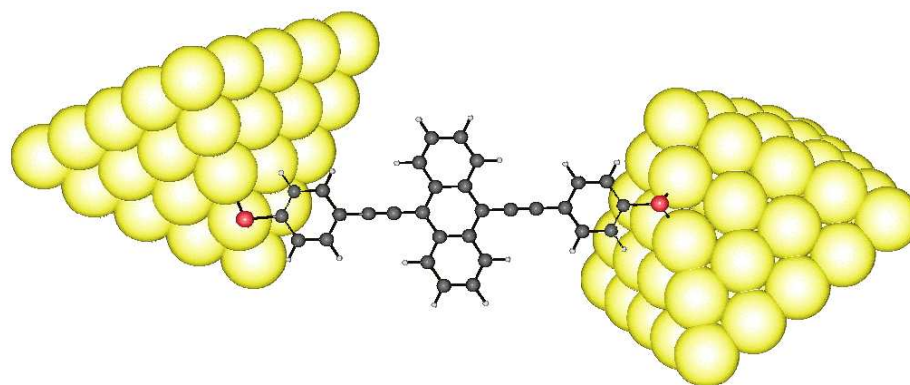


Figure 6.6: Schematic representation for the extended molecule for the conductance calculation of the symmetric molecule, 9,10-Bis((2'-para-mercaptophenyl)-ethynyl)-anthracene. In the calculation we considered pyramids of 55 gold atoms each for the contact.

For the symmetric, anthracene-based molecule of fig. 6.6, experimental data for many samples was obtained by Reichert *et al.* at our institute [11]. The molecule, 9,10-di(2'-para-acetylmercaptophenyl)-ethynyl)-anthracene, has an extended  $\pi$ -system, formed by the central anthracene (3 benzene rings). The two separate outer benzene rings of the molecule are connected to the conjugated part by acetylene bridges, which ensures that the  $\pi$ -system finally extends over the whole molecule and at the same time they render it very stiff and rod-like to ensure a reliable formation of molecular junctions. Contacting to the gold is done via sulfur end-groups. The molecule has a length of about 2 nm

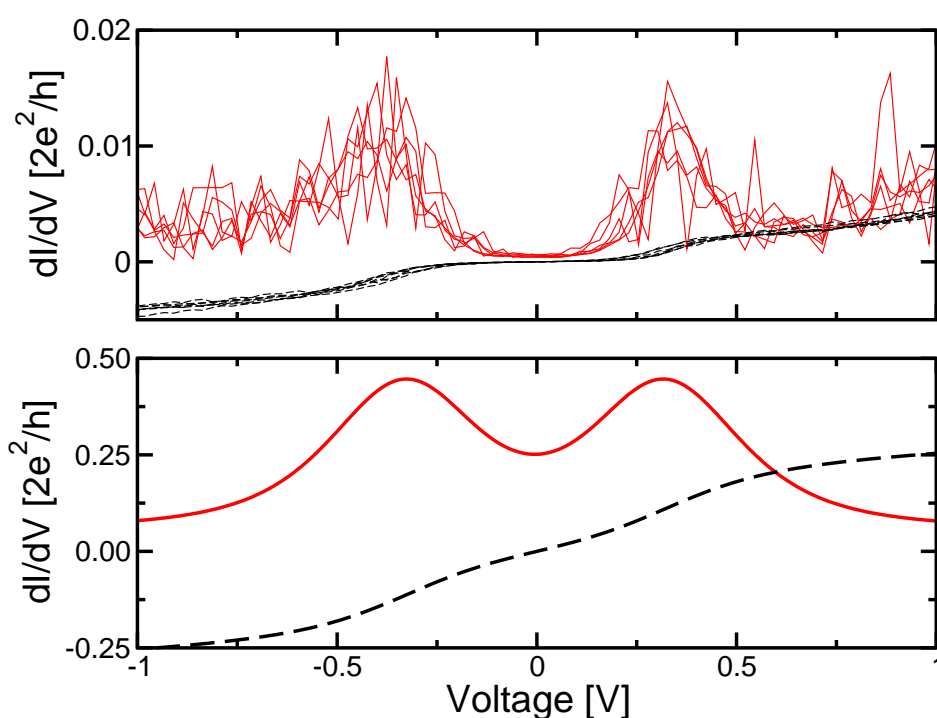


Figure 6.7:  $I$ - $V$  characteristics of the symmetric molecule from fig. 6.6. Upper graph: experimental data by Reichert *et al.* [11]. Dashed, black:  $I$ - $V$  characteristics; solid, red: differential conductance. Different lines correspond to different voltage sweeps. Lower graph: Theoretical calculation, the structure was relaxed completely in the DFT calculation. Dashed, black:  $I$ - $V$  characteristics; solid, red: differential conductance.

Fig. 6.7 depicts the experimental data for the conductance as well as the results of our theoretical calculations. Qualitatively they agree. Both show a pronounced peak in the differential conductance at about 0.3 V. This time, in contrast to the benzene data above, the position in energy and the broadening of the theoretical peaks is in agreement with the experimental one.

Again, in the experiment we observe a gap in the measured conductance at low bias. Only for bias voltages above  $0.2\text{ V}$  the current increases significantly. In our numerical calculation, the gap is indicated but not fully developed in the sense that the zero-bias conductance is about  $0.5 g_0$ , only a factor of two lower than the maximum values at  $0.3\text{ V}$ , though. Quantitatively the same discrepancy as in the case of benzene is present: the measured differential conductance at the peak position  $0.3\text{ V}$ , is about  $2 \cdot 10^{-2} g_0$  which is two to three orders of magnitude smaller than the theoretical prediction,  $0.8 g_0$ .

The numerical results exhibit a far too metallic behavior. This enormous quantitative discrepancy of several orders of magnitude between experiment and theory is observed for all results obtained from properly performed DFT calculations. Therefore an analysis and an understanding of the possible underlying reasons is of utmost importance. In the following sections we will discuss several sources.

## 6.3 Influence of stress on the conductance

The most often cited possible reason for this large quantitative, and in the case of benzene even qualitative, discrepancy between theory and experiment is, that the actual microscopic details of the molecular contact are unknown and the conductance could change strongly with modifications in the microscopies of the coupling of the molecule to the leads, see e.g., [72, 73, 134, 136].

As this large discrepancy is encountered in all molecules, we chose for simplicity to use the benzene-1,4-di-thiol molecule again to study the influence of the precise microscopies on the conductance.

The benzene molecule is, as in most experiments, coupled to the gold electrodes via terminal sulfur atoms that form a stable covalent bond with the gold of the electrodes. In a break-junction experiment, the molecular structure and the microscopies of the coupling to the gold most likely is not completely relaxed, as the boundary conditions in form of the electrode spacing pose hard restrictions on the geometry.

On the other hand, gold is a very ductile material. Experimental data by Rubio-Bollinger *et al.* [122, 140] suggests, that the stiffness of the first atom layers of nanosized gold contacts is only about  $6 \frac{\text{N}}{\text{m}}$  and the corresponding force for breaking the sulfur-gold bond should be much larger.

Usually, in break-junction experiments of single molecules, not the bond between sulfur and gold breaks when the electrode distance is enlarged, but one or several gold atoms are pulled out of the contact during the opening. This

results in stable I–V curves over a variable distance. Then the breaking of the contact occurs, when this “gold chain” breaks.

The breaking force of a chain of gold atoms has been estimated experimentally to be about 1 nN [140], which is in full agreement with molecular dynamics and Density Functional Theory calculations [141, 142] that predict  $1.2nN$ . There, pulling on the molecule resulted in the formation of a monoatomic gold wire followed by rupture of a gold-gold bond within the wire. This poses strong limits on the actual geometrical stress the molecule will be exerted to in a break-junction.

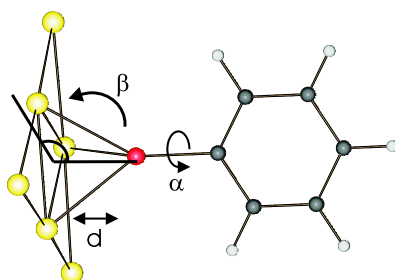


Figure 6.8: Different geometric degrees of freedom for the bonding of a benzene molecule on a gold surface. Red: sulfur, yellow: gold, black: carbon, grey: hydrogen.  $d$ : distance of the sulfur–gold bond.  $\alpha$ : angle of rotation about the molecular axis.  $\beta$ : tilting angle between molecular axis and gold surface.

To investigate the influence of this stress on the conductance, we did a study of the influence of a change in geometric parameters on the conductance properties for the paradigmatic molecule benzene-1,4-di-thiol. Fig. 6.8 depicts the different degrees of freedom in the bonding between the benzene molecule and the gold electrode.

### 6.3.1 Sulfur–gold bond distance $d$

We calculated the transmission of benzene-1,4-di-thiol where the sulfur–gold bond distance was increased by 5 and 10 pm (cf. distance of Au–atoms in bulk gold: 240 pm) in relation to its equilibrium value. The comparison with the relaxed equilibrium distance situation is presented in fig. 6.9.

For both elongations, the transmission is only changed slightly. Maximum differences amount to about 10 per cent of the conductance. Around the Fermi energy ( $E_F \approx -5.1 eV$ ) the change in the calculated zero bias conductance is almost invisible.

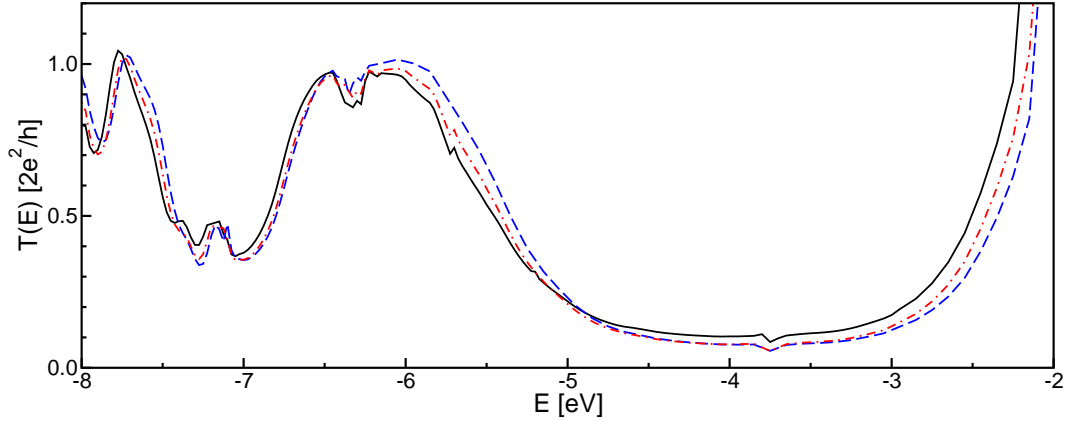


Figure 6.9: Influence of the sulfur–gold bond distance,  $d$  (see fig. 6.8), on the conductance of benzene-1,4-di-thiol. Solid, black line: transmission for the relaxed equilibrium distance. Red, dot–dashed line: sulfur–gold distance increased by 5 pm. Blue, dotted line: sulfur–gold distance increased by 10 pm.

Larger deviations from the equilibrium bond distance are unlikely to occur in experiment as the gold structure would more likely deform in reaction to the applied forces than the sulfur–gold bond distance would increase further [141, 142]. Krüger *et al* [141] observed changes of up to 10 pm in their MD simulations for the  $S - Au_1$  bond during elongation and chain formation.

### 6.3.2 Tilting the molecule: angle $\beta$ between molecule and gold

A larger effect can be observed, when the molecule is tilted by changing the angle  $\beta$  between the gold surface and the molecular axis (fig. 6.8). Results for tilting the molecule by 15, and 25 degrees are displayed in fig. 6.10. Here, deviations from the equilibrium geometry conductance for a tilt of 15 degrees amount to less than 30 %. Again, close to the Fermi energy the difference is small. ( $\leq 0.1 \frac{2e^2}{h}$ ).

Even for an unphysically strong deviation from the relaxed structure by an angle of 25 degrees, the change in the zero bias conductance is of the same order of magnitude. Here, for energies different from the Fermi energy the influence is larger, but deviations stay well below a factor of two in conductance.

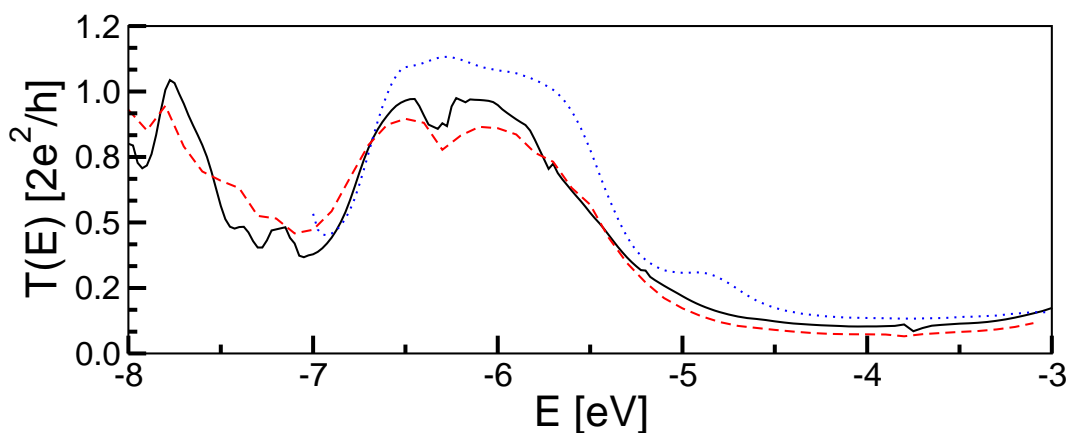


Figure 6.10: Influence of the tilting angle,  $\beta$ , between molecular axis and contact (see fig. 6.8) on the conductance of benzene-1,4-di-thiol. Solid, black line: transmission for the relaxed equilibrium distance. Red, dashed line: tilting angle changed by 15 degrees. Blue, dotted line: angle changed by 25 degrees.

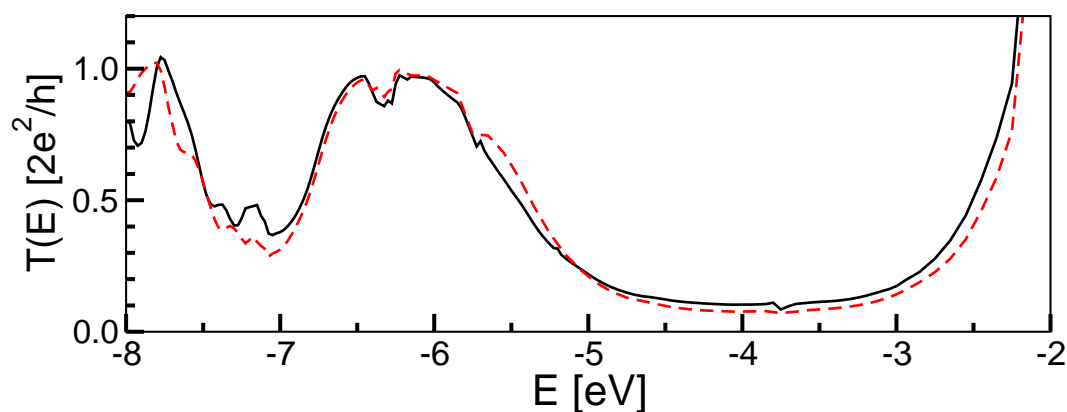


Figure 6.11: Influence of a rotation about the symmetry axis of the molecule by the angle  $\alpha$  (see fig. 6.8) on the conductance of benzene-1,4-di-thiol. Solid, black line: transmission for the relaxed equilibrium distance. Red, dashed line: transmission after a change in  $\alpha$  of  $\pi/24$ .

### 6.3.3 Rotating the molecule: angle $\alpha$

When the molecule is rotated around the axis defined by the two sulfur atoms (see fig. 6.8) only very small changes in the conductance are observed. Fig. 6.11 shows the influence of a rotation of  $\alpha = \pi/24$ . The zero bias conductance, at  $E = E_F \approx -5.1$  eV, for the rotated molecule is identical with the conductance of the relaxed structure.

### 6.3.4 Strong distortion of the coupling geometry

As a final test, we performed a calculation for a situation where the microscopics of the coupling to the leads is strongly distorted. In an actual experiment, we expect that a situation like this is energetically too unfavorable to be realized but it gives us an upper bound for the influence of the coupling geometry on the conductance properties.

Especially as the first layers of the gold electrodes are extremely ductile the gold will yield to this high stress resulting in a situation closer to the relaxed structure. In fig. 6.12 we present the conductance for a situation where the

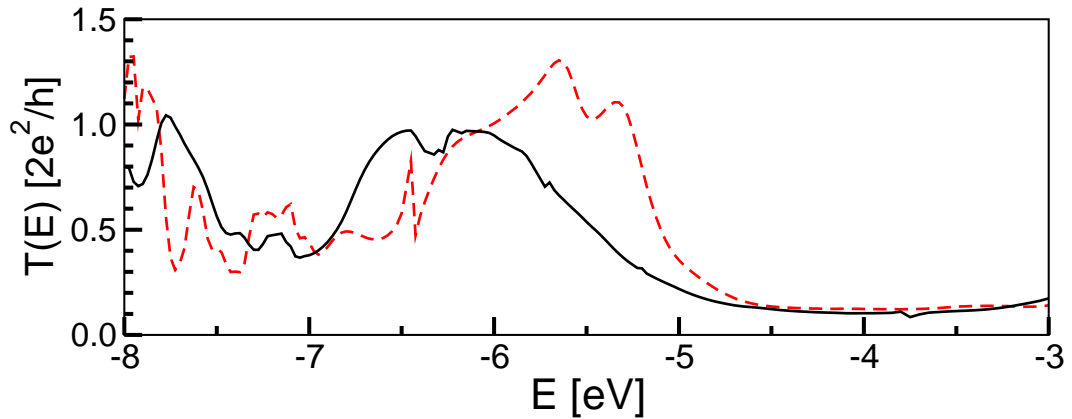


Figure 6.12: Influence of a strong distortion in the coupling geometry on the conductance of benzene-1,4-di-thiol. Tilt angle  $\beta$  of 30 degrees. Rotation about angle  $\alpha$  of 25 degrees. Solid, black line: transmission for the relaxed equilibrium distance. Red, dashed line: transmission of the distorted situation. Fermi energy,  $E_F \approx -5.1$  eV.

molecule is rotated by an angle  $\alpha$  of about 25 degrees and at the same time tilted by an angle  $\beta$  of about 30 degrees.

Still, the zero bias conductance is of the same order of magnitude. The deviation at the Fermi energy,  $E_F \approx -5.1$  eV, is less than a factor of two. For energies below  $E_F$ , the structure of the curve is changed significantly.

Instead of reducing the conductance, we can observe that the stress leads to an increase of the conductance. This can be attributed to the decreased distance of the extended  $\pi$ -system of the benzene ring to the gold surface coupling better to the conduction band states of the gold due to the decrease in the gold-ring distance, caused by the tilt.

### 6.3.5 Summary

All variations of the geometric parameters of the coupling between the molecule and the gold surface within reasonable limits did not cause a significant change of the conductance properties. Changes stay well below an order of magnitude and therefore cannot account for the large quantitative discrepancy between theory and experiment.

We can summarize, that the unknown microscopic conditions are not likely to be the only reason for the high conductance values in all present DFT-based transport calculations.

On the other hand, the magnitude of the variations in conductance observed in experiments between consecutive voltage sweeps after opening and reclosing the break-junction amount to a factor of two or three [139]. Changes due to small variations of the geometry observed in our calculations are of the same order of magnitude.

A remaining question is the influence of the type of coupling between sulfur and gold on the conductance, and whether this can be enough to account for the discrepancy between theory and experiment. This will be the subject of the next section.

## 6.4 Influence of the sulfur—gold coupling: coupling to 1, 2 and 3 Au atoms

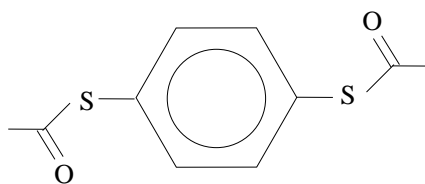


Figure 6.13: Benzene-di-thiol. Benzene molecule plus the thio-acetyl protection groups (sulphur and acetyl group) that prevent the molecules from forming chains. At the gold surface the acetyl protection group is removed and a stable, covalent bond of the sulfur atom with the gold is formed.

Most molecules currently used in single molecule experiments are contacted to the gold electrodes via terminal *acetyl-protected mono-thiols*. The end-groups, consisting of a sulfur atom and an *acetyl* protection group ensure the proper and defined bonding to the gold surface [130]. Figure 6.13 depicts these thio-acetyl-groups in the example of benzene-di-thiol. The protection

group prevents the formation of chains of the investigated molecules. Only at the gold surface, the acetyl group deprotects and a stable, covalent gold—sulphur bond is formed. The acetyl protection group also slows down the immobilization kinetics [130]. This reduces the density of molecules on the gold surface, leading to a reduced tendency of aggregation to larger bulks, thus increasing the probability of really contacting single molecules. The detailed mechanism of the deprotection process is currently unknown [130], but water may be the mediating factor [130]. But numerous experiments made it a well established, and controlled working procedure.

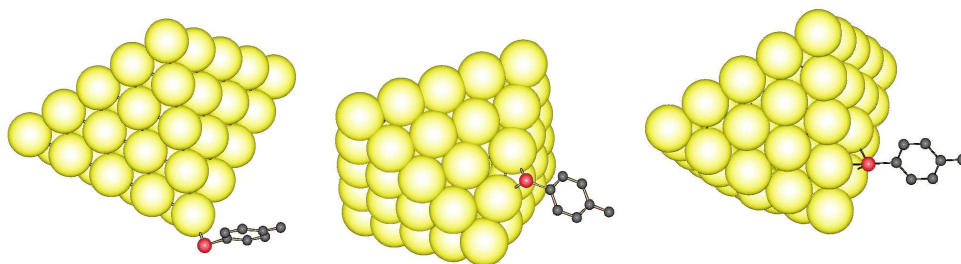


Figure 6.14: Different possible realizations of the coupling of sulphur (red) to gold surfaces. Left: sulphur binds to one gold atom (*on-top position*). Center: sulphur binds to two gold atoms. Right: sulphur binds to three gold atoms (*hollow position*).

The sulfur—gold bond can occur in three different stable abundances [143], which are depicted in fig. 6.14

- *on-top position*: the sulphur binds to one gold atom, the bond distance, obtained from a DFT calculation with structure relaxation, is about 2.34 Å.
- $S - Au_2$ : the sulphur binds to two gold atoms, the bond distance is slightly larger, at about 2.47 Å.
- *hollow position*: the sulphur binds to three gold atoms with the bond distance taking a value of 2.56 Å.

It is known that on plane Au(111) surfaces sulfur tends to bind to three gold atoms, i.e., the *hollow position* is the most stable one [143, 144]. Binding to just one gold atom — the on top position — corresponds to a local minimum of the free energy and binding to two gold atoms is unstable.

On rough surfaces exhibiting edges the situation can be completely different. We performed density functional theory calculations for the three different binding possibilities. Our results show, that near an edge, the sulfur

finds its most stable position by binding to two gold atoms, as depicted in fig. 6.14,(center). The *on top* position, shown in fig. 6.14,(left), where the sulfur binds to only one gold atom at the tip of the contact pyramid remains a minimum as in the plane Au(111) case, but now at a  $0.7\text{ eV}$  higher energy. The *hollow position*, displayed in fig. 6.14,(right), being the most stable one on a plane Au(111) surface, turns unstable, when the contact is formed on an edge.

In break-junction experiments the contact surface where the sulfur binds to form the molecular bridge is most likely irregular due to the mechanical breaking of the constriction to create the contact, see §2.2 and §6.1. Thus it is not possible to predict, which of the possible bindings is realized in the actual experimental situation. As one might suspect that the conduction properties are influenced by the type of bond it is worthwhile to consider all three cases in the conductance calculations.

It might also be possible, that during the experiment the structure somewhat changes so that a switching process between different coupling realizations occurs. This effect could then lead to *inhomogeneous broadening* of the peaks in the differential conductance, i.e. a broadening due to the different conductance behavior of different microscopic conditions.

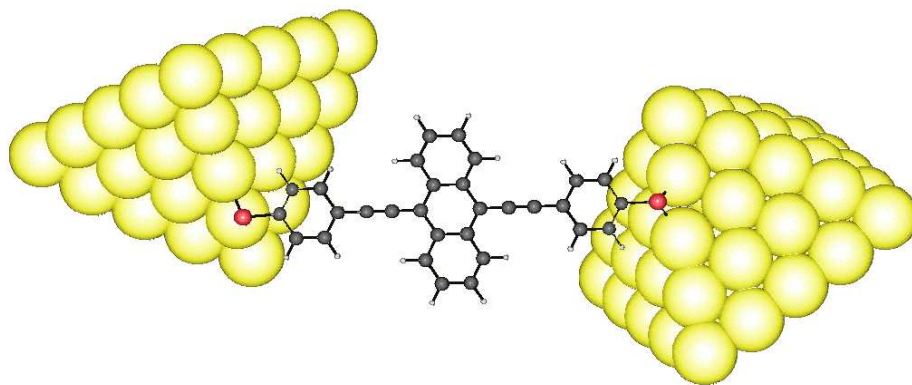


*Figure 6.15: Schematic representation for a conductance measurement of the symmetric molecule, (9,10-Bis((2'-para-mercaptophenyl)-ethynyl)-anthracene) used to study the influence of the sulfur-gold coupling on the conductance. In the calculation we considered pyramids of 55 gold atoms each for the contact.*

For the symmetric, anthracene-based organic molecule depicted in figure 6.15, which has been measured experimentally at our institute [11] (see §6.2 above for further discussion of the experimental data and comparison with the corresponding calculations), we did perform conductance calculations for all three possible binding variants.

Results for the conductance calculation, where we again considered pyramids of 55 gold atoms each to construct the *extended molecule* for the DFT calculation, are presented in fig 6.16. The structure of the molecule was allowed to relax in the DFT runs. The three different traces correspond to the cases in which the sulfur binds to either one, two or three gold atoms.

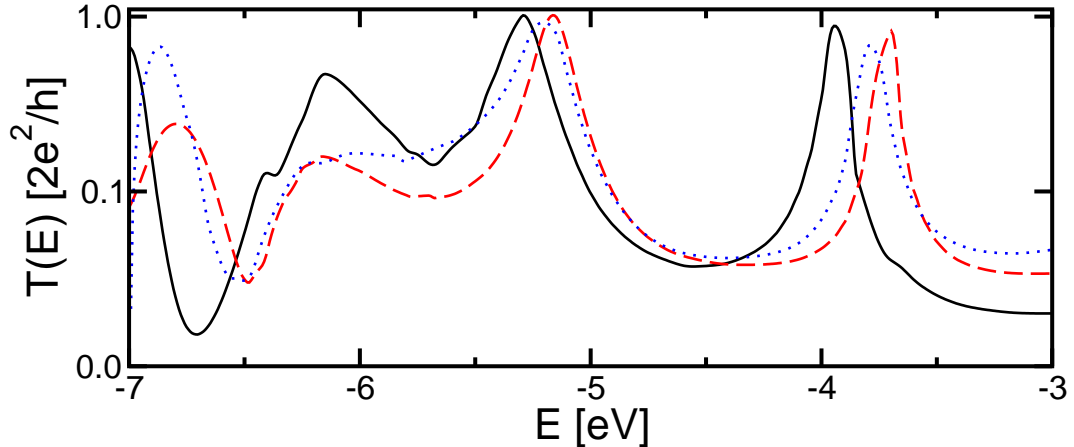


Figure 6.16: Influence of the type of coupling between sulphur and gold on the conductance of the symmetric molecule depicted in fig. 6.15. Displayed is the conductance for the three possible bonding variations depicted in fig. 6.14: *S* coupled to one gold atom in the on-top position (black, solid line), *S* coupled to two gold atoms (red, dashed line), and *S* coupled to three gold atoms in the hollow position (blue, dotted line). The Fermi energy is  $\approx -5.1$  eV.

Qualitatively the three curves are in good agreement with experimental findings [11], see discussion in §6.2 above.

The experimental data (see fig. 6.7 above) shows a conductance gap for low bias voltages and the differential conductance exhibits for the different measurements a maximum with a position between 0.3 V and 0.5 V, that would correspond to a resonant molecular level at about 0.15 eV to 0.3 eV below the Fermi energy ( $E_F \approx -5.1$  eV) in the case of symmetric couplings to the leads. The different positions could be due to inhomogeneous broadening effects, which is supported by our theoretical findings:

The qualitative effect of the microscopic change in contact geometry on the transmission is small. The position of the valence peak close to  $-5.2$  eV varies by up to 0.2 eV, depending on the bond type. The overall shape of the transmission curve remains unchanged.

Shifts of the peak position of 0.2 eV would, in the case of symmetric coupling to the leads, correspond to a shift of the  $dI/dV$  peak in the experiment by

about  $0.4 V$  which is comparable to the observed experimental variations of  $0.3 V$ . Since, near the Fermi energy, the transmission has a large slope in our calculations, the zero bias conductance can depend on the type of binding in a sensitive way. Depending on the type of coupling, the zero bias value can vary by a factor of four. But again, the transmission remains on the same order of magnitude, ruling out the bond type as a source of the overestimated theoretical conductance. On the other hand the changes due to bonding type can be an explanation for the different zero-bias conductance values obtained from consecutive measurements after opening and reclosing the molecular break junction contact. Typically these vary by a factor of 2–3 [139], which is in good agreement with our theoretical findings for the variations due to different couplings.

## 6.5 Conclusions

To summarize our findings of this chapter, we have shown that theoretical transport calculations based on DFT have converged to one result. In the case of benzene, DFT based calculations do not even qualitatively agree with measurements. On the other hand, for the larger symmetric, anthracene-based molecule, qualitative agreement with experimental data is good, whereas quantitative discrepancy remain high. In general DFT based calculations overestimate the conductance of organic molecules by several orders of magnitude.

We have shown that neither variations in the microscopic geometry of the coupling to the electrodes nor differences in the bond type between gold and sulfur do have a large influence on the conductance. Therefore, deviations from the geometry assumed in Fig. 6.6 in the actual experiment do not offer a plausible explanation for quantitative discrepancy of several orders of magnitude between experiment and DFT based transport calculations.

In principle, it is conceivable that virtually all experiments on the conductance of organic molecules are affected by dirt, e.g., oxygen chemically bound to the surface of the electrodes close to the contact region, that could reduce the conductance substantially. While this is a logical possibility, the sum of experimental evidence is not in favor of this interpretation, see also chapter 10.

Therefore, we will have to resort to more fundamental considerations to resolve this open question. In the next chapter we will present our considerations on the applicability of ground-state DFT to transport in molecular structures in general and will argue, in which cases and for what reasons it can fail.

# Chapter 7

## Exact description of transport within TD–DFT and Landauer–Büttiker theory for interacting electrons

In this chapter, we will present how it is possible to obtain in principle exact results for the conductance of mesoscopic systems in non–equilibrium using time–dependent Density Functional Theory and the appropriate non–equilibrium exchange–correlation functional. But first, we will discuss shortly, how different approximations made for the single particle Greens–function, i.e., LDA, Hartree Fock, or GGA influence the calculated conductance.

### 7.1 Transport properties in LDA and Hartree Fock

Before presenting our results on how to obtain in principle exact results using time–dependent DFT, it is instructive to compare results for the transmission curves based on different approximate single–particle theories.

One might perhaps suspect that, with increasing sophistication in the functional, the quantitative discrepancy between experiment and theory decreases. Comparing Hartree–Fock calculations with DFT based calculations, we will gain some insight into how large the self–interaction corrections as well as the contributions from correlation are. Again using the paradigmatic system

benzene-1,4-di-thiol, we have conducted electronic structure calculations considering several different levels of correlation. We used the following methods:

- **extended Hückel:**

Extended Hückel calculations are tight binding calculations that only include the hopping to the next neighboring atom sites in the Hamiltonian, when calculating the electronic structure. The calculation is not self-consistent. The coupling constants are taken from a database, obtained from DFT calculations.

- **Equilibrium DFT; GGA (BP86) functional:**

For comparison, we added the data from the full DFT calculation as described above in §6.1. From the DFT calculation we gain information on the diagonal elements of the Greens-function as  $\int dE -\frac{1}{\pi} \text{Im} G(\mathbf{r}, \mathbf{r}, E) = n$ . For the off-diagonal elements — important for transport — we, strictly speaking, don't know the physical meaning in the general case.

- **Hartree-Fock:**

By using a Hartree-Fock calculation, we avoid the errors from the unphysical *self-interaction*, present in DFT functionals. But at the same time, correlation effects are not described. Hartree-Fock gives the best single slater determinant approximation for the electronic ground state. It is the best estimate for the full Greens-function, including the off-diagonal matrix elements.

Our results are depicted in fig. 7.1. To facilitate the comparison to Hartree-Fock data, all calculations were performed with gold pyramids of 14 atoms each in the extended molecule as parts of the contacts to account for the coupling to the leads. This reduced number of gold atoms was necessary as Hartree-Fock calculations become numerically too costly for larger systems. In order to estimate the influence of this restriction on the DFT results, the data for pyramids of 55 atoms each is included as well.

The results from the DFT calculation, performed as described in the sections above (pyramids of 55 gold atoms as contacts, ...) are shown as a solid line. The DFT calculation with pyramids of 14 gold atoms is depicted in blue (dot-dashed). Compared to the other methods, DFT gives by far the highest conductance.

For the simplest of the three approximations, the extended Hückel calculation, we obtain the lowest conductance. At the Fermi energy, conductance is about 3 orders of magnitude smaller.

The description closest to experiments seems to be given on the basis of Hartree-Fock, depicted as a dotted curve. Absolute conductance levels are

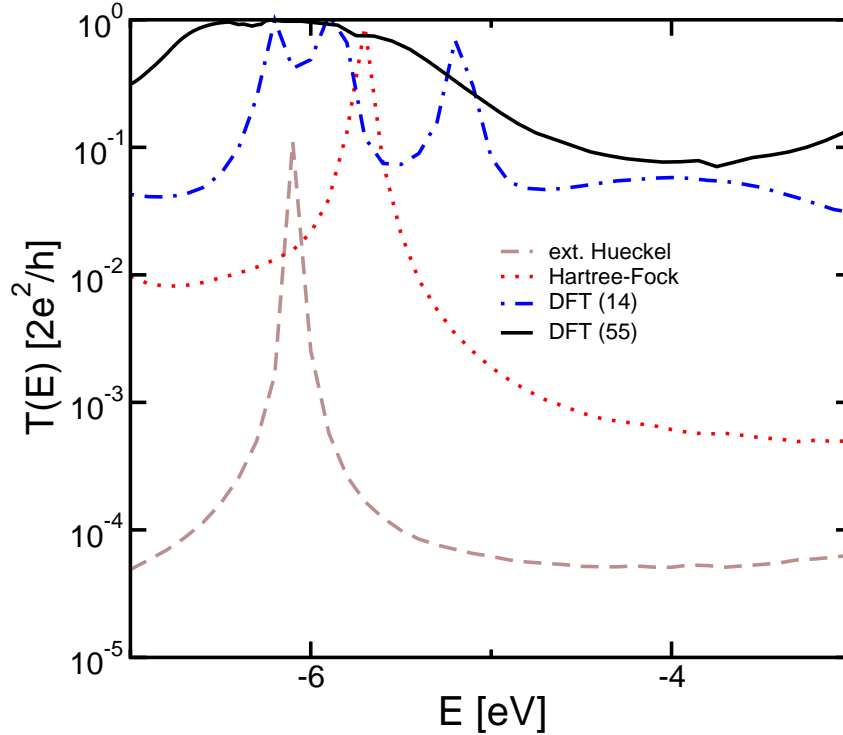


Figure 7.1: Benzene-di-thiol. Influence of the level of correlation in the electronic structure calculation on the conductance. Displayed are our results for the transmission obtained from Hartree-Fock (dashed, red), extended Hückel (dotted, brown) and DFT (dot-dashed, blue) calculations for the central cluster. Pyramids of 14 gold atoms per side were added for the calculation of the extended molecule. For comparison, we did also plot the calculation with pyramids of 55 gold atoms (solid, black) as described in §6.1.

much closer to the experimental results (see §6.1) which is ascribed to the level broadening being much weaker than in DFT.

This can be understood in two ways:

a) by looking at the Greens-function of the system. As described above, Hartree-Fock is the best effective single particle estimate for the elements of the Greens-function, including the nondiagonal ones, which are needed to describe the transport properties. On the other hand, in DFT only the diagonal matrix elements have a physical meaning by their connection to the electron density, given exactly by DFT. The physical meaning of the nondiagonal elements of the Greens-function obtained from DFT is not known. We know, that Hartree-Fock gives more localized states than DFT, where the systems tend to be more metallic. This results in a higher conductance in the DFT case.

b) by studying the errors made by using equilibrium DFT. The real many-body wave-function of the system is no single Slater determinant, but in the present DFT calculations we effectively assume it to be a Slater determinant of Kohn-Sham states. The best estimate for the ground-state (including its spatial properties) based on a single Slater-determinant is given by Hartree-Fock. By using DFT and assuming a single Slater determinant, we, in a sense, mix the real ground-state with excited states, which most likely are less localized. This results in an overestimation of the broadening.

Curves from different DFT functionals, like PBE or PW91 (see §4.7) instead of the used Becke Purdue functional (BP86), which we do not plot here, do not change the result in a significant way.

Hartree-Fock conductance values are closer to experiment than DFT based calculations, but on the other hand, recall that in Hartree-Fock, correlation physics is missing. This can result in a significant shift of the resonances compared to their experimental values.

## Conclusion

Deficiencies inherent to current DFT functionals, e.g., the self-interaction problem, are one of the reasons for the strong overestimation of the peak broadening. As a consequence, With the Fermi energy close to the HOMO and LUMO of the calculated molecules, DFT predicts conductances of too metallic character. The position of the peaks may, on the other hand, be correct. Hartree-Fock treats self-interaction correctly (see §4.7.3), so the level broadening is less overestimated but this is at the cost of wrong peak positions (as correlation physics is missing in Hartree-Fock).

As Hartree-Fock is numerically very expensive for larger systems, DFT remains the only choice for transport calculations of large systems right now. We will thus have to look at ways to circumvent the problems inherent to the present-state DFT based calculations. This will be the topic of the next sections.

## 7.2 Exact transport formalism using TD-DFT<sup>1</sup>

Currently, ground-state density functional theory in combination with the Landauer-Büttiker formalism is the most widely used approach to numerical transport calculations for single molecule junctions [66–68, 72, 73, 132–137].

Despite this enormous effort, a quantitative description of transport for weakly coupled molecules with a conductance well below the conductance quantum  $g_0$  has not been achieved, yet, as we have seen in chapter 6. Indeed, experimental and theoretical values for the zero bias conductance of organic molecules differ by one to (more commonly) three orders of magnitude [11, 72, 138, 145, 146].

We have seen in chapter 6, that there are large quantitative, and, in the case of benzene even qualitative, problems in the description of transport by ground-state DFT in the scattering approach. Most likely, geometric changes alone can not explain the discrepancy between theory and experiment, we believe the problems are also conceptual.

In the chapter on DFT, chap. 4, we learned that ground-state Density Functional Theory does in principle give us the exact density, but not necessarily the wavefunction or transport characteristics. The ground-state DFT based scattering approach is motivated by the tremendous success of DFT in many systems: even though DFT in the LDA or GGA approximation in principle does not need to, it gives, e.g., good results for the ground-state electron density and bond geometry of many molecular systems even though these systems are far away from the uniform electron gas.

In the following, we will present how we can obtain in principle exact results for the current from time-dependent Density Functional Theory (TD-DFT).

Time-dependent DFT, by construction, gives us the exact time-dependent density,  $n(\mathbf{x}, t)$ , of an interacting many-particle system, provided, the exact exchange-correlation functional is known. From the density, it is easy to obtain the time-dependent longitudinal current,  $j(\mathbf{x}, t)$ , via the continuity equation

$$\frac{\partial j(\mathbf{x}, t)}{\partial t} + \text{div } j = 0. \quad (7.1)$$

This is a very powerful idea, since TD-DFT is valid for arbitrary strength of the external applied potential and is in principle exact, if we know the appropriate exchange-correlation functional. In addition, it is possible to include electron-

---

<sup>1</sup>The results in this subsection have been obtained in collaboration with K. Burke, Rutgers, NJ.

lattice interaction in this picture, a formalism is currently being developed, see [147].

As the full non–equilibrium exchange–correlation functional is a very complicated object, we will focus in the following on the linear response regime. This will make an analysis of the differences to equilibrium DFT easier.

The conductivity  $\sigma_{kl}$  of the time–dependent system in linear response is defined via

$$j_k(\mathbf{x}, \omega) = \int d\mathbf{x}' \sigma(\mathbf{x}, \mathbf{x}', \omega)_{kl} E(\mathbf{x}', \omega)_l \quad (7.2)$$

with the local electric field,  $\mathbf{E}(\mathbf{x}, \omega)$  given by

$$\mathbf{E}(\mathbf{x}, \omega) = \mathbf{E}_{\text{ind}}(\mathbf{x}, \omega) + \mathbf{E}_{\text{ext}}(\mathbf{x}, \omega). \quad (7.3)$$

It has two contributions, the externally applied electric field,  $\mathbf{E}_{\text{ext}}(\mathbf{x}, \omega)$  and the induced field,  $\mathbf{E}_{\text{ind}}(\mathbf{x}, \omega)$ .

We can relate this now to the Kohn–Sham formalism: there, the effective single–particle potential,  $v_{\text{eff}}$ , is given by

$$v_{\text{eff}} = v_{\text{ext}} + v_H + v_{xc} \quad (7.4)$$

with the external potential,  $v_{\text{ext}}$ , the Hartree term,  $v_H$ , and the remaining part incorporated in the exchange–correlation potential,  $v_{xc}$ .

Thus, we can now define a Kohn–Sham conductivity,  $\sigma_{kl}^{KS}$ , via

$$j_k(\mathbf{x}, \omega) = \int d\mathbf{x}' \sigma^{KS}(\mathbf{x}, \mathbf{x}', \omega)_{kl} (E_{\text{ext},l}(\mathbf{x}', \omega) + E_H(\mathbf{x}', \omega) + E_{xc,l}(\mathbf{x}', \omega)) \quad (7.5)$$

The effective electric field within the Kohn–Sham picture thereby consists of the external contribution,  $E_{l,\text{ext}}$ , the induced (Hartree) contribution,  $E_{l,\text{ind}}$ , and the exchange–correlation field,  $E_{XC,l}$ .

In the “standard” approach to transport, it is the conductance based on this quantity  $\sigma^{KS}$  that is calculated:

$$G^{KS} = \int d\mathbf{x}_\perp d\mathbf{x}'_\perp \hat{x}_k \sigma^{KS}(\mathbf{x}, \mathbf{x}', \omega)_{kl} \hat{x}_l \quad (7.6)$$

The total current,  $I$ , is related to the Kohn–Sham conductance,  $G^{KS}$ , via the effective Kohn–Sham voltage drop  $V^{KS}$ , eq. 7.7.

## How big are the differences between $G$ and $G^{KS}$

An important open question is, how big the differences between the Kohn–Sham conductance,  $G^{KS}$ , and the exact conductance,  $G$ , actually are. As we

do not know the exact form of the exchange–correlation functional, no exact answer is possible.

But a qualitative discussion can be done. We will now present a one-dimensional example to analyze the differences. In 1 D the current,  $I$ , can be written as

$$I(\omega) = G^{KS} \int dz (E_{\text{ext}}(z, \omega) + E_{\text{ind}}(z, \omega) + E_{XC}(z, \omega)). \quad (7.7)$$

in terms of the effective Kohn–Sham system, with the electric field contributions as described above.

Alternatively, the current takes the form

$$I(\omega) = GV, \quad (7.8)$$

where the measured voltage is

$$V = \int dz (E_{\text{ext}}(z) + E_{\text{ind}}(z)). \quad (7.9)$$

Note that this measured voltage is different from the effective voltage drop that is felt by the Kohn–Sham particles, due to the long-ranged exchange–correlation contributions ( $E_{XC}$ ).

We can now calculate the difference for the conductances of the two descriptions, which yields

$$\Delta G = G - G^{KS} = \frac{G^{KS}}{V} \int dz E_{XC}(z, \omega). \quad (7.10)$$

How big is this difference?

The exchange–correlation field of the Kohn–Sham system should give an additional contribution to the screening of the externally applied field. If this screening is efficient, the conductances can differ strongly.  $G$  can be much smaller than the Kohn–Sham value  $G^{KS}$ .

From the results of chapter 6 we know that the difference indeed can be large for molecular systems like benzene, where measured conductance and conductance calculated in the scattering approach differed by several orders of magnitude. Let us now look at the size of the exchange–correlation field within different approximations for the exchange–correlation functional.

Within a local density approximation (ALDA in TD-DFT), there exists a simple relationship between the exchange–correlation potential,  $v_{XC}$ , and the exchange–correlation field,  $E_{XC}$

$$E_{XC} = -\partial_z v_{XC} \quad (7.11)$$

So, the difference is just the difference between the exchange–correlation potential on the right and on the left.

$$G - G^{KS} = \int dz E_{XC}(z) = -v_{XC}^r + v_{XC}^l. \quad (7.12)$$

As, within LDA, the  $v_{XC}^{l,r}$  just depends on the local density,

$$v_{XC}^{ALDA}(z) = v_{XC}^{ALDA}(n(z)) \quad (7.13)$$

and the electron densities  $n_{l,r}$  are the same on both sides, the contribution is zero.

$$\Delta G^{ALDA} = 0. \quad (7.14)$$

This means, using time–dependent DFT within the adiabatic local density approximation (ALDA) gives exactly the same result as equilibrium DFT. In this approximation we gain nothing in using TD–DFT. Within GGA the result is the same. Only long–range corrections in the exchange–correlation potential make a difference:

In DFT, the Hartree term of the Coulomb interaction contains an unphysical self–interaction term (see §4.7.3). This has to be canceled by the exchange part of the exchange–correlation potential, which therefore has a long–range contribution. In exact exchange, this is done correctly, but not in GGA or LDA. So, long–range contributions exist already in the equilibrium case. For small systems like benzene, we have seen, when comparing Hartree–Fock (where exchange is exact) and equilibrium DFT (§7.1), that these can account for a large correction.

There are other long–range contributions as well, that are not contained within the equilibrium approach. One extra term is described in [148] for large frequencies and slowly varying density. This extra contribution is due to the viscosity and elasticity of the electron fluid. We are currently working on implementing these corrections.

### 7.3 Time–dependent DFT in the quasistationary limit and scattering formalism

The Landauer–Büttiker formula for the transmission in the regime of linear response and zero temperature given by eq. (3.32)

$$T(E) = \text{Tr} [\Gamma_L \mathbf{G}_C^r \Gamma_R \mathbf{G}_C^a] \quad (7.15)$$

holds for interacting systems if we use time-dependent DFT and if certain assumptions are being made (see below). We will demonstrate this in the following.

We will first introduce a concept how to construct a regime of quasistatic non-equilibrium, where we can use time-dependent DFT to calculate the conductance and obtain in principle exact, quantitative results.

For TD-DFT the Runge-Gross theorem, described in §4.10.1, states that the time evolution of *any* two-body Hamiltonian of an electronic system in an external time-dependent potential can be calculated by solving a corresponding single-particle problem in an appropriate effective potential,  $V_{\text{eff}}$ , via

$$-i\frac{d}{dt}\Psi_n(x) = \left(-\frac{1}{2m}\nabla^2 + V_{\text{eff}}(x)\right)\Psi_n(x) \quad (7.16)$$

where we use the abbreviation  $x = (\mathbf{x}, t)$  and the effective potential is given by

$$V_{\text{eff}}(x) = V_i(x) + V_H[n(x)] + V_{xc}[n(x)] + V_{\text{ext}}(x). \quad (7.17)$$

$V_i(x)$  denotes the ion-core potential from the Born-Oppenheimer approximation. The Hartree potential  $V_H[n(x)]$  as well as the exchange correlation potential  $V_{xc}[n(x)]$  are functionals of the time-dependent density and  $V_{\text{ext}}(x)$  represents the external probing field, e.g. the applied voltage. In addition to the obvious explicit time dependence of the effective potential,  $V_{\text{eff}}$ , caused by the time-dependent probing field, an implicit dependence arises as  $V_{\text{eff}}[n(\mathbf{x}, t)]$  is a functional, in general nonlinear and nonlocal in time and space, of the density  $n(\mathbf{x}, t)$ .

For our derivation, we will now discuss the following setup: a molecule is placed in between two leads, described by the effective single-particle equation, eq. 7.16, in an external perturbation potential  $V_{\text{ext}}(\mathbf{x}, t)$  that is switched on at time  $t = t_0$  and which is time-independent thereafter:

$$V_{\text{ext}}(\mathbf{x}, t) = V_{\text{ext}}(\mathbf{x})\Theta(t - t_0). \quad (7.18)$$

The system is in thermal equilibrium at  $T = 0$  before the perturbation is switched on.

This motivates us to characterize the reservoirs by their occupation numbers  $f_n$  obeying a Fermi-distribution. Then, the density can be expressed with the Keldysh Greens-function

$$G_V^<(x, x') = \sum_n f_n \Psi_n(x) \Psi_n^*(x') \quad (7.19)$$

where the time evolution of the wavefunctions  $\Psi_n(\mathbf{x}, t)$  is given by eq. 7.16 as

$$n(x) = G_V^<(x, x). \quad (7.20)$$

For applications to molecular electronics it is useful to regard the special case, where the external potential  $V_{\text{ext}}$  creates a monotonous electrical potential drop from the potential  $V_0$  in the left lead far away from the molecule to potential  $V_{\text{ext}} = 0$  far within the right lead.

In response to this potential drop a current will be created. In the initial period we will observe transient behavior but after the perturbation has acted for a sufficiently long period of time, the current and the density will be quasistationary for a parametrically wide time interval. This situation is then equal to the one, the Meir–Wingreen formula was derived for. At much larger times, determined by the size of the reservoirs, the potential drop will have decayed to zero and the current will stop to flow as the potential will be homogeneous again.

Formally this can be translated into performing the limits for system size and time elapsed after switching on the perturbation in the following way:

- First, increase the size of the reservoirs to infinity
- Then, perform the limit  $t_0 \rightarrow -\infty$ .

As we are only interested in the long–time behavior (the quasi–stationary period) the details of how the perturbation is switched on *do not* influence the result. The corresponding memory will be completely erased in the reservoirs by the time we are looking at the quasistationary current.

Before presenting the method for calculating the current, we will elaborate some more on the conditions required to assume the system to be in a quasistationary state, as this is not that straightforward.

In fact, the density for example may not become stationary if the memory of the switch–on process is preserved by some existing conserved quantities. This can be illustrated using the following example: a molecular contact, where current flows from a left reservoir to a right reservoir as described above: immediately after the external potential has been switched on, the current will start to flow. It will be accompanied by a propagating density wave. This is due to momentum conservation and will prevent the density to become strictly time–independent in the entire system.

But as we are interested in a formulation of transport in terms of incoming and outgoing scattering states, we only need to know, whether we are allowed to approximate the occupation of the incoming waves with wavevector  $\mathbf{k}$  by a Fermi–Dirac distribution with a time–independent temperature and chemical potential. For non–interacting lead electrons, this is certainly true as in that case the incoming waves are completely decoupled from the outgoing ones. If

the electrons in the leads are interacting, the situation becomes much more complicated: for instance, the outgoing, propagating modes can interact with the incoming scattering waves whose distribution can be modified. This would then have an effect on the current in first order in the applied external voltage. Moreover, it is known that the exact current exchange-correlation functional has terms proportional to the current density, which are long-ranged. It is not known, and certainly not unconceivable, that also these are going to modify the Fermi-Dirac distribution of the incoming scattering states.

One of the basic assumptions underlying the scattering approach is, that the conductivity of the leads is so large that the voltage drop occurs only in the vicinity of the molecule with its contacts. This then implies an almost homogeneous chemical potential within the leads, but it does not fix its value, i.e., the potential in general does not need to be identical to the experimentally observed one. For non-interacting electrons this is clearly true, but for the Kohn-Sham system this is not necessarily the case (see previous section).

Now, we will give an argument how we can actually calculate the current in terms of scattering states under the assumption that the occupation of the incoming scattering states is Fermi-Dirac with some chemical potential  $\mu_{L,R}$ . Their values can (in general) not be obtained from a stationary calculation. Instead a full time propagation is necessary.

We have just demonstrated that the time-dependent Kohn-Sham equations can describe a quasi-stationary limit, in which the exchange-correlation functional is time-independent. Thus the solution of the quasi-stationary Kohn-Sham equations will equip us with scattering states, that in turn may be used to construct  $\mathbf{G}^<$ , in precisely the same way that has been adopted in the non-interacting case (§3.2.3):

$$\mathbf{G}^<(\mathbf{x}, \mathbf{x}') = \sum_{nL, nR} f_L \Psi_{nL}(\mathbf{x}) \Psi_{nL}^*(\mathbf{x}') + f_R \Psi_{nR}(\mathbf{x}) \Psi_{nR}^*(\mathbf{x}') \quad (7.21)$$

where the Kohn-Sham states  $\Psi_{L,R}(\mathbf{x})$  represent the scattering states in the quasistationary non-equilibrium situation. Their zero temperature occupation numbers are given by the Fermi-Dirac distributions  $f_{L,R}$  of the respective reservoirs.

As has been done in the non-interacting case (see §3.2.3), it is possible to derive an equation for the Keldysh Green's-function, equivalent to 3.37 in an analogous way for the fully interacting system

$$\mathbf{G}_V^< = i\mathbf{G}_V(f_L\mathbf{\Gamma}_L + f_R\mathbf{\Gamma}_R)\mathbf{G}_V^\dagger. \quad (7.22)$$

Using this expression and the corresponding retarded Greens-function  $\mathbf{G}_V$ , we can obtain an analogous equation for the *dc*-transmission

$$T = \text{Tr}(\Gamma_L G_V \Gamma_R \mathbf{G}_V^\dagger) \quad (7.23)$$

where the retarded Green’s–function is defined in the usual way,

$$\mathbf{G}_V(E) = (\mathbf{G}_{0V}^{-1} - \Sigma_L - \Sigma_R)^{-1}, \quad (7.24)$$

and the unperturbed Greens–function of the central cluster is given in its Lehmann representation

$$G_{0V}(\mathbf{x}, \mathbf{x}', E) = \sum_n \frac{\Psi_n(\mathbf{x})\Psi_n(\mathbf{x}')}{E - E_n + i\eta} \quad (7.25)$$

using the Kohn–Sham states,  $\Psi_n(\mathbf{x})$ , obtained from the self-consistent solution of the Kohn–Sham equations (§4.10) in the presence of a finite current.

This result constitutes a generalization of the Landauer–Büttiker formula to interacting electron systems.

Meir and Wingreen [65] already derived this expression for the special case of proportional couplings  $\Gamma$ , where  $\Gamma_L$  and  $\Gamma_R$  differ by a constant factor only. But we emphasize that this condition proved to be extremely restrictive, whereas the formula obtained by us is now valid *in the general case*. The condition of proportional couplings implied, that every atom of the molecule was coupled in precisely the same way to the left lead as it is coupled to the right lead. Given the fact that physical couplings decay with increasing spatial distance, the condition of proportional couplings is violated for every realistic system with finite dimensions.

### Remarks concerning the ingredients

- **Defining the *extended molecule* and the Self–Energies**

As in the noninteracting case, the self energies  $\Sigma_{L,R}$  account for the coupling of the molecule to the leads. In the interacting case, it is well known that the self–energies of the real Green’s–function of the molecule plus leads incorporate sophisticated many–body effects, for example *Abrikosov–Suhl* resonances if we are in the Kondo physics regime (see, e.g., [98]). So, we again have to pay attention to including enough gold atoms in the *extended molecule* to ensure that all effects of interest are included in  $\mathbf{G}_{0V}$ , already.

- **Assumptions:  $T \rightarrow 0$ ,  $\omega \rightarrow 0$ , and linear response**

We have derived expression 7.23 in the scattering picture under some assumptions:

We restricted ourselves to the condition of vanishing temperature and frequency in the linear response regime. Under these restrictions, scattering is energy conserving and therefore an effective

single particle description of transport using scattering states is possible.

But if we release these constraints, the incoming electrons can exchange energy with the molecule and thus qualitatively new phenomena can occur. The scattering problem will then, in general, become far more complicated and it will perhaps not be possible to treat it in an effective single-particle approach any more.

One example for such an additional complication are memory effects, as an incoming electron will find the molecule in a state caused by the interaction of preceding electrons with the molecule.

However, using the TD-DFT formalism in general to obtain the current via the time-dependent density and the continuity equation does not have these restrictions.

- **Time-independence of the exchange-correlation potential**

We have assumed the exchange-correlation potential  $V_{xc}^V$  to be time-independent in the quasistatic non-equilibrium situation. Logically, the fact that observables are stationary does not necessarily imply that the exchange-correlation functional itself is stationary. In fact, examples are known, where this is not the case.

Here, we will give an explicit construction of  $V_{xc}^V$  valid in the linear response regime, that indeed shows, that it is independent of time in our case.

The deviation of  $V_{xc}^V(\mathbf{x}, t)$  from the equilibrium  $V_{xc}^0(\mathbf{x})$  can be written as

$$\delta V_{xc}(\mathbf{x}) = \int d^3x' dt' f_{xc}(\mathbf{x}, \mathbf{x}', t - t') e^{-\eta(t-t')} \delta n(\mathbf{x}', t') \quad (7.26)$$

where the exchange-correlation kernel is given by

$$f_{xc}(\mathbf{x}, \mathbf{x}') = \frac{dV_{xc}(\mathbf{x})}{dn(\mathbf{x}')}. \quad (7.27)$$

This kernel produces a linear density response of the Kohn-Sham system, which is by construction identical to the true interacting density response. Here,  $\eta$  is the usual convergence factor known from linear response theories. This takes into account environmental dissipative effects not included in the exchange-correlation kernel  $f_{xc}$ . For stationary densities,  $n(\mathbf{x}, t) \rightarrow n(\mathbf{x})$ , the time integral in eq. (7.26) exists, so that a well defined asymptotic behavior of the exchange correlation potential as

$$\delta V_{xc}(\mathbf{x}) = \int dx' \delta n(\mathbf{x}') dt' f_{xc}(\mathbf{x}, \mathbf{x}', t - t') e^{-\eta(t-t')} \quad (7.28)$$

is ensured.



# Chapter 8

## Symmetry and transport

### 8.1 Motivation

Even though quantitative results from DFT-based transport calculations are difficult to obtain, qualitative features can be given quite reliably. In this chapter, we will discuss as an example the effect of symmetry on transport. DFT does give the exact symmetry properties so we expect to be able to obtain qualitatively correct results.

Molecules can have exact symmetry properties that are related to their structure. This can lead to new selection rules and additional physics compared to quantum dots, where these effects cannot be observed. An example: conductance takes place via single, hybridized orbitals that extend over the combined system of molecule plus neighboring gold atoms, thus connecting left and right lead in the scattering picture. Changes in the symmetry of the system can have a pronounced influence on the conductance by modifying the orbitals that carry the transport and thus their transparency. Again, we will illustrate this using the symmetric, anthracene type molecule from section §6.2.

### 8.2 *Para* and *meta* couplings and the conductance

The coupling of the symmetric, anthracene type molecule from §6.2 (see also fig. 8.1), to the gold via the sulfur atom can be done in several ways by placing the sulfur atom at different positions on the outermost benzene ring, resulting in different symmetry properties of the molecule.

In the molecules investigated in the chapters above, the acetyl-protected *thiol* end-group was always positioned on the terminal benzene rings in the *para* position, i.e., aligned with the symmetry axis of the molecule, see fig. 8.1.

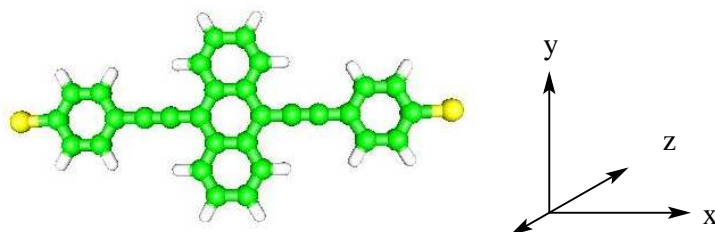


Figure 8.1: Symmetric, anthracene type molecule of §6.2 with the sulfur (yellow) in *para* position on the terminal benzene rings. The contact to the gold is again via covalent bonds formed between the sulfur atom and the gold electrodes.

We will now first analyze the symmetry properties of the bare molecule: the bare molecule is highly symmetric ( $d_{2h}$  symmetry). In particular, it has three mirror planes ( $x$ - $y$ ,  $y$ - $z$ ,  $x$ - $z$ ) and current flow is along the axis, where two mirror planes intersect ( $x$ -axis).

If we look at the highest occupied molecular orbital (HOMO) and the states close in energy to it, they should be symmetric with respect to the  $x$ - $z$  plane. In the antisymmetric case, they would have nodes along the  $x$ -axis, resulting in a localization of the  $\pi$ -system, which would be costly in energy.

If we now add the sulfur in the *para* position, as depicted in the figure 8.1 the situation does not change: the sulfur respects all symmetries of the bare molecule and thus can be relatively strongly coupled to the  $\pi$ -system. We would therefore expect the conductance to be large in this case. The  $\pi$ -system could extend into the neighboring gold atoms.

Using the symmetric anthracene type molecule, the coupling position was varied: a second molecule, where the sulfurs are positioned in the *meta* position (see fig. 8.2), was synthesized by M. Elbing and M. Mayor [151] at our institute. With the sulfur in the *meta* position, the situation changes strongly: the sulfur atom breaks most of the symmetries of the molecule. Two of the mirror planes ( $x$ - $z$  and  $y$ - $z$ ) are no longer present.

Now, the sulfur can only couple to a part of the molecule, if the structure of the HOMO is completely changed. Strong mixing of symmetric and antisymmetric orbitals would be necessary. But this cannot happen, as symmetric and antisymmetric states have very different energies. If the HOMO keeps the symmetry of the bare molecule—as changing it would be energetically expensive—the coupling between sulfur and HOMO can only be weak. In con-

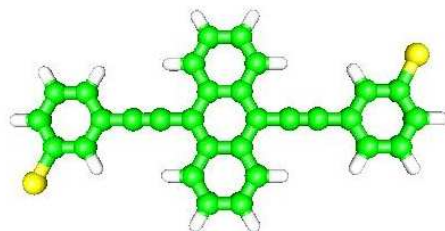


Figure 8.2: Molecule similar to the symmetric molecule of §6.2. But now, the sulfur (yellow) is attached in the meta position on the terminal benzene rings. The contact to the leads occurs via covalent bonds between the sulfur atoms and the gold electrodes.

clusion, the sulfur will only couple weakly to the molecule and we expect the conductance to be low. Electrochemical investigations [152] showed, that the conjugation of the  $\pi$ -system indeed is reduced in the *meta* position.

### 8.2.1 Numerical conductance calculations

In order to see, whether in agreement with our reasoning above, the change in symmetry reduces the conductance, we performed DFT calculations. For our transport calculation, the extended molecule in the DFT run consisted of the actual molecule itself plus two *fcc* gold pyramids of 55 atoms each, as described previously in the section 6.2 above. The structure of the molecule and the sulfur bond to the gold was allowed to relax completely.

Results for the molecule with sulfur in the *para* position were already discussed above (see §6.2), were we considered different coupling types (sulfur coupling to 1, 2 and 3 gold atoms). In the *meta* case, we also considered two different bonding variants, the sulfur coupling to two, and to three gold atoms.

Our findings are presented in fig. 8.3. In the upper panel, the data of the *para* coupled molecule, as presented in §6.2, is shown. The different traces correspond to the sulfur coupling to one, two, and three gold atoms. The transmission is plotted in units of the quantum of conductance,  $g_0$ . The lower panel then displays our conductance calculations for the *meta* coupled variant. The transmission for the S—Au<sub>2</sub> coupling is depicted with black  $\Delta$ , the S—Au<sub>3</sub> coupling as blue  $\times$ .

Comparing the transmission of the *para* and *meta* calculations we observe, as expected, a suppression of the transmission in the *meta* case. Looking at the transmission at the position of the first peak,  $E = -5.3\text{ eV}$  and  $E =$

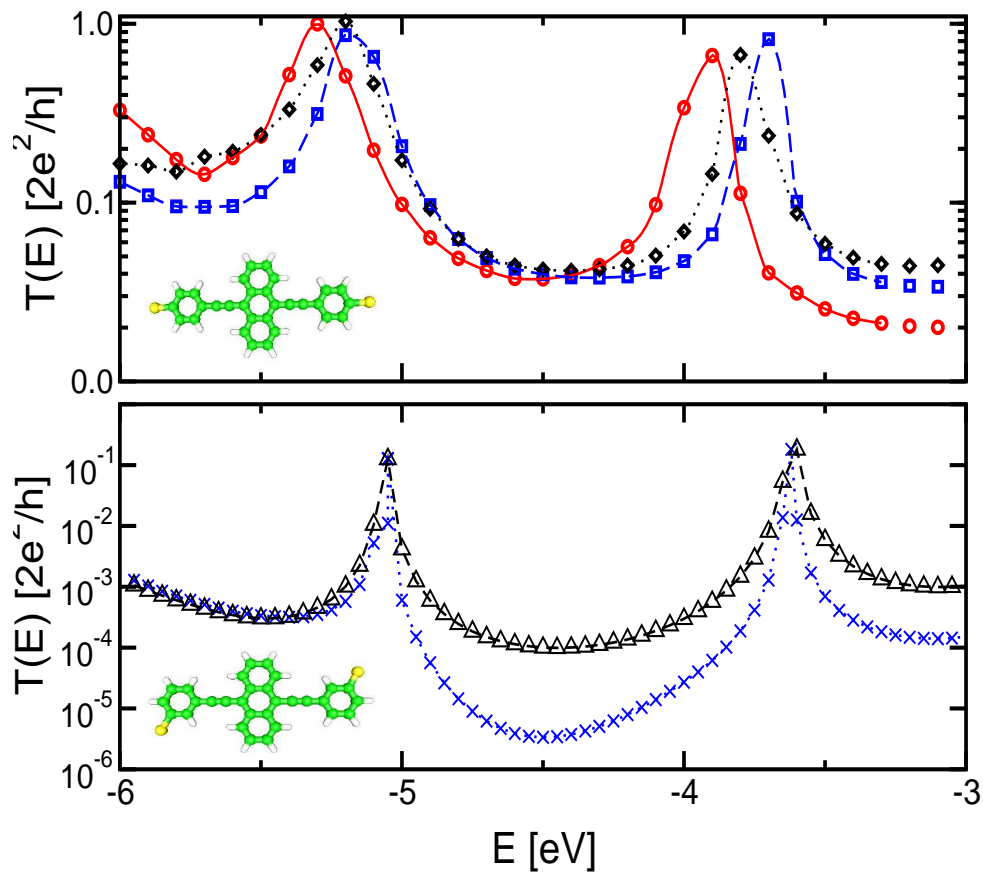


Figure 8.3: Influence of symmetry on the conductance. Upper panel: Transmission over energy for the symmetric, anthracene-type molecule with the sulfur attached in the *para* position. The different traces correspond to the sulfur coupling to one (red,  $\circ$ ), two (black,  $\square$ ), and three (blue,  $\diamond$ ) gold atoms. Lower panel: same as upper panel with sulfur in *meta* position. S coupling to two (black,  $\triangle$ ), and three (blue,  $\times$ ) gold atoms. The insets depict the molecule the calculation applies to.

$-5.1\text{ eV}$  respectively, conductance in the meta case,  $0.1 g_0$ , is about an order of magnitude smaller than the value for the para coupled molecule,  $1 g_0$ . In accordance with this, in the *meta* case, the peak is very narrow, broadening due to coupling to the leads is strongly suppressed.

If we now look at the differences caused by the sulfur-gold bond type in both cases, a second interesting conclusion can be drawn: Whereas in the *para*-coupled molecule, the different bond variants resulted in shifts of the peak positions as well as modified peak shapes (see §6.4 above for a more detailed discussion), the influence for the *meta*-coupled molecule is smaller.

Considering the peak positions, we observe that in the *para* case, all peaks are shifted to slightly lower energies compared to the *meta* coupled molecule. This is caused by a stronger hybridization of the HOMO and LUMO with the states of the gold in the higher conducting *para* molecule, resulting in a lower energy of these orbitals. The different couplings cause only slight modifications in the transmission behavior at the resonances when the sulfur is in the *meta* position.

## 8.2.2 Structure of the molecular orbitals

To further support our analysis of the transport properties, we can take a direct look at the different molecular orbitals that contribute to the conductance in both systems. The differential conductance peak slightly below the Fermi energy corresponds to the highest occupied molecular orbital (HOMO), therefore we plot the HOMO for the *para*-coupled molecule in fig. 8.4.

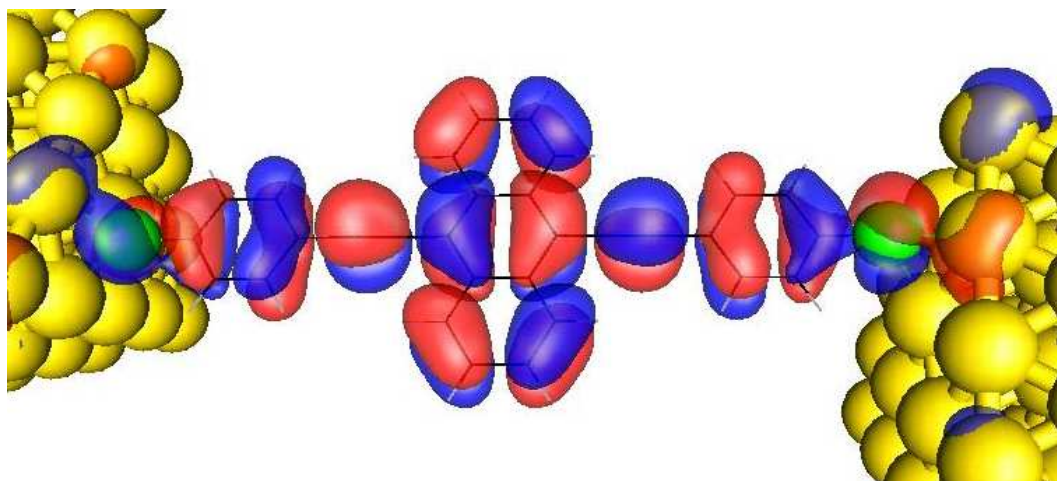


Figure 8.4: Highest occupied molecular orbital (HOMO) for the symmetric molecule of fig. 8.1, with the sulfur atom in the *para* position. Gold electrodes are depicted in yellow, the sulfur is displayed in green. The colors of the orbitals visualize the sign of the wavefunction.

In agreement with the symmetry analysis above, the structure of the conjugated  $\pi$ -system, covering the benzene ring extends to the sulfur atom and beyond well into the leads. This results in a high transparency of this orbital for transport and thus a high conductance at the HOMO energy.

In the *meta*-coupled variant of the molecule, the situation is completely different. The HOMO is shown in fig. 8.5.

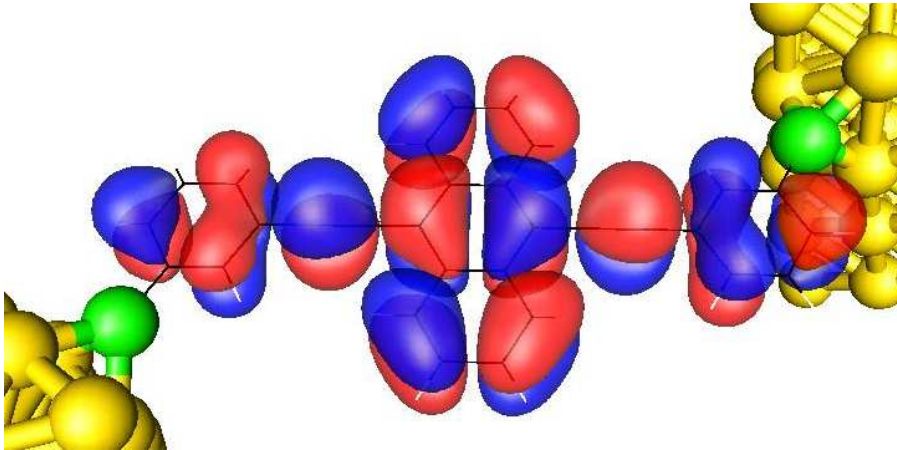


Figure 8.5: Highest occupied molecular orbital (HOMO) for the symmetric molecule of fig. 8.1, with the sulfur atom in the *meta* position. Gold electrodes are depicted in yellow, the sulfur is displayed in green. The colors of the orbitals visualize the sign of the wavefunction.

The reduced symmetry in the *meta* case results in a restriction of the conjugated  $\pi$ -system to the benzene ring only. The  $\pi$ -system is largely decoupled from the sulfur as well as the adjoining gold atoms. This explains the low transparency of the HOMO and in consequence the only weakly developed peak in the differential conductance.

### 8.2.3 Experimental results

The experimental data indeed shows the expected decrease in conductance, when the sulfur is attached in the *meta* position. In fig. 8.6 we present a measured current-voltage characteristics of the *meta*-coupled molecule [11, 153].

The red curve shows current over voltage, whereas the differential conductance is plotted in blue. Different traces correspond to consecutive voltage sweeps in the experiment. For comparison, data for the molecule with sulfur in the *para* position, which we have already discussed in section §6.2, is plotted in fig. 8.7.

Both I-V curves exhibit a conductance gap for low bias voltages and an onset of the conductance at about 0.5 V applied bias voltage. Looking at the differential conductance for an applied bias of about 1 V, a pronounced difference is visible: the *meta*-coupled molecule exhibits a value of about  $0.02 \mu S$ , corresponding to about  $2.5 \cdot 10^{-3} g_0$ , whereas the *para*-coupled molecule has a differential conductance of  $0.2 \mu S \approx 2.5 \cdot 10^{-2} g_0$ . The *meta*-coupling in this example reduces the differential conductance by one order of magnitude, which is in

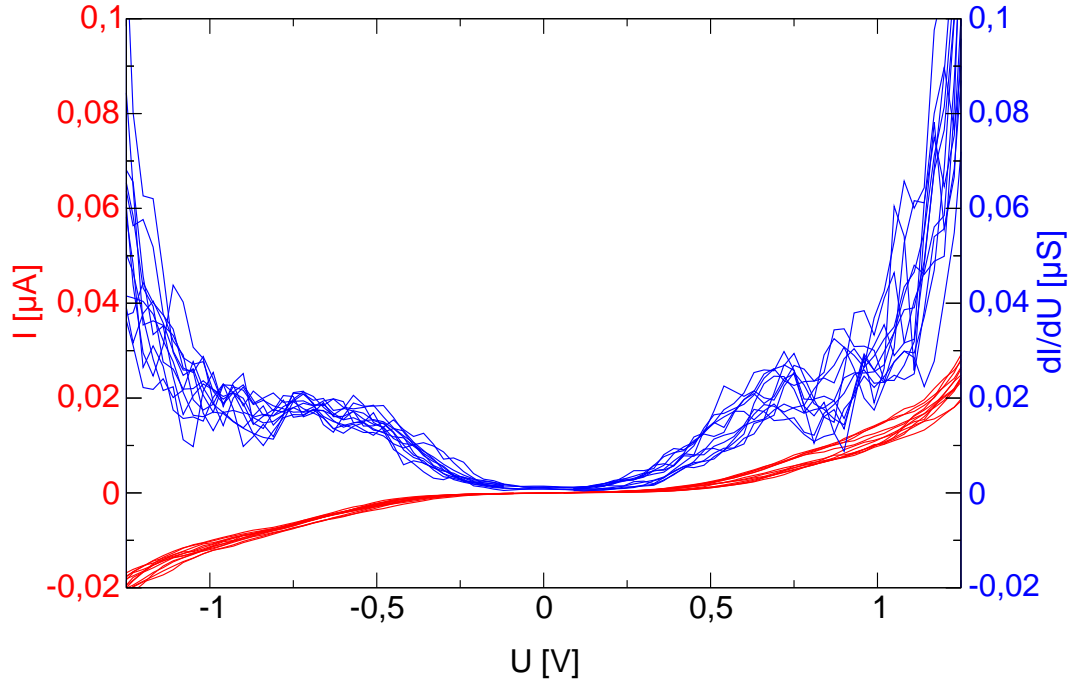


Figure 8.6: Conductance measurement of the symmetric molecule of fig. 8.2, with the sulfur in *meta* position. Red: current over applied bias voltage in  $\mu\text{A}$ . Blue: differential conductance in  $\mu\text{S}$ . Different traces correspond to different voltage sweeps, [11].

agreement with our theoretical calculations. For the zero-bias conductance the effect is of similar size: the *meta*-coupled molecule exhibits a value about a factor of 10 smaller than the *para*-coupled molecule.

For all I-Vs measured (approximately 80), the current at 1 V varied in the *meta* case between 5 and 25 nA whereas the values for the *para*-coupled molecule ranged between 25 and 150 nA, corresponding to a factor of 5 to 30 for the total conductance at 1 Volt [153].

It is thus clearly visible, that the conductance is strongly decreased by attaching the sulfur in the *meta* position, supporting our analysis, that the conjugated  $\pi$ -system is disturbed by breaking the symmetry. The main conclusion to be drawn is that the symmetry analysis gives a qualitatively correct prediction. Also, qualitatively our calculations for the *meta* coupled molecule agree with the experimental observations, as observed previously for the *para* case (§6.2). A low zero-bias conductance is followed by a transmission peak slightly below the Fermi energy ( $\approx 5\text{ eV}$ ), at about  $5.1\text{ eV}$ , corresponding to a peak in the differential conductance for a bias voltage of  $0.2\text{ V}$ .

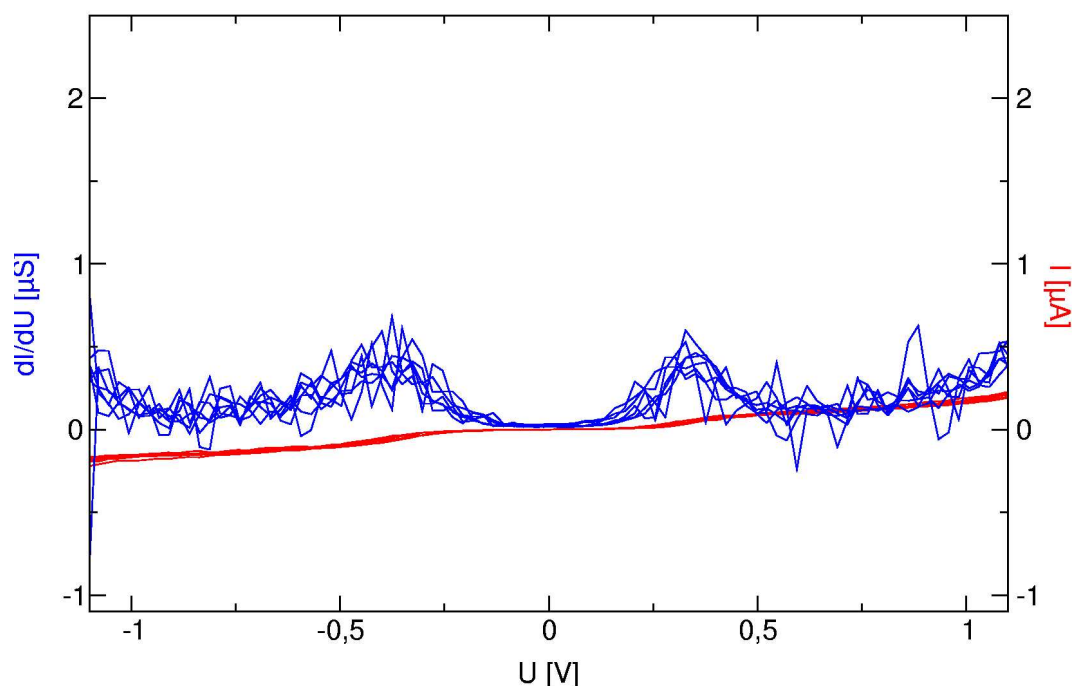


Figure 8.7: Conductance measurement of the symmetric, anthracene-type molecule of fig. 8.1, with the sulfur in *para* position. Black: current in  $\mu\text{A}$  over applied bias voltage in  $V$ . Blue: differential conductance in  $\mu\text{S}$ . Different traces correspond to consecutive voltage sweeps.

### 8.2.4 Summary

Summarizing, we have gained interesting insights from the analysis of the *para* versus the *meta* coupling:

First, DFT calculations illustrate aspects of symmetry essential for transport and give a correct qualitative account of the impact of symmetries on transport:

Breaking the symmetry of the molecule by attaching the sulfur in the *meta* position significantly decreases the conductance by restricting the conjugated system to the benzene rings and thus effectively decouples the gold from the molecule.

Second, this decoupling can strongly reduce the dependence of the transport properties on the actual microscopics of the sulfur—gold bond. And thus this could be a method to increase the reliability and reproducibility of current-voltage curves in break-junction experiments.

# Chapter 9

## Three terminal devices: describing a gate electrode

### 9.1 Motivation and idea

In the previous chapter we have seen that DFT can be a useful tool in providing qualitative information on transport—even though large quantitative discrepancies, e.g., due to missing non-equilibrium effects in the exchange–correlation functional exist. In this chapter, we will demonstrate that even based on equilibrium–DFT calculations, crucial information on the transport properties can be obtained, that are in principle exact.

The idea is, to consider an experimental setup with a tunable parameter. A prototypical example is a molecule subjected to a gate electrode. Using the gate voltage as an external parameter, we can study the local change in the ground–state electron density on the molecule under a changing gate voltage. From the evolution of the density with the gate voltage we can obtain information on Coulomb blockade like charging effects. As this conceptually constitutes an equilibrium situation where there is no current flow, we expect the ground–state DFT approach to deliver in principle *exact* results. Their quality is constrained only by the approximations in the equilibrium exchange–correlation functional (§4.7). This is a tremendous advantage, as a lot is known about the equilibrium functional, whereas at present only very little is known about the quasistationary limit of the non–equilibrium exchange–correlation functional.

Information pertaining to transport can be deduced by studying the evolution of the resonances in the transmission characteristics as a function of the applied gate voltage. Fig. 9.1 shows a schematic level structure for a molecule in

between gold leads. We assume, the molecule is weakly coupled to the electrodes via the covalent sulfur bonds, i.e., level broadening  $\gamma$  is small compared to the level spacing  $\Delta$  ( $\gamma \ll \Delta$ ). By varying the applied gate voltage, we can shift the levels of the molecule.

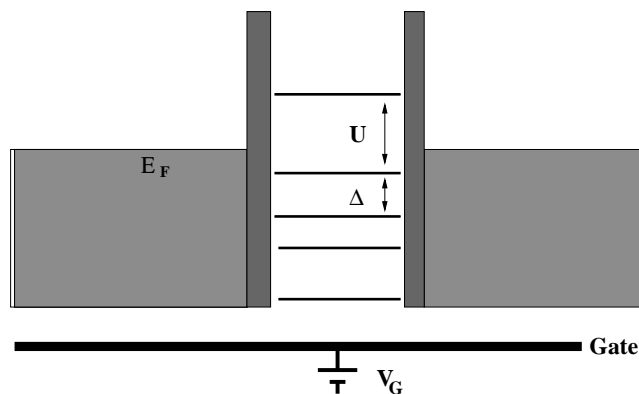


Figure 9.1: Schematic representation of a weakly coupled molecule with a gate electrode: level scheme with level spacing  $\Delta$ , Coulomb charging energy  $U$ , Fermi level  $E_F$ . An applied gate voltage,  $V_G$ , shifts the levels of the “molecular quantum dot”. The molecule is weakly coupled; level broadening  $\gamma \ll \Delta$ .

When a level crosses the Fermi energy, the level gets occupied (or vacated) by electrons entering from the leads. The corresponding gate voltage,  $V_G$ , should, by virtue of the Hohenberg–Kohn theorems (§4.2.1), be given exactly by equilibrium DFT. At this value of  $V_G$  one should observe a peak in the differential conductance, as a new channel opens up. Thus, studying the evolution of the levels, we expect to be able to predict the peak positions similar to the case of the *coupled quantum double dot molecule* we will study below in chapter 10.

Many important building blocks for functional molecular electronics devices are of three terminal design, e.g., single molecule transistors. A theoretical description of a gate electrode is an important prerequisite to study such three terminal devices theoretically. Interesting questions include the study of transport properties as a function of the gate voltage as well as charging effects, like Coulomb blockade. Also of interest are possible structural/conformational changes of the molecule, when a gate voltage is applied. This new and interesting aspect is unique to these molecular devices and absent in conventional quantum dot systems. New interesting physics can be studied. Also such conformational changes might be utilized in the design of single-molecule switches.

## Motivation: experiments

On top of the theoretical motivation there is also a strong experimental drive that triggers our interest in gated molecular structures. Recently, fascinating experiments that studied the influence of a gate electrode on the conductance properties of single molecules were reported [16, 25, 26, 154]. We will now present three, which we are currently studying theoretically: the first two experiments were conducted using nanogaps fabricated by electromigration techniques (see §2.3). Using a particularly designed molecular system comprised of an organic ring system with a cobalt atom acting as the “impurity spin”, J. Park *et al.* [16] observed a Kondo resonance (see also §2.3). For a similar, but far less conducting molecule, Coulomb blockade was reported.

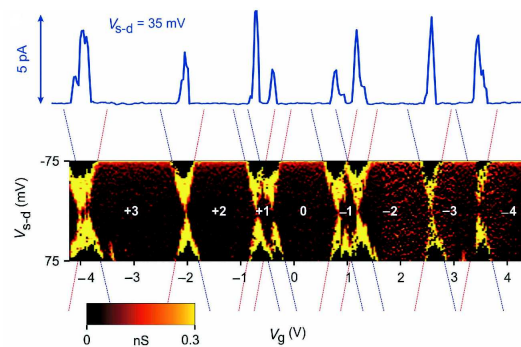


Figure 9.2: Coulomb blockade in a single molecule, from [154]: Gate dependent  $I$ – $V$  characteristics of a 5–benzene–ring molecule, studied by Kubatkin *et al.* Upper graph: Current over applied gate voltage at 35 mV source–drain voltage. Lower graph: Coulomb diamonds. Conductivity in nS. X–axis: gate voltage; y–axis: source–drain voltage. In white, the suggested charge state of the molecule is depicted.

Kubatkin *et al* [154] observed Coulomb blockade effects in a 5–benzene–ring molecule, where the rings were connected by carbon double bonds, resulting in a rigid, planar molecule with a conjugated  $\pi$ –system spanning the molecule. By applying a gate voltage they could detect Coulomb diamonds in the  $I$ – $V$  characteristics, corresponding to several charge states of the molecule, see fig. 9.2. The molecule studied did not contain terminal thio–acetyl groups, so no chemical bond to the gold electrodes was formed. Instead, it is suggested that the two terminal benzene rings of the molecule lie on top of the gold electrodes, with van der Waals forces between the surface and the  $\pi$ –system of the ring being the binding force.

We believe, that this is also the case in the earlier experiment [16] above, as this results in a strong hybridization of the orbitals of the gold electrodes with the

orbitals of the molecule and only then, the relatively large conductance necessary for the observation of a Kondo resonance can be achieved. We currently perform DFT calculations on this molecule, but the somewhat uncontrolled contact between molecule and electrode make the situation more complicated to treat numerically.

A third set of recent experiments that we are interested in, is reported by H. van der Zant *et al.* [25, 26]. There, the device is based on lithographically manufactured gold nanocontacts, where the final device gap to place the molecule in is produced by electrochemically etching the very thin ( $\approx 15\text{ nm}$ ) contact region. This process allows to control the electrode separation with sub-nanometer precision (see also §2.4.1) in contrast to the electromigration technique used in the two experiments above. A gate electrode is realized by structuring the device on an aluminum surface covered with a two to four nm thick oxide layer. This way, a very close distance of the gate electrode to the molecule of only a few nanometers can be achieved. This, together with the thin electrodes, ensures that the screening of the gate field by the gold is minimized and gate effects can be studied.

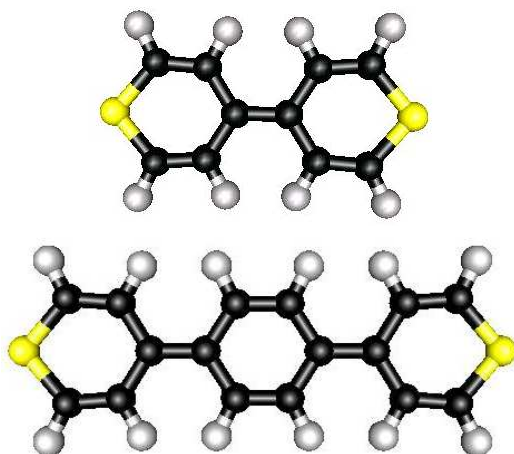


Figure 9.3: Gate effect in single molecules: organic molecules studied by H. van der Zant *et al.* [26]. The sulfur (yellow) for bonding to the gold electrodes is included in the terminal benzene ring. Carbon: black; hydrogen: grey.

The two molecules studied, consisted of two and three benzene rings, respectively, that were connected by carbon double bonds. The sulfur atoms for controlled contact to the gold electrodes were included *within* the terminal benzene rings, see fig. 9.3.

Both molecules show a pronounced conductance gap for low bias voltages in the experiment with an onset of the current at about 0.25 V for the 3-ring

molecule and 0.5 V for the 2–ring molecule. This supports the idea that we are in the Coulomb blockade regime, see fig. 9.4.

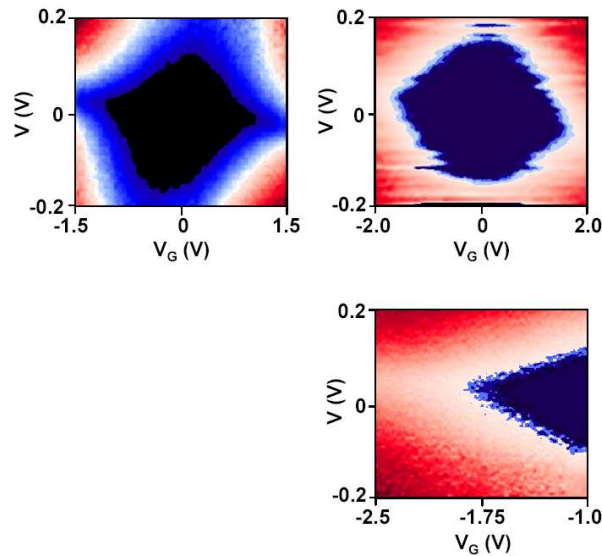


Figure 9.4: Gate effect in the 3–ring molecule of fig. 9.3. Experimental data by Kervennic *et al.* [26]. Differential conductance in dependence of the applied gate voltage  $V_g$  and the source–drain voltage  $V$ . Shown are three different samples. Scale: blue (0) to red (40nS).

When a gate voltage is applied, a strong gate effect can be observed in the 3–ring molecule. In fig. 9.4, the experimental data for three different samples with the 3–ring molecule are displayed. All three measurements show a smeared Coulomb diamond structure: for higher gate voltages, the required source–drain voltage to arrive at the onset of the current is reduced. However, there is no repetition of the diamonds. These are outside the experimentally accessible voltages, as the molecular junctions are destroyed at higher voltages.

Surprisingly at first, no gate dependence can be observed for the shorter, 2–ring molecule. We will see below (§9.2.2), that screening effects are strong. The absence of gate dependence in the two–ring case might thus be due to the small size of the molecule. In consequence, the field does not reach the molecule effectively and also the charging energy is higher, so that we stay within the low bias Coulomb blockade gap when sweeping the gate voltage.

## 9.2 How the gate is realized within DFT

We will now present, how a gate electrode can be implemented within the framework of DFT. We will also point out the considerations that have to be taken into account when choosing the geometry of the system.

### 9.2.1 Implementation

Within the Density Functional Theory description, we construct the gate electrode using a grid of additional point charges. These are realized as dummy atoms with a charge, but without basis states. Thus, they just lead to an extra electrostatic term in the Hamiltonian of our DFT system.

They are placed equidistantly in a grid, see Fig. 9.5. A gate voltage is then applied by distributing the appropriate charge equally on all dummy atoms.

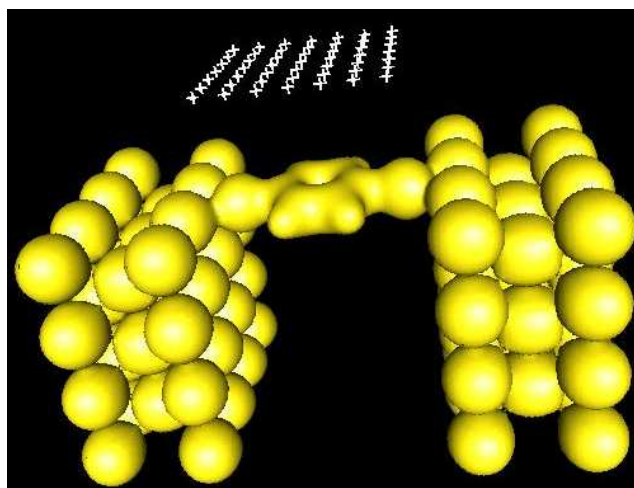


*Figure 9.5: The gate electrode is realized using 49 point charges. The charges are distributed equidistantly in a grid, depicted in white. The gold electrodes and molecule (benzene-1,4-di-thiol) are depicted in yellow.*

The electrical field caused by these charges will be screened by the cluster consisting of molecule and parts of the gold electrodes. In a system with macroscopic leads, the charges on the gate electrode would attract the same amount of screening charges of the opposite sign from “infinity”. These would screen the field created by the gate within some screening distance. To account for this screening in an appropriate way, we have to

- add the same amount of screening charges (with opposite sign), as we put on the gate dummy atoms, onto the extended cluster.

- choose the system large enough, so that effectively all screening takes place within the finite cluster.

If these conditions are satisfied, the screening is (in principle) included exactly in our calculation. The only approximations are due to the equilibrium DFT functional used.

The most serious defect is most likely the derivative discontinuity. It will lead to a smearing of the excess charge evolution on the molecule with the gate voltage, which is much bigger than the experimental width of the Coulomb blockade peaks (see §4.5). The peak positions, however, should be given correctly.

### 9.2.2 Finding the right geometry

Finding the appropriate geometry that can be used for modeling a gate electrode within the DFT framework is a difficult task. Thereby several parameters need to be optimized in order to obtain useful results:

- **Gate distance, extension and number of point charges**

The electric field created by the gate electrode should be homogeneous, so that the simple picture given in fig. 9.5 applies, and it should be strong enough to pull one or several charges on the molecule in order to be able to observe Coulomb blockade related effects.

Our tests showed, that distributing 49 point charges ( $7 \times 7$ ) is sufficient to model a square gate electrode and to produce a relatively homogeneous field suitable to study the molecule benzene, see fig. 9.6. Here we plot an equipotential surface of the field created by these charges. For calculations on the molecules of the experiment by van der Zant *et al.*, 91 ( $7 \times 13$ ) point charges were used.

In an actual experiment, the gate electrode is typically about 2 nm away from the molecule [26, 154]. A comparable distance is not achievable in our DFT approach due to several restrictions:

Instead of applying a gate voltage, we put charges on a grid to create the electric field. To account for screening requires us to add the same amount of countercharges to the extended molecule. However, the amount of charges we can add to molecule plus gold is limited. DFT calculations converge only for a few ( $\leq 20$ ) additional electrons on such a system. As we want to create a field, large enough to pull one or several electrons on the molecule, by the use of only a few electrons as

gate charge, the gate needs to be much closer. Test runs resulted in an optimum distance of about 1.5 gold lattice constants.

Current computer power restricts the system size we can treat in DFT calculations to about 4000 electrons. This implies that we can include about 70 gold atoms per electrode in the extended cluster (19 electrons per gold atom are treated independently within DFT). The screening has to be accounted for completely within this cluster, and the electron density at outer edges of the gold blocks should be unaffected by the gate induced field to avoid finite size effects. This results in a second limiting factor for the number of additional charges, we can put onto the cluster.

The gate electrode was designed to only cover the area of the molecule and not the gold electrodes, see fig. 9.5. This also ensures, that the charges are mostly pulled onto the molecule and not onto the neighboring gold atoms. In fig. 9.6 we depict an equipotential surface of the field created by our gate consisting of 49 gold atoms for a contact with a benzene-1,4-di-thiol molecule. It can be seen that the field reaches the molecule and is relatively homogeneous.

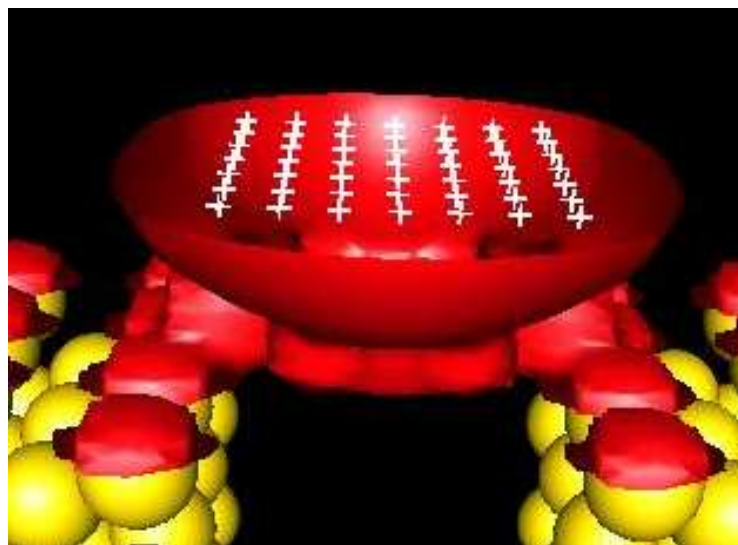


*Figure 9.6: Equipotential surface (4V) for the electrostatic field created by the gate. Gate charge  $+2e$ . The gate–molecule distance is approx. 1.5 gold lattice constants.*

- **Shape and geometry of the gold clusters**

The shape of the electrodes is not completely unimportant as it defines the electromagnetic vacuum the molecule lives in. However, the details of the electrodes in an actual experiment are not known and most likely vary from sample to sample. This allows us to choose the form of the

electrodes to our convenience. Therefore, in principle, is a large choice in the actual shape and geometry of the gold clusters to be included in the molecule as parts of the leads.

However, actual choices are very limited due to practical considerations, and picking a feasible one turns out to be very difficult. The reasons behind this apparent difficulty are manifold:

First, the geometry has to be chosen in a way that the electrodes do not shield the electric field from the molecule. Also, no point of the gold clusters in the extended molecule should be closer to the gate than the actual molecule, as otherwise charge would mostly accumulate on these gold atoms instead of on the molecule. For this reason we discard our standard geometry using pyramids. When the appropriate (relaxed) bond angle between sulfur and gold is satisfied, the extended molecule does not have a surface parallel to the gate and screening of the field as well as charge accumulation on the gold are a problem, see fig. 9.7.

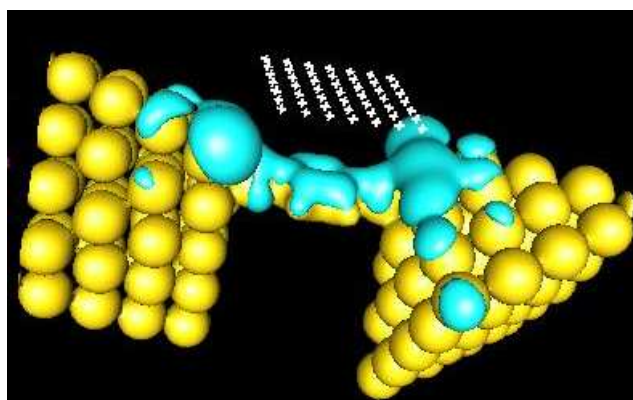


Figure 9.7: Gate electrode: original geometry as used for our transport calculations in chap.5. The extended molecule consists of the benzene-di-thiol molecule plus two 55 atom gold pyramids, depicted in yellow. Screening problems: the additional screening charge, attracted by a gate charge of  $-2e^-$ , is depicted in blue.

Tilting the pyramids to obtain a system, where one side of each pyramid lies in a common plane with the molecule, also is no solution. Then, the gold atoms of the two pyramids come very close to each other which leads to a second difficulty: direct coupling between the two clusters occurs, effectively short-circuiting the molecule when the distance between the gold clusters is too small.

These requirement alone would not be too complicated, but third, the actual geometry chosen should also be one, where the electronic structure in the DFT calculation converges and gives a physically appropriate,

i.e., similar to bulk gold, result. In other words, the Fermi energy and density of states close to  $E_F$  of the gold clusters should resemble bulk gold values. For some highly symmetric geometries for example, the symmetry leads to artificial degeneracies which results in an unphysically large level spacing. Many trial systems where we used, for example, two-layered rectangular or triangular Au(111) gold sheets, did not converge. The system that finally turned out to be appropriate consists of two *fcc* gold blocks, constructed of layers of  $3\times 3$  and  $4\times 4$  gold atoms, respectively. A sample cluster is shown above in fig. 9.5. In this design, the screening of the field the molecule is subjected to is easily minimized. The size of the electrodes is easily scalable by adding additional layers. Also, the *fcc* block structure proved to be converging best in the DFT calculations.

- Size of the electrodes

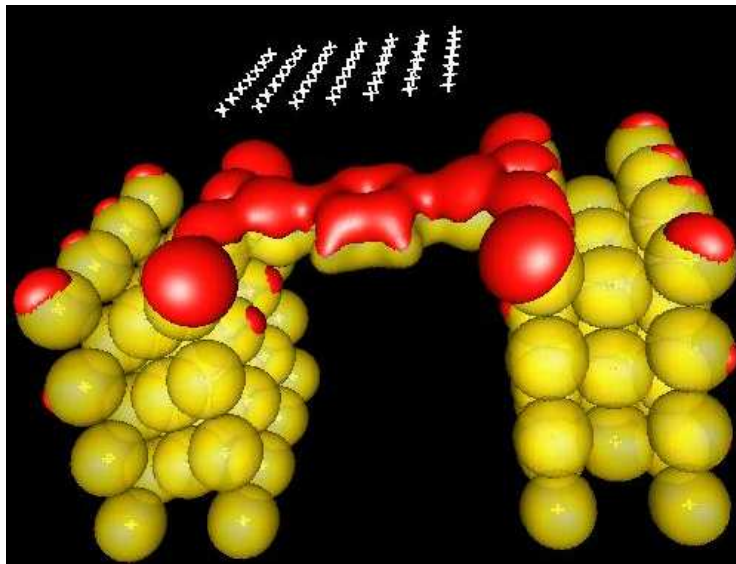
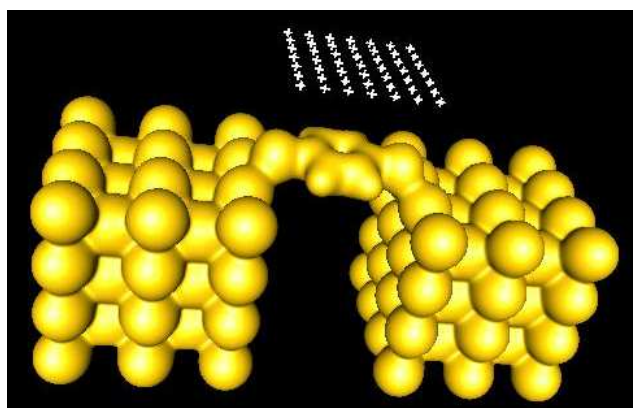


Figure 9.8: Screening of the gate charge by the gold electrodes. The additional screening charge pulled on the central cluster by the gate charge ( $+4e$ ) is depicted in red. Molecule and gold atoms are depicted in yellow. Electrodes consist of *fcc* blocks of 41 atoms, each.

For the chosen electrode geometry of *fcc* gold blocks, we tested several cluster sizes to ensure that finite size effects are minimized in our calculations. Fig. 9.8 shows the screening properties of a system where we have used clusters of 41 gold atoms each to model the coupling to the leads. The gate was charged with 4 positive elementary charges, whereas 4 electrons were added to the cluster. The spatial distribution of the additional screening charge compared to the ungated system is depicted in

red. It is clearly visible that most screening takes place in the row of gold atoms directly adjacent to the molecular bridge. But, at the outer row of gold atoms we still see some charge accumulation. Thus, a larger cluster size is necessary.

Using 66 gold atoms per side to form the clusters, consisting of three  $4 \times 4$  and two  $3 \times 3$  layers of gold, proved to be sufficient. Screening is done almost completely by the first three rows of gold atoms. The geometry used is depicted in fig. 9.9, with benzene-1,4-di-thiol as molecule in between the contacts.



*Figure 9.9: Actual geometry of the electrodes and the gate used for the DFT calculations. The electrodes consist of 66 gold atoms each, organized in an fcc block. Electrodes and molecule (benzene-1,4-di-thiol) are depicted in yellow, the point charges are denoted in white.*

- **Position of the molecule between the electrodes**

The position of the molecule with respect to the gate electrode as well as with respect to the gold contacts is of critical importance in determining the electrostatic field, the molecule is exposed to. In gold, the Thomas-Fermi screening length is of the order of  $1 \text{ \AA}$ , so that electrostatic fields created by a gate electrode above a narrow gap between two metal surfaces are usually screened within the first few atomic layers. Positioning the molecule between the gold electrodes will therefore result in only minimal exposure of the molecule to the applied gate field.

This poses a challenging problem to the experimental design as well. In break-junction experiments, for example, it will be unlikely that any gate effects can be observed, as the position of the molecule with respect to the electrodes prohibits exposure to the field: the terminal surfaces of the open break-junction are usually  $50$  by  $50 \text{ nm}$  large and the molecule-electrode bond forms at an uncontrolled position within this surface, so that fields will be effectively screened by the electrodes.

The experimental technique by van der Zant (see §9.1 above) allows to fabricate extremely thin electrodes and the gate distance to the electrodes is only about 2 nm. Due to the thin electrodes, chances are higher to find samples, where the molecule sits at the gate-directed end of the electrodes so that screening is minimized.

In our model setup, we placed the molecule at the topmost gold layer of the electrodes to minimize screening effects. To preserve the equilibrium bond angles between the sulfur and the gold (as discussed in §6.3), we had to place the molecule slightly above the electrodes. The equilibrium angles were obtained from DFT calculations, where the geometry was allowed to relax.

### 9.3 Results and discussion

As an exemplary case, we have studied the gate voltage dependence of the benzene molecule. In fig. 9.10 several transmission traces have been depicted each one corresponding to a different value of the gate charge,  $Q_G = 0, 2, 4$  electron charges. The most striking impact of the gate voltage on the transmission is, that it shifts the position of the resonance located at energies  $\sim 3$  eV above the Fermi energy (LUMO) to lower values. This is precisely the effect, expected based on the simple picture explicated in fig. 9.1.

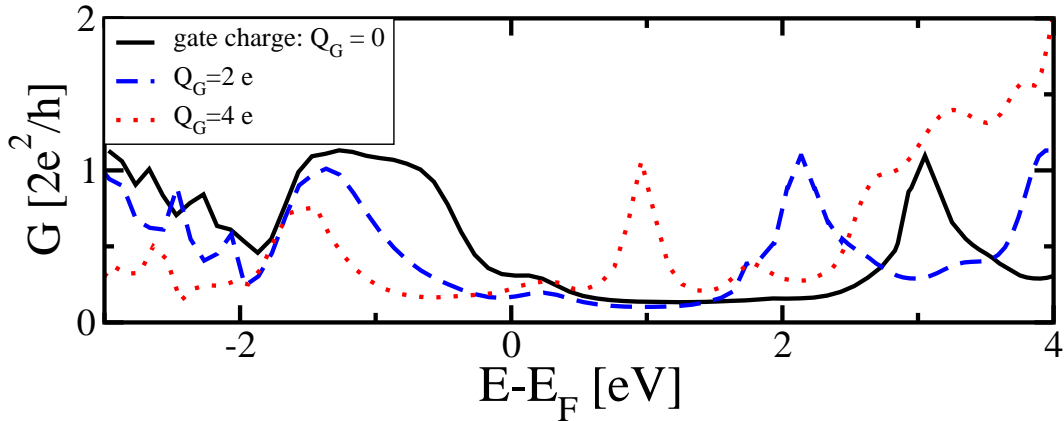


Figure 9.10: Benzene: impact of a gate charge on the transmission traces. Depicted is the transmission in  $2e^2/h$  over the energy. The different traces correspond to different gate charges:  $0e$  (solid black line),  $+2e$  (blue, dashed line), and  $+4e$  (red, dotted line).

The actual position of the resonance is tied to the spectrum of the unoccupied Kohn-Sham levels. Therefore, it is not physical and does not necessarily indi-

cate a true resonance observable in real experiments at that particular energy. However, when the gate voltage is swept, then this resonance approaches the Fermi energy. In our example this roughly happens when  $Q_G \geq 6$ . At the crossing of the LUMO with the Fermi energy, charge flows onto the molecule, which is a process that is detected properly by equilibrium DFT. Hence at the gate voltage, at which the crossing occurs, the true LUMO, the artificial Kohn-Sham LUMO and the Fermi energy must coincide. As a consequence, by monitoring the shift of the *Kohn-Sham* LUMO we can detect the exact positions of the spacings of the peaks in the Coulomb blockade oscillations.

Clearly, in practical calculations we are limited by the approximations in the exchange–correlation functional employed. The most serious defect for our present application is related to the “derivative discontinuity”, which is not properly accounted for in the standard functionals local in the density, like LDA or GGA. This implies, that we may be able to give a correct estimate for the peak position, but its broadening, i.e., at which value of  $Q_G$  the charge actually starts to flow onto the molecule and correspondingly at which value the flow really stops, could be vastly overestimated. Our encounter here with respect to the peak broadening is similar to the situation we have met before in the context of transmission resonances, see §7.1. As is the case for all DFT calculations for molecular systems, one needs to gauge the method using a test set of molecules investigated experimentally, in order to find out for which classes of molecular systems the corrections to the density functionals that are available in practice, become small. Therefore, DFT calculations for a molecule investigated experimentally by van der Zant [26] are under way.

It is also seen in fig. 9.10, that the gate has an impact on the transmission at energies below  $E_F$ , which is not properly described by a simple shift of energy levels. The situation here is more complicated, as the density of states in the electrodes (*d*-bands of gold) has pronounced structure at energies 1eV below  $E_F$ , cf. fig. 5.3. As a consequence, the molecular levels not only change their position, but also the way they hybridize with the gold when they are shifted. This does not happen in the case of the LUMO, because here, the density of states of the electrodes is nearly constant in the relevant energy window.



# Chapter 10

## Transport through a molecular double dot system

### 10.1 Motivation

In chapter 9, we have given an example on how to obtain quantitative information on transport from equilibrium DFT calculations. In the following chapter, we (ab-)use the underlying idea, applying it to a slightly different, but closely related problem: we calculate the position of steps in the non-linear I-V characteristics of a molecular double dot system.

Our specific choice of molecule used in this study has been motivated by recent experiments. The design of the molecular species in the experiment was directed towards fabrication of a single-molecule diode based on an asymmetric, functional molecule (see fig. 10.3). It will be seen, that a large number of steps observed in the experimental I-V characteristics can be reproduced *quantitatively* by our approach.

In this project, we have benefitted from a particularly intense collaboration with M. Mayor and M. Elbing (synthesis, INT) and H. Weber, R. Ochs (transport measurements, INT).

#### 10.1.1 The Aviram-Ratner diode

Historically, the field of molecular electronics started out from electron transfer physics and chemistry [155–157].

In the theoretical description of electron transfer physics, single electrons are transferred within a molecule from one orbital to another. Often these systems

are modeled as donor–acceptor systems. The electron is transferred from the electron–rich conjugated system that acts as a *donor* to a second conjugated unit, electron–poor, which constitutes the *acceptor*. The transfer occurs across non conjugated  $\sigma$ –bonds, that act as tunneling barrier.

In this spirit, Aviram and Ratner [4] proposed in 1974 a *Gedankenexperiment* to realize a diode by connecting such a donor–( $\sigma$ –bond)–acceptor system to metallic leads. The innovative aspect compared to electron transfer physics was, that the connection to the leads could support “a continuous sequence of electron transfer processes”, i.e., a stationary current.

For the setup suggested by Aviram and Ratner, the I–V characteristics of a rectifier was predicted. In short, the idea behind the “Aviram–Ratner approach” can be described as follows:

They suggested to use *electron pulling* substituents on one conjugated system to decrease the  $\pi$ –system electron density and construct the electron–poor acceptor, and likewise *electron pushing* substituents on the second conjugated system were suggested to construct the donor.

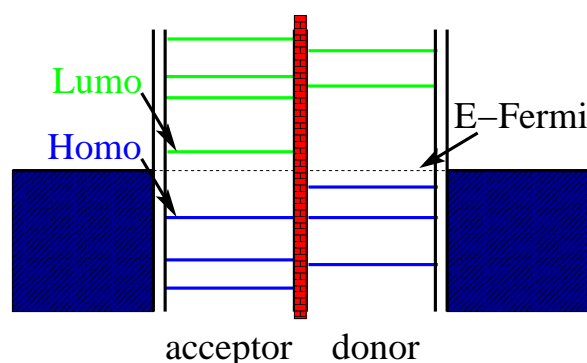


Figure 10.1: Aviram–Ratner diode: schematic representation of the electronic levels of the two conjugated systems, separated by a tunneling barrier. The left system acting as a donor and the right system as an acceptor. Occupied levels are depicted in blue, whereas unoccupied orbitals are printed in green. The Fermi energy is indicated as a dotted line.

The electron rich donor system will have a highest occupied molecular orbital (HOMO) higher in energy than that of the acceptor system. In the acceptor system, the lowest unoccupied molecular orbital (LUMO) will sit just slightly above the Fermi energy, whereas in the donor system the LUMO will be of higher energy, see fig. 10.1.

If we now apply a bias voltage, the levels of the two subsystems will move with respect to each other as depicted in fig. 10.2. On the left hand side, where we display the blocking direction of the molecule, a high bias voltage will be

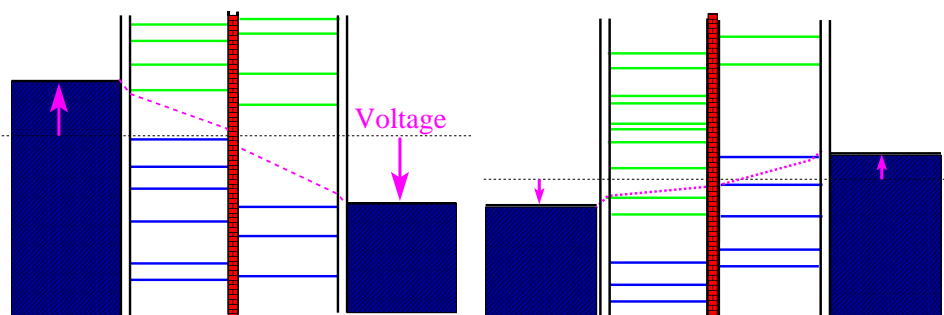


Figure 10.2: Aviram–Ratner diode: schematic representation of the electronic levels of the two conjugated systems under bias. Left: blocking direction. Right: transmitting direction. The bias voltage is depicted with magenta arrows. In the blocking case, a higher bias is required until levels align and transport becomes possible.

necessary before the first two levels align and transport is possible. When the bias sign is opposed, as depicted on the right, we need a much smaller bias voltage so that current starts to flow.

Thus, the predicted behavior of the molecular device is that of a diode<sup>1</sup>.

Note, that underlying this simple picture is a very strong assumption, namely that transport is governed mainly by the level sequence, i.e., the spectrum. The spatial structure of the wavefunctions, i.e., nontrivial properties of matrix elements, are ignored.

In fact, the molecule we will consider below is an example, where the Aviram–Ratner rule breaks down. We will see that the transport properties cannot be easily predicted by such simple assumptions. They crucially depend on the level structure and matrix elements and their evolution under bias.

### 10.1.2 Reasons for an asymmetric I–V characteristics

Any asymmetry in the I–V characteristics of a molecule is a consequence of a broken symmetry, which could be either a mirror plane, an inversion/rotational symmetry or some combination of these.

In theoretical calculations, in the framework explicated in chapter 3, asymmetries can be seen only, if one takes into account that the transmission depends

<sup>1</sup>It is assumed here, that sufficiently many inelastic decay channels exist so that an occupied molecular level can be evacuated even if the purely elastic, resonant channel is blocked.

on the voltage. This implies that any calculation based on linear response will be oblivious to such effect.

From the point of view presented in chapter 3, the voltage enters the transmission,  $T$ , in two places:

- The self-energies  $\Sigma(E + \delta\mu^{l,r})$

The density of states of the leads may be non-constant and thus different for left and right lead at finite bias voltage  $V$ , where the chemical potentials,  $\mu_{l,r}$  of the respective leads differ from their equilibrium values by  $\delta\mu_{l,r}$ , with  $\delta\mu_l - \delta\mu_r = V$ . This results in bias dependent self-energies.

- The Green's-function of the *extended molecule*

Spectrum and wavefunctions of the extended molecule need to be calculated in the presence of a finite current. The feedback of the current into wavefunction and spectrum is due to an induced shift of the molecular charge that does not directly participate in the current flow. We will refer to this as polarization induced effects.

### Examples of situations leading to asymmetric I-Vs:

#### Asymmetric molecules

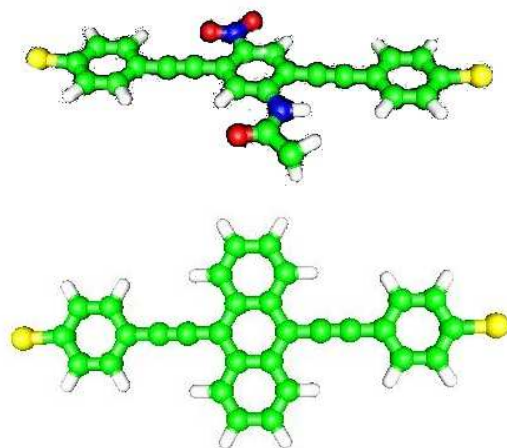


Figure 10.3: Asymmetric molecule (top) and symmetric anthracene type molecule (bottom) of section §6.2.

Asymmetric molecules show asymmetric I-V characteristics because their polarizability will be bias-dependent. One example are molecules with permanent electrical dipole moment: in chapter 6 we have studied a symmetric,

anthracene type molecule, for which symmetric I–V curves were observed. To investigate asymmetries due to the polarizability of molecules, a second, asymmetric molecule of comparable size and structure was synthesized at our institute by M. Elbing and M. Mayor, see fig. 10.3.

Instead of the anthracene, a benzene ring with two differing side–groups was used as the central element. On one side,  $NO_2$  is used as a substituent, which is known as a group with high electron affinity. This should pull electrons from the central benzene ring. On the other side, an acetyl–protected amide group was used, which is supposed to inject electrons in the  $\pi$ –system of the central ring.

This asymmetric charge distribution then leads to a *permanent dipole moment* with a component parallel to the molecular axis (the axis defined by the two terminal sulfurs). Due to this asymmetry and the resulting permanent dipole moment, we can expect the molecule to have an asymmetric polarizability under applied bias. Depending on the bias sign, the Kohn–Sham levels thus could evolve differently, resulting in an asymmetric I–V characteristics.

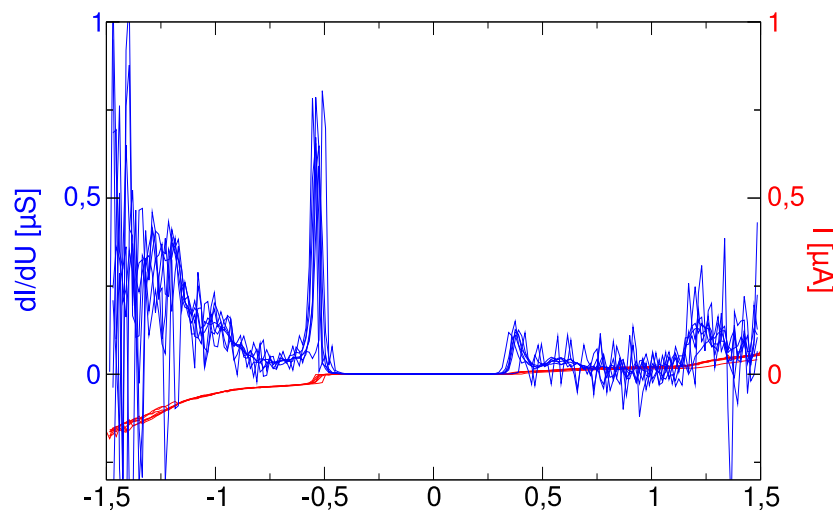


Figure 10.4: I–V characteristics of the asymmetric molecule depicted in fig. 10.3, top, at about 30 K. Red: current over applied bias voltage in  $\mu A$ . Blue: differential conductance in  $\mu S$ . Different traces correspond to consecutive voltage sweeps, [153].

In fig. 10.4, the experimental data for the conductance of the asymmetric molecules is presented. The strong asymmetry is obvious: for negative bias, we

observe a strong peak in the differential conductance at about  $0.5 V$ , whereas in the positive bias case only small peaks can be observed.

To investigate the origin of this asymmetry, we performed DFT calculations of the molecule between pyramids of 29 gold atoms. In the linear response regime, where calculations are done with no external bias voltage applied, we can not observe an asymmetry. But doing calculations under a finite applied bias voltage of  $1 V$  can lead to polarization of the molecule resulting in asymmetric transport characteristics. The calculation was done by supplying a constant external electrical field, that corresponds to a voltage drop of  $1 V$  over the length of the molecule, in the DFT run.

The amount of 29 gold atoms per contact to include into the extended cluster is too small to do a transport calculation, but we can look at the evolution of the electron density under bias. We will only give an illustration of the influence of the external field on the charge distribution. Further analysis is in progress.

In fig. 10.5, we depict the polarization of the molecule when an external field from right to left, corresponding to  $1 V$  bias voltage, is applied. Fig. 10.6 corresponds to the opposite situation, where the field is directed to the right. In both cases, the additional charge accumulated in comparison to the zero-bias case is depicted in red, whereas the charge deficit is drawn in blue.

The polarizability of the molecule is clearly asymmetric: in the positive bias situation (fig. 10.6), on the central ring plus the substituents, additional charge accumulates, whereas in the negative bias situation (fig. 10.5), a charge deficit is observed. In both cases, charges accumulate on the left ring, although to different extent. Due to the asymmetric polarizability, we expect the I-V to be asymmetric.

Although these two figures provide a large amount of detailed information, it is not straightforward how to extract from it which direction under bias is better conducting. In order to address this question, calculations using our “standard approach” to transport, but with input wavefunctions and orbitals from the finite bias DFT calculations could be used. These calculations are in the works.

As a check, we also conducted calculations for applied external fields in the case of the the symmetric molecule of fig. 10.3. There, as expected, our calculations showed symmetric polarizability for the two bias directions.

A second example of a molecular asymmetry leading to asymmetric I-V characteristics are strongly asymmetric designs in the spatial molecular structure:

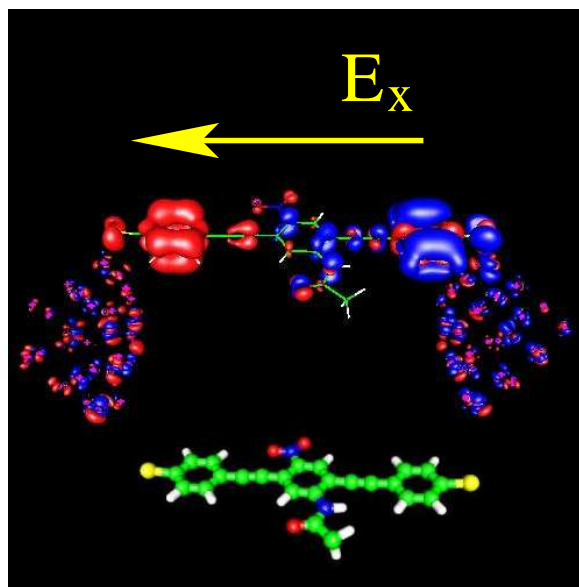


Figure 10.5: Polarizability of the asymmetric molecule: depicted is the electron density difference for an applied external electric field (arrow) corresponding to  $-1\text{ V}$  bias voltage. Red: charge accumulation relative to zero voltage case, blue: charge deficit. For illustration, the structure of the asymmetric molecule is depicted at the bottom

A molecule consisting of a central conjugated group, sandwiched between two insulating molecular subunits of different lengths, results in a molecular quantum dot with strongly asymmetric coupling. This is due to the spatially asymmetric placement of the resonant system closer to one of the electrodes [158]. The voltage drop will occur mainly at the side with the larger insulating group, resulting in different resonance conditions for the dot depending on the bias sign.

### Symmetric molecules with asymmetric coupling to the electrodes

An asymmetry in the I-V characteristics can be induced even for symmetric molecules, by asymmetric coupling to the two metallic leads.

In fact, in STM experiments the coupling is extremely asymmetric. There, only one of the two ends of the molecule is usually covalently bonded to the electrode, i.e., the substrate. The other electrode, i.e., the STM tip, only constitutes a tunneling contact. In this setup, the Fermi energy of the molecule is pinned to the electrode it is covalently bonded to. Therefore, sweeping the applied voltage will scan different molecular orbitals depending on the sign of the bias. Thus,

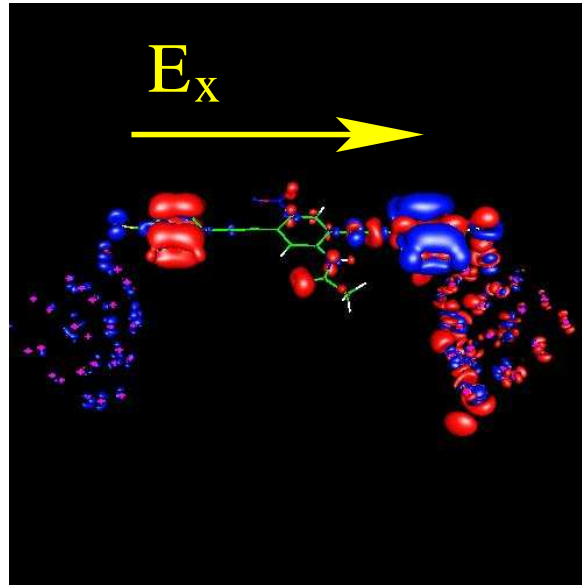


Figure 10.6: Polarizability of the asymmetric molecule: depicted is the electron density difference for an applied external electric field (arrow) corresponding to +1 V bias voltage. Red: charge accumulation relative to zero voltage case, blue: charge deficit.

observed I–Vs are asymmetric, independent of the symmetry properties of the molecule.

Asymmetries are usually present in all experimental setups, including break-junction experiments. But there, due to the defined covalent bond of the sulfur to the gold, the asymmetry is much smaller than in the STM setup, leading to asymmetries of typically only a factor of two in the I–V characteristics in most cases (see also §6.3).

Different electron affinities of the coupling groups to the electrodes can lead to a coupling induced polarization even without applied bias. This is, because these asymmetries will result in bias dependent molecular level evolution and, thereby asymmetric I–V characteristics [11, 159, 160].

## 10.2 Molecular double quantum dot system

In this section, we will give a detailed study of an example of asymmetric current–voltage characteristics for a system that has no permanent dipole moment.

### 10.2.1 Design of the molecule

Experimentally, donor- $\sigma$ -acceptor systems have been built using Langmuir-Blodgett films in between two planar electrodes (see e.g., [161]) or using self-assembled monolayers in STM experiments [38].

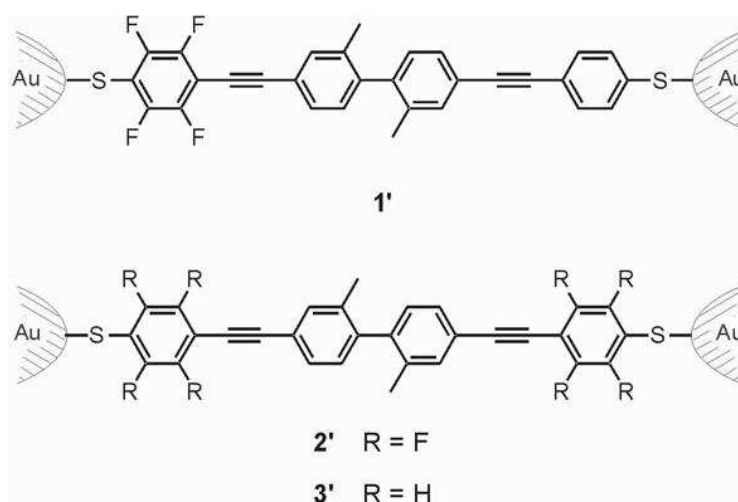


Figure 10.7: Diode molecule and control molecules covalently coupled to gold electrodes, schematic representation. **1'**: diode molecule, where on the left benzene ring, the hydrogen was substituted by fluor. **2'**, **3'**: control molecules. Either both sides (**2'**: R=F) have fluor substitutions on the outer benzene rings, or both outer benzene rings have hydrogen atoms (**3'**: R=H), [1].

Following the *Gedankenexperiment* of Aviram and Ratner, a donor- $\sigma$ -acceptor molecule was designed and synthesized by M. Elbing and M. Mayor. In order to make measurements using the break junction technique possible, the molecule has to have a linear, rigid rod like structure. For connection to the leads, it is terminated on both sides with acetyl protected sulfur groups (as has been discussed in section §6.4). The diode molecule is depicted in fig. 10.7, labeled with **1'**.

The intended electronic asymmetry is achieved by partitioning the molecular rod into two separated  $\pi$ -segments of comparable structural features but different donor/acceptor properties. It is crucial to keep both  $\pi$ -systems as similar as possible in size, building blocks and anchor groups, to ensure that effects on the electronic transparency of the molecule mainly stem from the electronic level evolution under bias of both subsystems. This way, effects from structural asymmetries are minimized.

One of the outer rings was functionalized with four electron-deficient fluorine atoms to produce a  $\pi$ -system with comparable structural properties but significantly different electronic properties.

Instead of using a stiff linker of  $\sigma$ -bond character, as suggested originally by Aviram and Ratner [4], both  $\pi$ -systems (consisting of two benzene rings, each) were linked by a single C—C bond. Methyl side-groups in *ortho* position to the C—C bond were added to the inner benzene rings. This way, steric repulsion induces a large torsion angle between the two conjugated subunits, thereby minimizing the overlap of the  $\pi$ -orbitals and hence the coupling. Thus, a donor- $\sigma$ -acceptor system is realized.

Our DFT calculations, where we allowed the structure of the molecule to relax, as well as X-ray crystallography data confirm, that the two subunits are at an angle close to 75 degrees. Thus, differing from the original design, the molecules are separated by a *torsion induced tunneling barrier* provided by side groups.

The modular strategy of synthesizing the molecule from their subunits made it possible to also produce two control molecules, depicted in fig. 10.7. These were either fluorized on both outer rings, (**2'**), or on none, (**3'**). They can not only be used for control experiments, but also might offer interesting insights into the influence of charging of the molecule on its conductance properties.

## 10.2.2 Experimental results

Extensive conductance measurements of the *diode molecule* (**1'**) and the two control molecules (**2'**, **3'**) were conducted by R. Ochs and H. Weber [1]. In fig. 10.8, we present the data for the I-V characteristics of the diode. The experiments were performed at low temperature,  $T \approx 30K$ , stable I-V curves were observed repeatedly.

Molecule **1'** shows clearly asymmetric I-V properties: for negative bias voltages the current is much smaller than at the corresponding positive values. A comparison of the current level at  $U = \pm 1.5V$  yields a “rectification ratio” of 1:4.5.

The current increases in a step-like behavior which is more pronounced for positive bias, but also present at negative bias voltages.

Counting all stable contacts (i.e., contacts where I-Vs could be consecutively recorded more than 5 times) 20 I-Vs were obtained. In these measurements, the rectification ratio, again evaluated at  $U = \pm 1.5V$ , varied from 1.4 to 10, with an average rectification ratio of 3.6. This shows clearly, that molecule **1'** exhibits asymmetric conductance properties.

For comparison, data for the control molecules **2'** and **3'** is depicted in fig. 10.9. In both cases, more symmetric I-Vs were recorded for all measurements. For

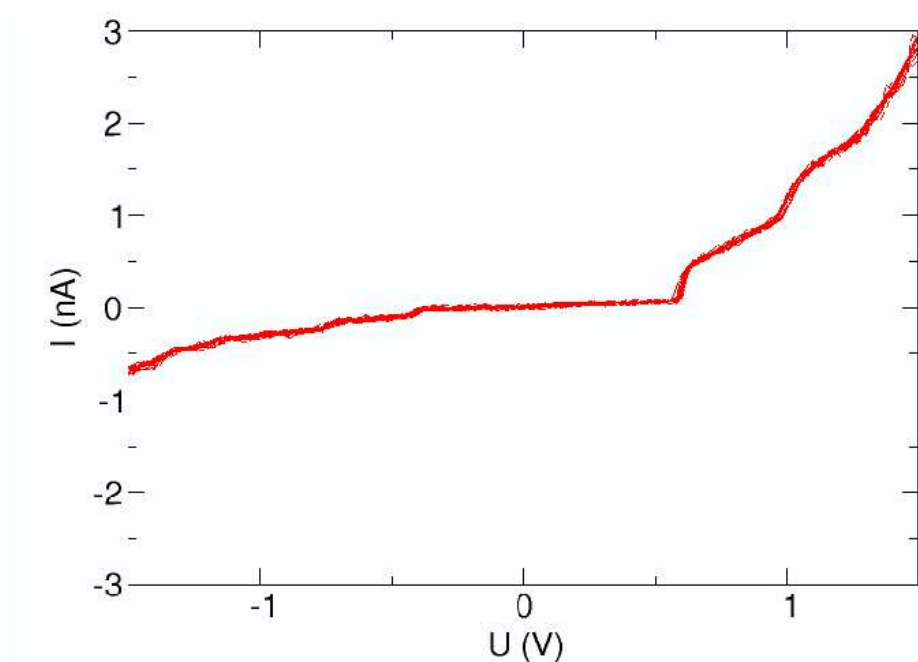


Figure 10.8:  $I$ - $V$  characteristics of the diode molecule **1'**, depicted in fig. 10.7. Red: current [nA] over applied bias voltage, [1].

molecule **2'**, fluorized on both ends, 40 measurements were taken. In the case of control molecule **3'**, 16 curves could be obtained. In all measurements the rectification ratios, again evaluated at  $U = \pm 1.5 V$ , were close to one, taking values between 1 and 1.8.

There is a clear qualitative difference between the diode molecule and the other ones adding further evidence that the asymmetric  $I$ - $V$ s, obtained for molecule **1'**, stem from the asymmetric design of the molecule and are not artefacts from asymmetric coupling or other environmental influences.

In their original paper, Aviram and Ratner predicted “true” diode like behavior for their molecule, due to a current onset occurring at significantly different voltages depending on the sign of the bias. Rectification for our molecule stems from the significantly different slope in the  $I$ - $V$  characteristics at different bias signs rather than from a difference in the current onset, which depends only weakly on the bias sign. Thus, the experimental data suggests a different process underlying the rectification in this case.

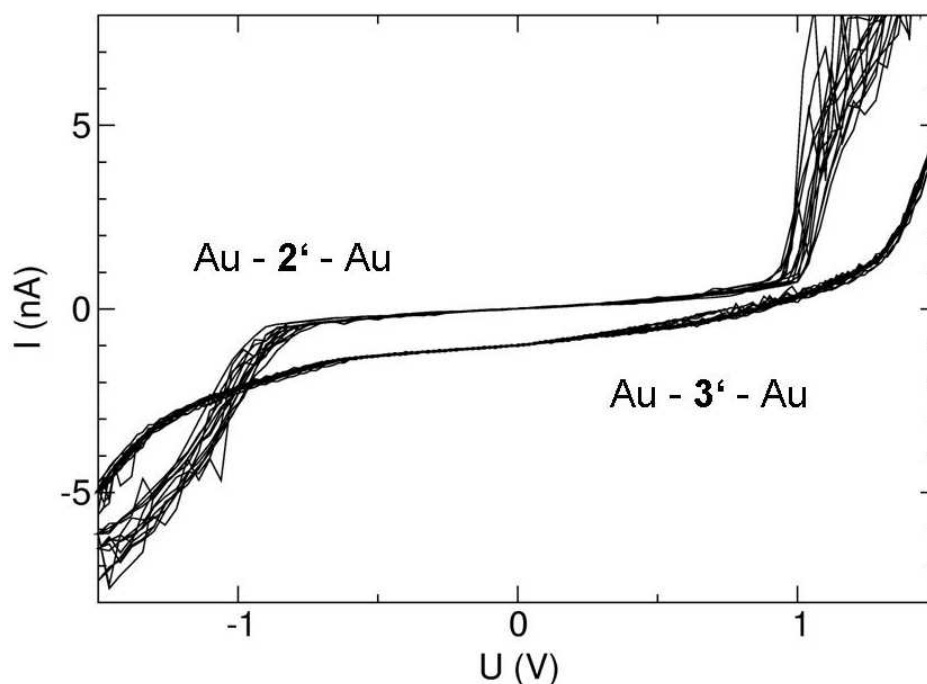


Figure 10.9:  $I$ - $V$  characteristics of the control molecules **2'**, **3'**, depicted in fig. 10.7. Relatively symmetric  $I$ - $V$ s were recorded. Different traces correspond to consecutive voltage sweeps, [1].

### 10.2.3 Double dot system: principle mechanism

In this section, we offer a qualitative explanation of the relevant underlying transport mechanism, and how it manifests itself in the experimental observations.

By design, the set-up (gold electrode)—(diode molecule)—(gold electrode) with its two separated electronic  $\pi$ -systems may be viewed as two quantum dots coupled in series. We will refer to them as the  $F$ -dot (fluorized dot), and  $H$ -dot (not fluorized dot/ hydrogen dot) as depicted in fig. 10.10.

As the two  $\pi$ -systems are only very weakly overlapping, the conductance of the molecule is low. For this reason, transport is likely to be incoherent and transmission calculations using the scattering approach will not yield the dominating contribution to the current. However, we will see that a DFT study can nevertheless deliver *quantitative* results for the structure of the  $I$ - $V$  curves. Let us outline now, how this can be achieved.

Our DFT calculations show that the electronic orbitals are indeed localized on either one of the dots, confirming the notion of two separate conjugated

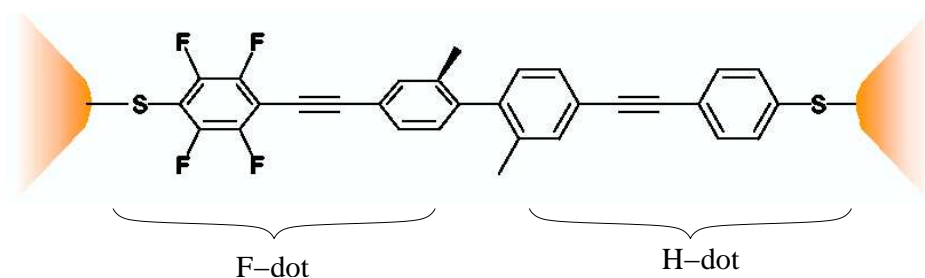


Figure 10.10: Schematic view of the diode molecule in between gold contacts. The system can be modeled as two quantum dots separated by a tunneling barrier, caused by the torsion of the two subsystems.

subsystems. In Fig. 10.11 we show the lowest unoccupied molecular orbital (LUMO) of both subunits obtained from the DFT calculations.

At zero bias, the states of both subsystems are occupied up to the HOMO, see fig. 10.12. Due to the modification of the electronic structure of the F-dot by the substitution of fluorine atoms for the hydrogen, the level positions of both subunits differ from each other. The new level sequence is such, that the F-dot acts as the acceptor, the H-dot as the donor system (see §10.1.1).

The zero-bias conductance is suppressed, since resonant transport is blocked. When the bias voltage is swept, the levels of both dots are shifted with respect to one another and at certain voltages two levels will cross. E.g., for positive bias applied on the right-hand side, the highest occupied level (HOMO) of the H-dot will move upward and align with the downward moving lowest unoccupied molecular orbital (LUMO) of the F-dot. Thus, a transport channel will open up for inelastic transmission of electrons from the F-dot to the H-dot and from there into the right lead.

As transport by assumption is inelastic, the channel will remain open when the bias is further increased, resulting in a step in the I-V characteristics, as depicted in fig. 10.13. Every time the occupied level of the H-dot passes by an unoccupied level of the F-dot, an additional transport channel opens up for inelastic transmission and the current will increase by a certain amount, resulting in a new step in the I-V.

In the blocking direction, depicted in fig. 10.14, less level crossings are observed when the bias voltage is swept, resulting in fewer, larger spaced steps in the I-V characteristics.

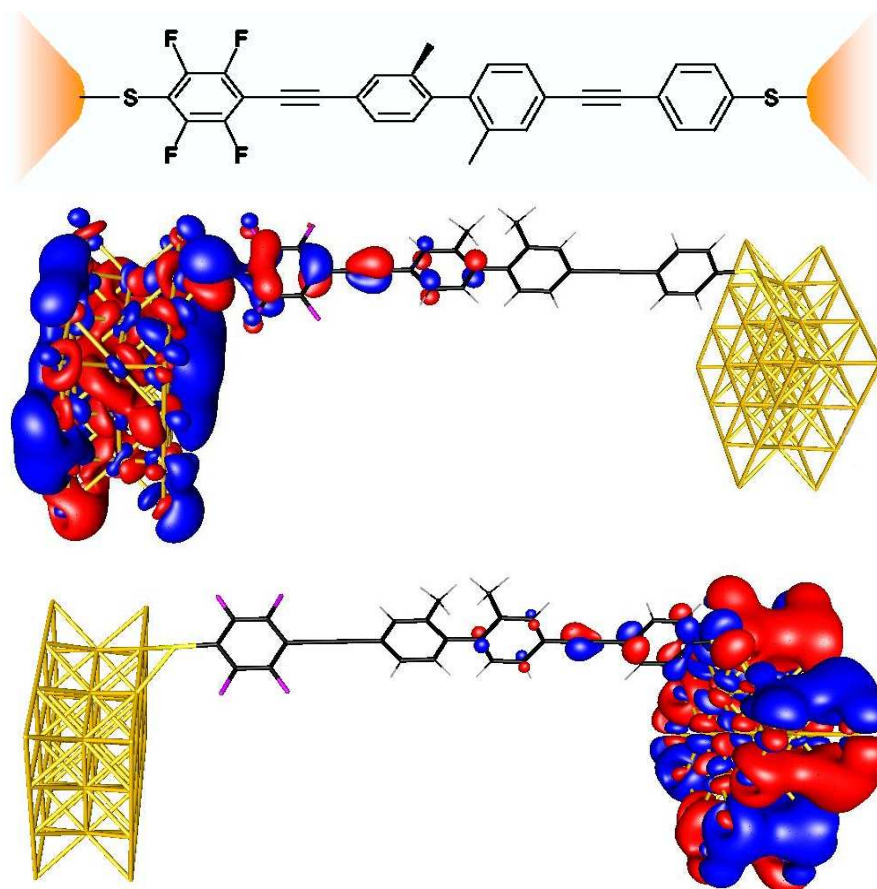


Figure 10.11: Lowest unoccupied molecular orbitals (LUMO) of the fluorized (F-dot, center) and the unfluorized (H-dot, bottom) sections of the diode molecule attached to gold leads. DFT calculation. The gold atoms included in the DFT run are depicted by a golden lattice. For orientation, the molecular structure is depicted at the top. Different colors of the orbitals visualize the sign of the wavefunctions.

#### 10.2.4 Evolution of the Kohn–Sham levels

In order to support the qualitative analysis given above, we have carried out extensive DFT calculations of the diode molecule. The electrodes were modeled by including two gold blocks of 41 atoms each in the DFT calculation of the molecule, see fig. 10.11.

Since the conductance of the molecules is very small, we performed the DFT–calculation in a constant external electric field. The TURBOMOLE iteration cycle was stopped, when a local equilibrium on either side of the system, i.e., the F-dot or the H-dot plus the associated leads, was reached.

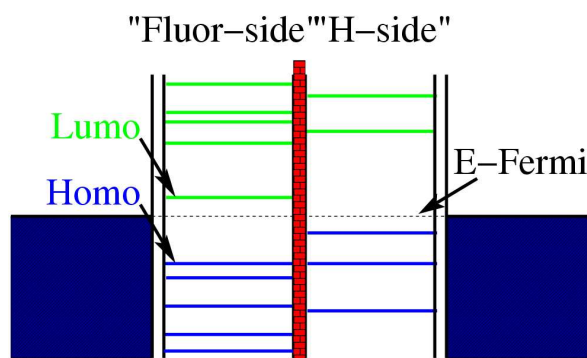


Figure 10.12: Schematic of the level structure for the molecular double dot at zero bias. Left dot: fluoridized benzene ring. Right dot: benzene ring with hydrogen.

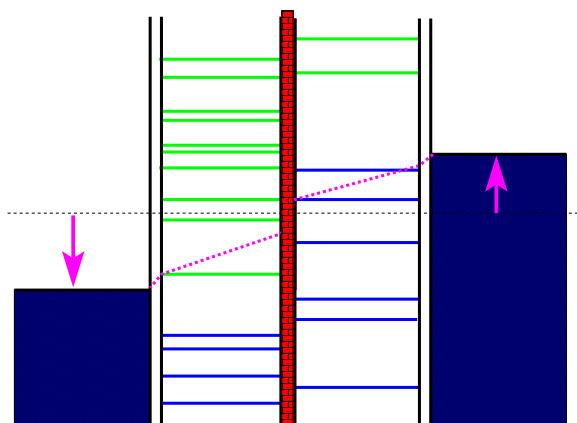


Figure 10.13: Schematic of the level structure, transmitting direction. A new transport channel is opened in the molecular double dot when the levels align. Left dot: fluoridized benzene ring. Right dot: benzene ring with hydrogen. In this situation, several channels can contribute to the current.

The structure of the molecule was relaxed in a zero field run. We know from other DFT calculations done by us, that the influence of the applied field along the molecular axis is small and can be neglected, so relaxation was not to be repeated at finite voltage. But it could be done, of course.

By studying the evolution of the single-particle Kohn-Sham energies with the applied voltage, we can obtain quantitative information on the transport characteristics. Applying a bias voltage to the system will shift the Kohn-Sham energy levels of the subsystems. Due to the fluoridation of the *F-dot*, the two subsystems are of different electronic structure. Thus the level evolution will be different for the two sides.

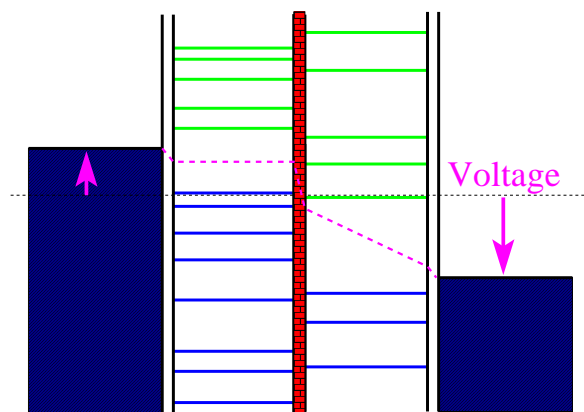


Figure 10.14: Schematic of the level structure for the molecular double dot in blocking direction. Left dot: fluoridized benzene ring. Right dot: benzene ring with hydrogen. Only two levels are available for transport in the right dot within the voltage window opened by the applied bias, depicted in magenta.

This evolution is entirely dominated by electrostatic effects and therefore can be studied appropriately within the standard framework of equilibrium DFT. For the same reason, the level flow is expected to exhibit linear behavior in the applied voltage to an excellent approximation, as long as the voltages are not too large.

We could obtain the Kohn–Sham orbitals for three bias voltage values:  $U = -0.1\text{ V}$ ,  $U = 0.08\text{ V}$ , and for zero bias. All orbitals within the energy window of interest (a few eV around the Fermi level) were plotted and characterized according to their symmetry and localization on a specific dot. This way, we were able to match the levels of the calculations for different bias voltages with each other and thus determine their evolution under bias. In figure 10.15 we depict the level evolution for the diode molecule under bias. Shown are the position of the occupied levels close to the Fermi energy together with the lowest unoccupied ones for the three voltages. With dotted (*F-dot*) and dashed (*H-dot*) lines we display the linear extrapolation to larger biases.

The slope with which the levels evolve under bias is an indicator for the polarizability of the electron system of either dot. A small slope signals the screening of the applied bias and points to a rather *metallic* character of the dot. Higher slopes correspond to more insulating properties.

The slope for the H-dot levels ( $\square$ ) is larger than the slope for the F-dot levels ( $\circ$ ) due to less screening of the applied electrical field, presumably because there are less electrons available to do the screening. This thus implies a more insulating behavior of the H-dot.

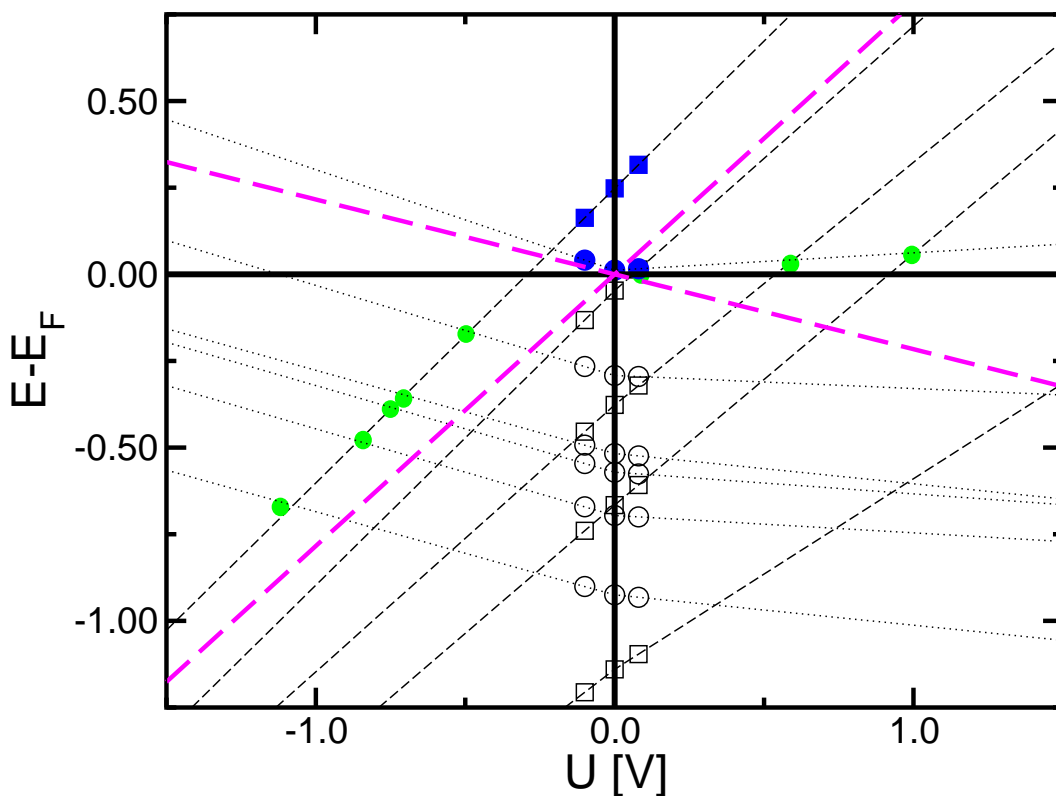


Figure 10.15: Diode molecule: Analysis of the evolution of the Kohn–Sham energy levels corresponding to the fluorized (F-dot,  $\circ$ ) and unfluorized (H-dot,  $\square$ ) sections of the molecule when applying a gate voltage ( $-0.1$  V,  $0$  V, and  $0.08$  V). The lowest unoccupied molecular orbitals (LUMO) are depicted as filled symbols. Using dotted (F-dot), and dashed (H-dot) lines, we show the linear extrapolation of the level flow to higher bias voltages. The voltage window, within which level crossings can be observed experimentally ( $\bullet$ ) is indicated by the dashed, magenta lines.

Experimental data for the control molecules **2'** and **3'** are consistent with this deduction: the zero bias conductance of the Au—**2'**—Au bridge, consisting of two F-dots, is considerably higher than that of the Au—**3'**—Au bridge which contains two H-dots (see fig. 10.9).

The evolution of the H-dot levels is almost bias sign independent, suggesting a symmetric polarizability of the H-dot. In the case of the F-dot, we observe a significant difference in the slope depending on the bias sign, pointing to an asymmetric polarizability of the F-dot.

### 10.2.5 Peak positions in the I–V characteristics

Let us now turn to the quantitative analysis of the peak position in the I–V characteristics of the diode molecule, presented in fig. 10.8, above. As explained previously, we expect a new channel to open, each time an occupied level of the upward moving dot crosses an unoccupied level of the downward moving dot.

In fig. 10.15 we marked the voltage window, which indicates those level crossings that can be observable experimentally. This window is defined by the shift of the chemical potentials of the two leads with the bias voltage. It is obtained from the evolution of those states of the extended molecule, that are exclusively localized on one of the gold clusters. Depicted in green are the level crossings inside the voltage window where we would expect to observe peaks in the measured differential conductance.

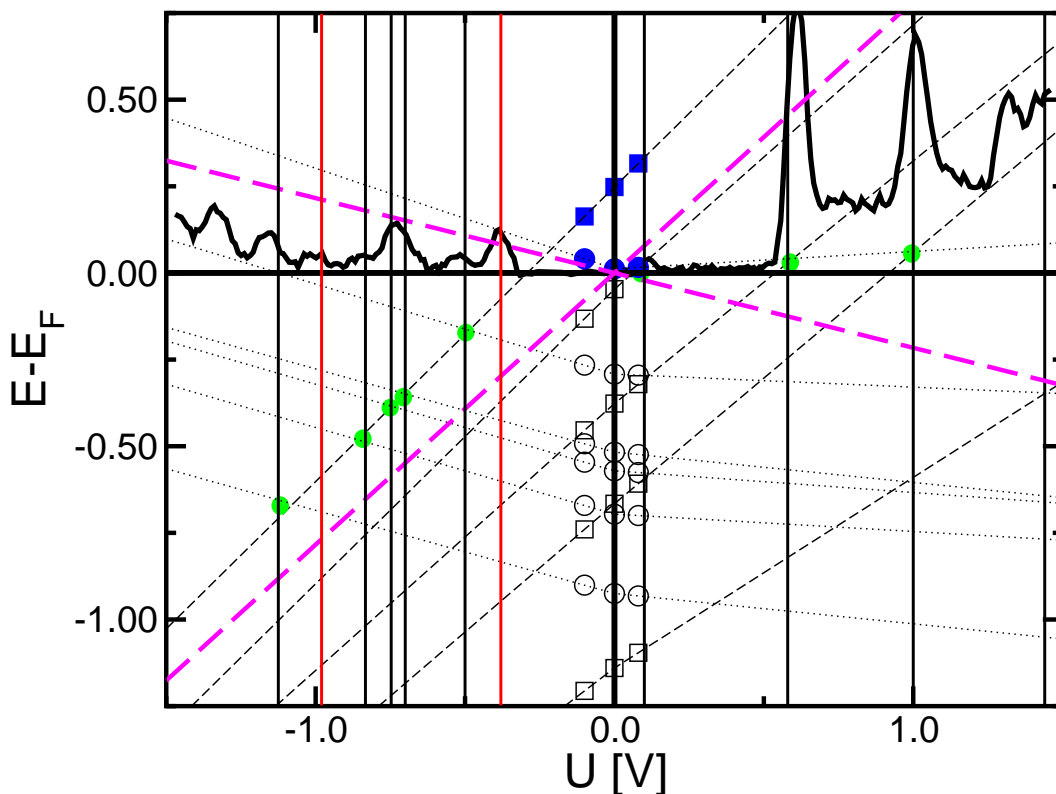


Figure 10.16: Diode molecule: analysis of the peak positions in the I–V characteristics. Plot similar to fig. 10.15, but now with the experimental differential conductance plotted in black. For easier comparison with the theoretical data, vertical lines are inserted at the theoretical peak positions.

This now has to be compared with the experimental differential conductance data for the diode molecule (i.e., the  $dI/dV$  of fig. 10.8), which we do in the next plot, fig. 10.16. There, the experimental data is plotted as a black curve. To make the comparison with the experimental data easier, we inserted vertical, black lines at the expected peak positions.

We find that our calculation gives a proper quantitative account of seven out of the nine lowest lying peaks. Deviations in peak positions are not larger than the experimental peak width. Only two peaks seen in the experiment are missing in our theoretical prediction. These are shown as red lines in the graph. Indeed, all peaks predicted theoretically are also observed in experiment. The fourth peak on the positive bias side lies narrowly outside the voltage window. With a slightly different slope for the level evolution of the lowest orbital considered, it would fall in place, explaining the peak position.

Three more, nontrivial experimental observations find a natural explanation in our proposed scenario:

First, in the experimental data the number of peaks in the differential conductance is larger for the branch of the I–V curve that exhibits the lower conductance (negative bias in fig. 10.8).

The number of peaks can directly be attributed to the number of level crossings. In the positive bias case, these are governed by the HOMO of the H–dot crossing the unoccupied levels of the F–dot. These are more numerous than in the H–dot case, due to the larger amount of electrons contributed by the fluorine atoms, as seen above in the discussion of the subsystems. In the negative bias case, the HOMO of the F–dot crosses the fewer unoccupied levels of the H–dot, resulting in a smaller number of peaks in the differential conductance.

Second, despite the larger number of transmitting channels in the negative branch of the I–V curve, the total current is significantly smaller than in the positive bias case. The diode acts opposite to what one might have guessed, perhaps.

To solve this puzzle, we have to consider the polarizability of the subsystems: while the slopes of the H–dot levels are more or less bias sign independent, the slopes of the F–dot levels are in general larger at negative bias, suggesting an asymmetric polarizability of the double dot system. In similarity to a p–n–junction, the current is larger in the direction, where the dot exhibits a larger polarizability. In other words, differently polarized electron systems result in different transmissions and thus we can observe a larger current in the positive bias direction even though there are fewer, and larger spaced peaks in the differential conductance.

Third, let us comment on the applicability of the Aviram–Ratner scenario to the present case. The peak appearing at the lowest bias voltage indeed is found in the forward bias sector, at voltages  $V \approx 0.1 V$ , see fig. 10.18. The corresponding transport channel gives the dominant contribution to the current only until the second channel opens up at  $V \approx 0.6 V$ , which then becomes the overwhelming one. The main features of the experimental curve in the voltage window up to  $\pm 1 V$  stem from the characteristics of these higher channels which is due to polarization physics not contained in the Aviram–Ratner picture.

### 10.2.6 Discussion

The excellent quantitative agreement between our theoretical calculations and the experimental data concerning the peak positions could not be anticipated a priori:

Taking into account the deficiencies in the GGA exchange–correlation functional used in the DFT calculations, as well as our approximation to use the equilibrium functional neglecting the current through the system, one would expect slight deviations of the peak positions. Our data seems to suggest, that these approximation induced changes in the level flow with applied bias could be quite small in the present case, so that this approximation made is justified here.

Further deviations between experiment and theory could be expected from variations in the microscopies of the molecular contacts, as we did investigate in chapter 6: there are several parameters in the contact and its environment, that cannot be controlled and may therefore vary from sample to sample:

- The spatial orientation of the molecule is uncontrolled, it might not sit in the idealized situation as depicted in fig. 10.7, resulting in stress on the bonding geometry which can influence the transmission characteristics (see §6.3).
- Different bonding types of the S–Au bond can shift the transmission characteristics (see §6.4).
- The environment might provide background charges in form of other diode molecules or water present. These can effectively *dope* the molecule, resulting in a shift of the peaks.

Indeed, when the measurement is repeated after either opening and reclosing the molecular bridge to form a new contact, or by using an entirely new

break-junction, the experimental curves look qualitatively similar, but differ nevertheless quantitatively.

Many different I–V curves were recorded, unfortunately most of them did exhibit less pronounced peaks, making a direct comparison with our theoretical data more difficult. Our choice of curve was motivated by the fact, that it offered the most pronounced and stable peak structure to facilitate clear comparison between theory and experiment.

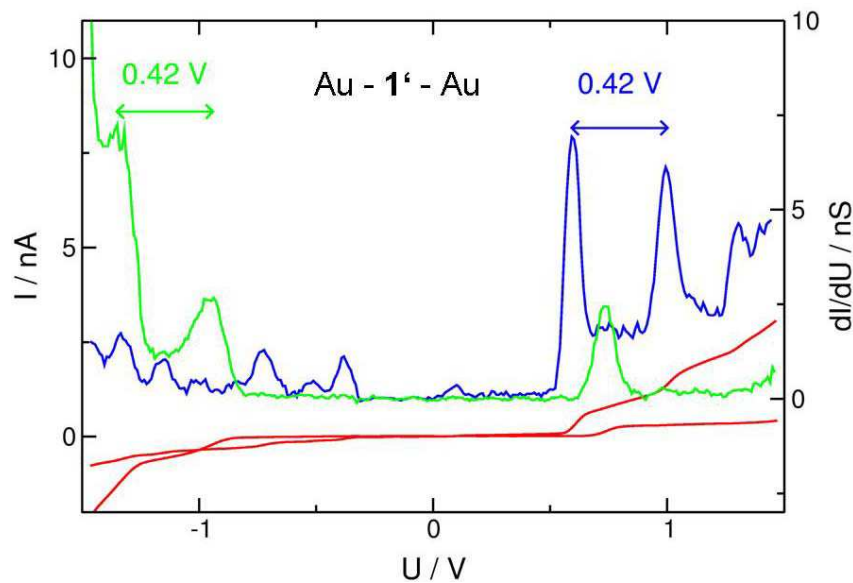


Figure 10.17: Diode molecule: Comparison of the I–V characteristics of two different samples. Red: current over bias voltage. Green: differential conductance. The  $dI/dV$  of the sample from fig. 10.8 above is depicted in blue, [1].

For an illustration of these sample to sample variations, we show in fig. 10.17 data for a second set of I–V (red) together with the one discussed above. The differential conductance is depicted in green.

Evidently, the new curve is inverted with respect to the bias direction, likely because the molecule is oppositely oriented. In contrast to the curve discussed above, it only offers few (three) pronounced peaks. In addition, the peaks and thus the current steps have different heights and are observed at slightly different voltage values. Note however, that the spacing between the peaks in the forward direction is quite similar in both measurements, which is why we believe that both traces stem from the same molecule exposed to different environments.

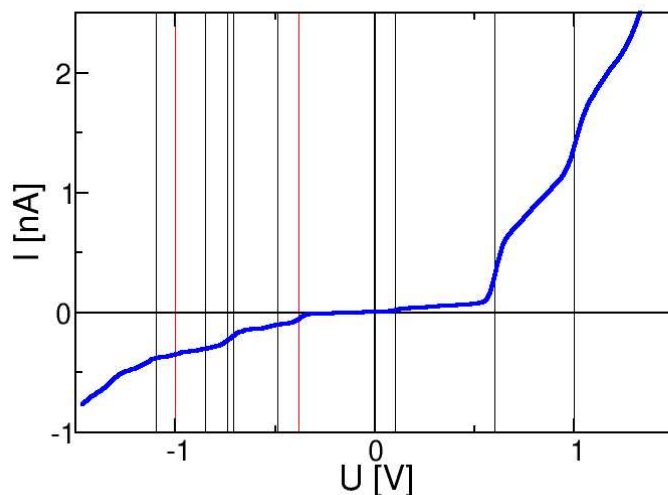


Figure 10.18: Diode molecule of fig. 10.10: measured current–voltage characteristics (blue curve) and theoretically predicted step positions (black vertical lines). The molecule behaves as a coupled double quantum dot in series. States are localized on the subsystems (H–dot, F–dot). When a bias voltage is applied, the positions of the levels of the two subsystems move with respect to each other. At level crossings, a step in the  $I$ – $V$  characteristics is observed. We predicted the position of seven out of the nine lowest lying peaks in the differential conductance. Missing peaks are depicted by red lines.

### 10.2.7 Summary

We have identified the fingerprint of a molecule in a transport measurement for the first time. Thereby, we predicted the position of seven out of the nine lowest lying peaks in the differential conductance, see fig. 10.18.

The relevant transport mechanisms were identified, and a new method was suggested to calculate the transport properties: using DFT calculations in a finite external electric field, we were able to extract the evolution of the Kohn–Sham orbitals under bias. From this, we obtained the positions of the peaks in the differential conductance, which are in quantitative agreement with the experiment.

We have seen that physics beyond the Aviram–Ratner picture—polarization and the evolution of the matrix elements under bias—gives the dominant contributions to the  $I$ – $V$  characteristics in this case.

# Chapter 11

## Conclusions

### 11.1 Summary

This work is motivated by the strong impact that first principles based calculations are likely to have in the emerging field of molecular electronics. At the moment, one of the most pressing problems in this context is the fact, that the current theoretical predictions of the transmission of a molecule exceed the experimentally measured one by much more than one order of magnitude.

As a first step in our work we have implemented the “standard” approach to the molecular conductance, namely transport calculations in a Landauer–Büttiker framework based on Kohn–Sham orbitals extracted from density functional theory (DFT) calculations. Our particular implementation ensures, that apart from approximations inherent in the exchange–correlation functional of DFT no further approximations are made. In particular, we can include sufficiently many contact atoms to ensure a reliable extrapolation to the limit of macroscopic electrodes.

We made use of this implementation in order to investigate two molecules, well studied experimentally: benzene–1,4–di–thiol, and a larger, anthracene–based molecule. Our findings are twofold:

- The experimental conductance is two to three orders of magnitude below the theoretical estimate in agreement with results found in the literature. For the larger molecule, qualitative information on the transport could be gained.
- Changing bond lengths, bond angles, number of contact atoms etc. within reasonable limits does not bring down the theoretical value by orders of magnitude.

Thus we are led to the conclusion that approximations in the exchange–correlation functional may be the major underlying reason for the discrepancy. To this end, we formulated the condition, under which the “standard” approach would be exact, namely if the quasistatic limit of the exact exchange–correlation functional of time–dependent DFT would be used. However, in actual calculations an approximated equilibrium functional is used, e.g., in the local density approximation (LDA). This functional misses several pieces that are not local in the density. In order to demonstrate that the missing terms are important for transport we replaced the Kohn–Sham energies and orbitals from DFT by their counterparts from Hartree-Fock. While we loose correlation effects correcting the resonance energies this way, exchange effects giving rise to non–local terms in a density functional are treated in an exact manner. Indeed, we find that the level broadening, which is vastly overestimated in the “standard” DFT method and responsible for the mispredicted conductance, becomes much more realistic.

At present, better functionals that would include correlation effects, exact exchange and also additional long range terms that originate from genuine non-equilibrium effects are not on the market. Nevertheless, DFT based transport calculations for single molecules can be very useful and in many situations even quantitative results can be obtained. In order to illustrate this, three examples have been investigated in our work.

1. Effects based on symmetry: molecules can be highly symmetric. A particularly interesting situation occurs, when the main current flow through the molecule is right along the intersection line of two mirror planes. In that case, depending on whether or not the current feed into the molecule respects the mirror symmetries, the measured conductance can be strongly different. DFT calculations are perfectly suitable to illustrate this effect. We have studied an appropriate example and indeed obtained a good qualitative agreement with the experimental findings.
2. External parameters: equilibrium DFT allows to monitor the flow of the electron density with external parameters, like a gate voltage. In molecules, strong changes of the density can occur, when the energy of a molecular level driven by an external parametric change passes the Fermi-energy of the leads. The resonance situation implies a large current flow, and therefore oscillations of the conductance with the external parameter can be investigated exactly, even with equilibrium functionals. Again we illustrated this procedure using the paradigm molecule benzene–1,4–di–thiol.
3. Polarization driven shift of energy levels: a non-orthodox application of the same idea is, to study how the single–particle levels shift in en-

ergy when a finite bias is applied. We demonstrated this idea using the “diode” molecule that has been described in the introduction (fig. 1.1). Our method gives a quantitatively correct reproduction of seven out of nine of the lowest lying steps seen in the current voltage characteristics, see fig. 10.18. To the best of our knowledge, this is the first time that a spectral fingerprint of a molecule in a transport experiment has been predicted quantitatively.

## 11.2 Outlook

Being able to predict the peak positions of the molecule of fig. 1.1 is certainly a major theoretical success, but by no means does it imply that we have come much closer to the resolution of the fundamental theoretical problems at hand. In order to calculate the step height (in addition to its position) it is necessary to use improved, i.e., non-local, exchange–correlation functionals. At present, the choice of possible functionals is limited. None of them incorporates all long–range terms that are known to exist and many of them are computationally much more expensive than, e.g., LDA. Therefore, it is at least conceivable that a lot more fundamental work on the front of time–dependent DFT and many–body physics has to be done before fully quantitative calculations with DFT become possible.

Given this somewhat unclear perspective at the DFT front, it seems to be advisable to follow several different paths in parallel in order to make progress in predicting molecular properties in transport measurements:

- Implement those exchange–correlation functionals with long range kernel that are available and compare results among these and with experiments.
- Continue to look for more experimental features in transport that can be understood in terms of equilibrium DFT. Those might include e.g. phonon frequencies, oscillator strengths and electron–phonon couplings.
- Hybrid approaches: try to marry exact methods (like configuration interaction, CC2 etc.) performed for the bare molecule with DFT calculations for the combined system of molecule and leads.

In order to grasp the full picture, a similar amount of work also needs to be done at the experimental front. Taking everything together, it seems fairly plausible that we have to go through a longer process that involves many different contributions made from different fields — conceptual, computational

and experimental — before we arrive at a state in which a systematical design of functional molecular units is possible.

# Appendix A

## The Meir–Wingreen Formula

The Meir–Wingreen formula [65]

$$I = \int dE \operatorname{Tr}(f_L \Gamma_L - f_R \Gamma_R)(\mathbf{G}_C - \mathbf{G}_C^\dagger) + \operatorname{Tr}(\Gamma_L - \Gamma_R) \mathbf{G}_C^< \quad (\text{A.1})$$

connects the retarded (advanced) Green's functions  $\mathbf{G}$  ( $\mathbf{G}^\dagger$ ) and the lesser Green's-function  $\mathbf{G}^<$  of the full many-body problem including the coupling to the leads with the  $dc$ -current  $I$ . These Green's-functions are again defined in the Hilbert space of the *extended molecule*.

$f_{L,R} = f(E - \mu_{L,R})$  denote the Fermi distribution functions for the left/right lead, respectively, which are assumed to be at chemical potentials  $\mu_{R,L}$ .  $\Gamma_{L,R}$  describes the coupling of the molecule to the external leads. The dependence on energy  $E$  has been omitted.

The coupling matrices,  $\Gamma_{L,R}$ , are known from the non-interacting case above, whereas the Green's-functions  $\mathbf{G}_C$  and  $\mathbf{G}_C^<$  are now more complicated due to the included interaction effects. Obtaining these, especially the lesser function  $\mathbf{G}_C^<$ , which is more complicated as it depends on the occupation distribution  $f$ , is difficult.

### Derivation:

The current  $I$  between the left lead and the central cluster follows from the continuity equation as

$$I = \frac{ie}{\hbar} \sum_{m;\alpha=l} (t_{\alpha m} \langle \mathbf{c}_\alpha^\dagger \mathbf{d}_m \rangle - t_{\alpha m}^* \langle \mathbf{d}_m^\dagger \mathbf{c}_\alpha \rangle) \quad (\text{A.2})$$

We transform this using the Keldysh Green’s–function  $G^<(\omega) = i\langle \mathbf{c}_\alpha^\dagger \mathbf{d}_\mathbf{m} \rangle$  (see e.g. [63, 98]) into

$$I = \frac{e}{\hbar} \sum_{\alpha=l} \int_{-\infty}^{\infty} \frac{d\omega}{2\pi} [V_{\alpha,m} G_{m,\alpha}^<(\omega) - V_{\alpha,m}^* G_{\alpha,m}^<(\omega)]. \quad (\text{A.3})$$

As we assume the leads to be non–interacting, we can write down the Dyson–equations for the Keldysh Green’s–functions

$$G_{\alpha,m}^<(\omega) = \sum_n V_{\alpha,n} [g_{\alpha,\alpha}^t(\omega) G_{n,m}^<(\omega) - g_{\alpha,\alpha}^<(\omega) G_{n,m}^{\bar{t}}(\omega)] \quad (\text{A.4})$$

$$G_{m,\alpha}^<(\omega) = \sum_n V_{k\alpha,n}^* [g_{\alpha,\alpha}^<(\omega) G_{m,n}^t(\omega) - g_{\alpha,\alpha}^{\bar{t}}(\omega) G_{m,n}^<(\omega)] \quad (\text{A.5})$$

where we have introduced the time–ordered ( $t$ ) and anti–time–ordered ( $\bar{t}$ ) Green’s–functions and  $G_{n,m}^<(t) = i\langle \mathbf{d}_\mathbf{m}^\dagger \mathbf{d}_\mathbf{n}(t) \rangle$ .

In terms of left–, and right–going scattering states,  $\Psi_n(\mathbf{x}, t)$ , the lesser Green’s–function,  $G_{n,m}^<(t)$ , can be written as

$$\mathbf{G}^<(\mathbf{x}, \mathbf{x}', E) = \sum_{n,\alpha=l,r} \int d(t-t') \Psi_n(\mathbf{x}) \Psi_n^*(\mathbf{x}') f_\alpha e^{iE(t-t')}, \quad (\text{A.6})$$

where the index  $n$ , comprises the quantum numbers describing the states in the left and right lead,  $f_{\alpha=l,r}$  are the Fermi distributions of the respective leads, and  $\mathbf{x} = (\mathbf{x}, t)$ .

Further ingredients required to write down the expression for the current in the desired form are

- The known identities [98]

$$G^>(\omega) + G^<(\omega) = G^t(\omega) + G^{\bar{t}}(\omega) \quad (\text{A.7})$$

$$G^>(\omega) - G^<(\omega) = G^r(\omega) - G^a(\omega) \quad (\text{A.8})$$

- The definition of the unperturbed Keldysh Green’s–functions [98]

$$g_{\alpha,\alpha}^< = 2\pi i f_L(\omega) \delta(\omega - \varepsilon_\alpha) \quad (\text{A.9})$$

$$g_{\alpha,\alpha}^> = -2\pi i [1 - f_L(\omega)] \delta(\omega - \varepsilon_\alpha) \quad (\text{A.10})$$

- The coupling matrices  $\mathbf{\Gamma}_{L,R}$

$$\mathbf{\Gamma}_{L,R}^{n,m} = 2\pi \sum_{\alpha=L,R} \rho_\alpha(E) V_{\alpha,n}(E) V_{\alpha,m}^*(E) \quad (\text{A.11})$$

---

With the density of states  $\rho_\alpha(\varepsilon)$  for a channel  $\alpha$  in the lead we can rewrite the expression for the current to yield

$$I = \frac{ie}{\hbar} \sum_{n,m,\alpha=l} \int d\varepsilon \rho_\alpha(\varepsilon) V_{\alpha,m}(\varepsilon) V_{\alpha,n}^*(\varepsilon) \{f_L(\varepsilon)[G_{m,n}^R(\varepsilon) - G_{m,n}^A(\varepsilon)] + G_{m,n}^<(\varepsilon)\}. \quad (\text{A.12})$$

We can derive an analogous expression for the current between the right lead and the central cluster.

As we assume a steady state, we can symmetrize the two equations to arrive at the final result, the Meir–Wingreen formula for interacting electrons:

$$I = \int dE \text{Tr}(f_L \mathbf{\Gamma}_L - f_R \mathbf{\Gamma}_R)(\mathbf{G}_C - \mathbf{G}_C^\dagger) + \text{Tr}(\mathbf{\Gamma}_L - \mathbf{\Gamma}_R) \mathbf{G}_C^<. \quad (\text{A.13})$$



# List of Figures

1.1	Diode molecule of [1]. . . . .	2
1.2	Diode molecule: I–V characteristics and predicted peak positions	2
2.1	Mechanically controlled break–junction technique . . . . .	9
2.2	Kondo effect in molecules . . . . .	11
2.3	Gated single–molecule contact: electrochemical etching technique	12
2.4	Molecular film devices . . . . .	14
2.5	Repeated formation of junctions using STM . . . . .	15
2.6	Single–molecule device on an STM tip . . . . .	16
2.7	Crossed wire device: schematic representation . . . . .	17
2.8	Nanopore device: setup . . . . .	18
3.1	Schematic representation of a mesoscopic contact . . . . .	20
3.2	Schematic representation of the contact. . . . .	21
3.3	Observation of conductance steps in QPCs. . . . .	24
3.4	Extended molecule as used in our DFT calculations . . . . .	34
3.5	Schematic representation of the coupling. . . . .	37
5.1	Band structure for bulk gold from our DFT calculation . . . . .	71
5.2	Band structure for bulk <i>fcc</i> gold from the ESDB . . . . .	72
5.3	DoS of bulk gold from our DFT calculation . . . . .	73
5.4	4 Atom gold chain with 2 54–atom gold pyramids . . . . .	73

5.5	Transmission of a 4-atom gold chain. Influence of the number of surface atoms . . . . .	75
5.6	Transmission of a 4-atom gold chain. Influence of the cluster size	76
6.1	Relaxed benzene-1,4-di-thiol contact geometry. . . . .	79
6.2	Transmission of benzene-1,4-di-thiol, theoretical calculations . .	80
6.3	Conductance data for benzene-1,4-di-thiol, data by M. Reed. . .	81
6.4	Conductance data for benzene-1,4-di-thiol, data by M. Di Leo .	82
6.5	Conductance data for benzene-1,4-di-thiol, theory. . . . .	83
6.6	Symmetric molecule . . . . .	83
6.7	Conductance data for the symmetric molecule. . . . .	84
6.8	Geometric degrees of freedom of the molecule—gold bond. . . .	86
6.9	Influence of the sulfur-gold distance on conductance . . . . .	87
6.10	Influence of the tilt angle on the conductance . . . . .	88
6.11	Influence of rotation about the molecular symmetry axis on the conductance . . . . .	88
6.12	Influence of a strong distortion in the coupling geometry . . . .	89
6.13	Sulphur-Gold coupling — the <i>thio-acetyl</i> end-group . . . . .	90
6.14	Sulphur-Gold coupling. . . . .	91
6.15	Symmetric molecule . . . . .	92
6.16	Influence of S-Au coupling on conductance. . . . .	93
7.1	Benzene-1,4-di-thiol: Influence of correlation on transport . . . .	97
8.1	Symmetric molecule with sulfur in <i>para</i> position . . . . .	110
8.2	Symmetric molecule with sulfur in <i>meta</i> position . . . . .	111
8.3	Transmission in <i>para</i> and <i>meta</i> coupling . . . . .	112
8.4	HOMO symmetric molecule in <i>para</i> coupling . . . . .	113
8.5	HOMO symmetric molecule in <i>meta</i> coupling . . . . .	114
8.6	Transmission in <i>meta</i> position . . . . .	115

---

8.7	Transmission in <i>para</i> position . . . . .	116
9.1	Gated molecule: level scheme . . . . .	118
9.2	Coulomb diamonds in a single molecule . . . . .	119
9.3	Organic molecules for studying gate effect . . . . .	120
9.4	Gate effect in single molecule . . . . .	121
9.5	Gate electrode . . . . .	122
9.6	Gate electrode: equipotential surface . . . . .	124
9.7	Gate electrode: screening problems . . . . .	125
9.8	Gate electrode: screening properties . . . . .	126
9.9	Gate electrode, geometry used . . . . .	127
9.10	Benzene: shift of the transmission traces. . . . .	128
10.1	Aviram–Ratner diode at zero bias. . . . .	132
10.2	Aviram–Ratner diode under bias. . . . .	133
10.3	Asymmetric and symmetric molecule. . . . .	134
10.4	I–V characteristics: asymmetric molecule . . . . .	135
10.5	Polarizability: asymmetric molecule. . . . .	137
10.6	Polarizability: asymmetric molecule. . . . .	138
10.7	Diode molecule and control molecules. . . . .	139
10.8	Diode molecule: I–V characteristics . . . . .	141
10.9	Control molecules <b>2'</b> , <b>3'</b> : I–V characteristics . . . . .	142
10.10	Diode molecule . . . . .	143
10.11	Diode molecule: LUMO of the separate dots . . . . .	144
10.12	Double dot: zero bias case. . . . .	145
10.13	Double dot: transmitting case. . . . .	145
10.14	Double dot: blocking case. . . . .	146
10.15	Diode molecule: Evolution of the Kohn–Sham energy levels . . . . .	147
10.16	Diode molecule: analysis of the peak positions . . . . .	148

## List of Figures

---

10.17	Diode: comparison of different I-Vs . . . . .	151
10.18	Diode molecule: comparison of theory and experiment . . . . .	152

# Bibliography

- [1] M. Elbing, R. Ochs, M. Koentopp, M. Fischer, C. von Hänisch, F. Weigend, F. Evers, H. Weber, and M. Mayor, A Single-Molecule Diode, Proc. Nat. Acad. Sci. USA (2005), accepted.
- [2] N. Sai, M. Zwolak, G. Vignale, and M. Di Ventra, Non-local corrections to the DFT-LDA electron conductance in nanoscale systems, cond-mat/ , 0411098 (2004).
- [3] H. Kuhn and D. Möbius, Systems of Monomolecular Layers - Assembling and Physico-Chemical Behavior, Angewandte Chemie Int. Ed. **10**, 620 (1971).
- [4] A. Aviram and M. Ratner, Molecular Rectifiers, Chemical Physics Letters **29**, 277 (1974).
- [5] M. Reed, C. Zhou, C. Muller, T. Burgin, and J. Tour, Conductance of a Molecular Junction, Science **278**, 252 (Oct. 1997).
- [6] C. Zhou, C. Muller, M. Deshpande, J. Sleight, and M. Reed, Microfabrication of a mechanically controllable break junction in silicon, Applied Physics Letters **76**(8), 1160 (Aug. 1995).
- [7] J. van Ruitenbeek, A. Alvarez, I. Piñeyro, C. Grahmann, P. Joyez, M. Devoret, D. Esteve, and C. Urbina, Adjustable nanofabricated atomic size contacts, Review of Scientific Instruments **67**(1), 108 (1996).
- [8] C. Muller, J. van Ruitenbeek, and L. de Jongh, Experimental observation of the transition from weak link to tunnel junction, Physica C **191**, 485 (1992).
- [9] E. Scheer, P. Joyez, D. Esteve, C. Urbina, and M. Devoret, Conduction Channel Transmissions of Atomic-Size Aluminum Contacts, Phys. Rev. Lett. **78**(18), 3535 (1997).

- [10] E. Scheer, N. Agrait, J. Cuevas, A. Yeyati, B. Ludolph, A. Mart'in-Rodero, G. Rubio-Bollinger, J. van Ruitenbeek, and C. Urbina, The signature of chemical valence in the electrical conduction through a single-atom contact, *Nature* **394**, 154 (1998).
- [11] J. Reichert, R. Ochs, D. Beckmann, H. Weber, M. Mayor, and H. von Löhneysen, Driving current through single organic molecules, *Physical Review Letters* **88**(17), 176804 (2002).
- [12] H. Weber, J. Reichert, F. Weigend, R. Ochs, D. Beckmann, M. Mayor, R. Ahlrichs, and H. von Löhneysen, Electronic transport through single conjugated molecules, *Chemical Physics* **281**, 113–125 (Oct. 2002).
- [13] M. Mayor, C. von Hänisch, H. Weber, J. Reichert, and D. Beckmann, A trans-Platinum(II) Complex as a Single-Molecule Insulator, *Angw. Chem. Int. Ed.* **41**(7), 1183 (2002).
- [14] C. Kergueris, J.-P. Bourgoin, S. Palacin, D. Esteve, C. Urbina, M. Magoga, and C. Joachim, Electron Transport through a metal-molecule-metal junction, *Physical Review B* **59**, 12505 (May 1999).
- [15] X. Xiao, B. Xu, and N. Tao, Measurement of Single Molecule Conductance: Benzenedithiol and Benzenedimethanethiol, *Nano Lett.* **4**(2), 267 (2004).
- [16] J. Park, A. Pasupathy, J. Goldsmith, C. Chang, Y. Yaish, J. Petta, M. Rinkoski, J. Sethna, H. Abruña, P. McEuen, and D. Ralph, Coulomb blockade and the Kondo effect in single atom transistors, *Nature* **417**, 722 (June 2002).
- [17] R. Smit, Y. Noat, C. Untiedt, N. Lang, M. von Hemert, and J. van Ruitenbeek, Measurement of the conductance of a hydrogen molecule, *Nature* **419**, 906 (Oct. 2002).
- [18] D. Dulić, S. van der Molen, T. Kudernac, H. Jonkman, J. de Jong, T. Bowden, J. van Esch, B. Feringa, and B. van Wees, One-way optoelectronic switching of photochromic molecules on gold, *Physical Review Letters* **91**, 207402 (2003).
- [19] A. Champagne, A. Pasupathy, and D. Ralph, Mechanically-adjustable and electrically-gated single-molecule transistors, *Cond-Mat* , 0409134 (2004).
- [20] H. Park, A. Lim, A. Alivisatos, J. Park, and P. MCEuen, Fabricatio of metallic electrodes with nanometer separation by electromigration, *Applied Physics Letters* **75**(2), 301 (1999).

- [21] W. Liang, M. Shores, M. Bockrath, J. Long, and H. Park, Kondo resonance in a single-molecule transistor, *Nature* **417**, 725 (2002).
- [22] M. Lambert, M. Goffman, J. Bourgoin, and P. Hesto, Fabrication and characterisation of sub-3 nm gaps for single-cluster and single-molecule experiments, *Nanotechnology* **14**, 772 (2003).
- [23] M. Saifullah, T. Ondarçuhu, D. Koltsov, C. Joachim, and M. Welland, A reliable scheme for fabricating sub 5 nm co planar junctions for single molecule electronics, *Nanotechnology* **13**, 659 (2002).
- [24] S. Khondaker and Z. Yao, Fabrication of nanometer-spaced Electrodes using gold nanoparticles, *Applied Physics Letters* **81**(24), 4613 (Dec. 2002).
- [25] Y. Kervennic, D. Vanmaekelbergh, L. Kouwenhoven, and H. Van der Zant, Planar nanocontacts with atomically controlled separation, *Applied Physics Letters* **83**, 3782 (2003).
- [26] Y. Kervennic, J. Thijssen, D. Vanmaekelbergh, R. Dabirian, C. van Walree, L. Jennekens, and H. Van der Zant, Orbital transport in a nanometer long molecular transistor, *Journal of the American Chemical Society* , submitted (2004).
- [27] S. Boussaad and N. Tao, Atom-size gaps and contacts between electrodes fabricated with a self-terminated electrochemical method, *Applied Physics Letters* **80**, 2398 (2002).
- [28] A. Morpurgo, C. Marcus, and D. Robinson, Controlled fabrication of metallic electrodes with atomic separation, *Applied Physics Letters* **74**(14), 2084 (1999).
- [29] G. Philipp, T. Weinmann, M. Hinze, P. Nad Burghard, and J. Weis, Shadow Evaporation Method for Fabrication of sub 10 nm Gaps between Metal Electrodes, *Microelectronic Engineering* **46**, 157–160 (1999).
- [30] C. Lau, D. Steward, R. Williams, and M. Bockrath, Direct Observation of Nanoscale Switching Centers in Metal/Molecule/Metal Structures, *Nano Lett.* **4**(4), 569 (2004).
- [31] X. Cui, A. Primak, X. Zarate, J. Tomfohr, O. Sankey, A. Moore, T. Moore, D. Gust, G. Haris, and S. Lindsay, Reproducible Measurement of Single-Molecule Conductivity, *Science* **294**, 571 (2001).

- [32] L. Patrone, S. Palacin, J. Bougoin, J. Lagoute, T. Zambelli, and S. Gauthier, Direct comparison of the electronic coupling efficiency of sulfur and selenium anchoring groups for molecules adsorbed onto gold electrodes, *Chem. Phys.* **281**, 325–332 (2002).
- [33] Z. Donhauser, B. Mantooth, K. Kelly, L. Bumm, J. Monnell, J. Stapleton, D. Price Jr., A. Rawlett, D. Allara, J. Tour, and P. Weiss, Conductance Switching in Single Molecules Through Conformational Changes, *Science* **292**, 2303 (June 2001).
- [34] S. Lenfant and C. Krzeminski, Molecular rectifying diodes from self-assembly on silicon, *cond-mat*, 0305594 (2003).
- [35] C. Collier, G. Mattersteig, E. Wong, Y. Luo, K. Beverly, J. Sampaio, F. Raymo, J. Stoddart, and J. Heath, A [2]Catenane-Based Solid State Electronically Reconfigurable Switch, *Science* **289**, 1172 (2000).
- [36] A. Ulman, *An Introduction to Ultrathin Organic Films, from Langmuir Blodgett to Self-Assembling*, Academic Press, Boston, 1991.
- [37] A. Ulman, Formation and Structure of Self-Assembled Monolayers, *Chem. Rev.* **96**, 1533 (1996).
- [38] M.-K. Ng and L. Yu, Synthesis of Amphiphilic Conjugated Diblock Oligomers as Molecular Diodes, *Angw. Chem. Int. Ed.* **41**(19), 3598 (2002).
- [39] G. Dholakia, W. Fan, J. Koehne, J. Han, and M. Meyyappan, Topography and Transport Properties of Oligo(phenylene ethylene) Molecular Wires Studied by Scanning Tunneling Microscopy, *J. Nanosci. Nanotech.* **3**, 231 (2003).
- [40] S.-C. Chan, Z. Li, C. Lau, B. Larade, and R. Williams, Investigation of a model molecular-electronic rectifier with an evaporated Ti-metal top contact, *Appl. Phys. Lett.* **83**(15), 3198 (2003).
- [41] L. Bumm, J. Arnold, M. Cygan, T. Dunbar, T. Burgin, L. Jones II, D. Allara, J. Tour, and P. Weiss, Are Single Molecular Wires Conducting?, *Science* **271**, 1705 (1996).
- [42] B. Xu and N. Tao, Measurement of Single-Molecule Resistance by Repeated Formation of Molecular Junctions, *Science* **301**, 1221 (Aug. 2003).
- [43] N. Zhitenev, H. Meng, and Z. Bao, Conductance of small molecular junctions, *Physical Review Letters* **88**(22), 226801 (2002).

- 
- [44] J. Kushmerick, D. Holt, J. Yang, J. Naciri, M. Moore, and R. Shashidhar, Metal-Molecule Contacts and Charge Transport across Monomolecular Layers: Measurement and Theory, *Physical Review Letters* **89**, 086802 (2002).
- [45] J. Kushmerick, D. Holt, S. Pollack, M. Ratner, J. Yang, T. Schull, J. Naciri, M. Moore, and R. Shashidhar, Effect of Bond-Length Alternation in Molecular Wires, *Journal of the American Chemical Society* **124**, 10654 (2002).
- [46] C. Zhou, M. Deshpande, M. Reed, L. Jones II, and J. Tour, Nanoscale metal/self-assembled monolayer/metal heterostructures, *Applied Physics Letters* **71**(5), 611 (1997).
- [47] W. Wang, T. Lee, and M. Reed, Mechanism of electron conduction in self-assembled alkanethiol monolayer devices, *Phys. Rev. B* **68**, 035416 (2003).
- [48] W. Wang, T. Lee, I. Kretzschmar, and M. Reed, Inelastic Electron Tunneling Spectroscopy of an Alkanedithiol Self-Assembled Monolayer, *Nano Lett.* **4**(4), 643 (2004).
- [49] J. Chen, M. Reed, A. Rawlett, and J. Tour, Large On-Off Ratios and Negative Differential Resistance in a Molecular Electronic Device, *Science* **286**, 1550 (1999).
- [50] M. Reed, J. Chen, A. Rawlett, D. Price, and J. Tour, Molecular random access memory cell, *Applied Physics Letters* **78**(23), 3735 (2001).
- [51] J. Chen, W. Wang, M. Reed, A. Rawlett, D. Price, and J. Tour, Room temperature negative differential resistance in nanoscale molecular junctions, *Applied Physics Letters* **77**(8), 1224 (2000).
- [52] J. Chen and M. Reed, Electronic transport of molecular systems, *Chem. Phys.* **281**, 127–145 (april 2002).
- [53] E. Myers, D. Ralph, J. Katine, R. Louie, and R. Buhrman, Current-Induced Switching of Domains in Magnetic Multilayer Devices, *Science* **285**, 867 (1999).
- [54] M. Büttiker, Four-Terminal Phase-Coherent Conductance, *Phys. Rev. Lett.* **57**, 1761 (1986).
- [55] M. Büttiker, Y. Imry, R. Landauer, and S. Pinhas, Generalized many-channel conductance formula with application to small rings, *Phys. Rev. B* **31**(10), 6207 (1985).

- [56] R. Landauer, ., IBM J. Res. Dev. **1**, 233 (1957).
- [57] R. Landauer, Electrical resistance of disordered one-dimensional lattices, Philosophical Magazine **21**, 863 (1970).
- [58] H. Baranger and A. Stone, Electrical linear-response theory in an arbitrary magnetic field: A new Fermi-surface formation, Phys. Rev. B **40**(12), 8169 (1989).
- [59] B. van Wees, H. van Houten, C. Beenakker, J. Williamson, L. Kouwenhoven, D. van der Marel, and C. Foxon, Quantized conductance of point contacts in a two-dimensional electron gas, Phys. Rev. Lett. **60**(9), 848 (1988).
- [60] M. Paulsson, Non Equilibrium Green's Functions for Dummies: Introduction to the One Particle NEGF equations, cond-mat/0210519 (2002).
- [61] M. Paulsson, F. Zahid, and S. Datta, Resistance of a Molecule, cond-mat/0208183 (2002).
- [62] M. Marinov and B. Segev, Analytical properties of scattering amplitudes in one-dimensional quantum theory, J. Phys. A: Math. Gen. **29**, 2839 (1996).
- [63] S. Datta, *Electronic Transport in Mesoscopic Systems*, Cambridge University Press, 1995.
- [64] J. Rammer and H. Smith, Quantum field-theoretical methods in transport theory of metals, Rev. Mod. Phys. **58**(2), 323 (1986).
- [65] Y. Meir and N. Wingreen, Landauer Formula for the Current through an Interacting Electron Region, Phys. Rev. Lett. **68**(16), 2512 (1992).
- [66] P. Damle, A. Gosh, and S. Datta, Unified description of molecular conduction: From molecules to metallic wires, Phys. Rev. B **64**, 201403 (2001).
- [67] M. Brandbyge, J.-L. Mozos, P. Ordejon, J. Taylor, and K. Stokbro, Density-functional method for nonequilibrium electron transport, PRB **65**, 165401 (2002).
- [68] Y. Xue, S. Datta, and M. Ratner, First-Principles Based Matrix-Green's Function Approach to Molecular Electronic Devices: General Formulation, cond-mat/0112136 (2001).
- [69] R. Ahlrichs, M. Br, M. Hser, H. Horn, and C. Klmel, Electronic Structure Calculations on Workstation Computers: The Program System TURBO-MOLE., Chemical Physics Letters **162**, 165 (1989).

- 
- [70] P.-O. Löwdin, Quantum Theory of Many-Particle Systems. II. Study of the Ordinary Hartree-Fock Approximation, *Phys. Rev.* **97**, 1490 (1955).
- [71] A. Williams, P. Feibelman, and N. Lang, Green's-function methods for electronic-structure calculations, *Phys. Rev. B* **26**(10), 5433 (1982).
- [72] J. Heurich, J. Cuevas, W. Wenzel, and G. Schön, Electrical Transport through Single-Molecule Junctions: From Molecular Orbitals to Conduction Channels, *Phys. Rev. Lett.* **88**, 256803 (2002).
- [73] M. Di Ventura, S. Pantelides, and N. Lang, First-Principles Calculation of Transport Properties of a Molecular Device, *Phys. Rev. Lett.* **84**(5), 979 (2000).
- [74] P. Hohenberg and W. Kohn, Inhomogeneous Electron Gas, *Phys. Rev.* **136**(3B), 864 (1964).
- [75] W. Kohn and L. Sham, Self-Consistent Equations Including Exchange and Correlation Effects, *Phys. Rev.* **140**(4A), 1133 (1965).
- [76] W. Kohn, Nobel Lecture: Electronic structure of matter — wave functions and density functionals, *Rev. Mod. Phys.* **71**(5), 1253 (1999).
- [77] R. Dreizler and E. Gross, *Density Functional Theory*, Springer-Verlag, 1990.
- [78] K. Burke, *The ABC of DFT*, <http://dft.rutgers.edu/kieron/beta>, 2004.
- [79] R. Jones and O. Gunnarsson, The density functional formalism, its applications and prospects, *Rev. Mod. Phys.* **61**(3), 689 (1989).
- [80] E. Lieb, *Physics in Natural Philosophy: Essays in Honor of Laszlo Tisza on His 75th Birthday*, MIT, Cambridge, 1982.
- [81] M. Levy, Electron densities in search of Hamiltonians, *Phys. Rev. A* **26**, 1200 (1982).
- [82] U. von Barth and L. Hedin, A local exchange-correlation potential for the spin polarized case, *J. Phys. C* **5**, 1629 (1972).
- [83] J. Perdew and M. Levy, Physical Content of the Exact Kohn-Sham Orbital Energies: Band Gaps and Derivative Discontinuities, *Phys. Rev. Lett.* **51**(20), 1884 (1983).
- [84] J. Perdew, R. Parr, M. Levy, and J. Balduz, Density-Functional Theory for Fractional Particle Number: Derivative Discontinuities of the Energy, *Phys. Rev. Lett.* **49**(23), 1691 (1982).

- [85] K. Eichkorn, O. Treutler, H. Oehm, M. Haeser, and R. Ahlrichs, Auxiliary Basis Sets to Approximate Coulomb Potentials, *Chemical Physics Letters* **242**, 652 (1995).
- [86] E. Davidson and D. Feller, Basis set selection for molecular calculations, *Chem. Rev.* **86**, 681 (1986).
- [87] F. Weigend, F. Furche, and R. Ahlrichs, Gaussian basis sets of quadruple zeta valence quality for atoms H–Kr, *J. Chem. Phys.* **119**(24), 12753 (2003).
- [88] K. Eichkorn, F. Weigend, O. Treutler, , and R. Ahlrichs, Auxiliary basis sets for main row atoms and transition metals and their use to approximate Coulomb potentials., *Theor. Chem. Acc.* **97**, 119 (1997).
- [89] A. Schäfer, H. Horn, and R. Ahlrichs, Fully optimized contracted Gaussian basis sets for atoms Li to Kr, *J. Chem. Phys.* **97**, 2571 (1992).
- [90] A. Schäfer, C. Huber, and R. Ahlrichs, Fully optimized contracted Gaussian basis sets of triple zeta valence quality for atoms Li to Kr, *J. Chem. Phys.* **100**(8), 5829 (1994).
- [91] L. Kleinmann and B. Bylander, Efficacious Form for Model Pseudopotentials, *Phys. Rev. Lett.* **48**, 1425 (1982).
- [92] U. von Barth and C. Gelatt, Validity of the frozen-core approximation and pseudopotential theory for cohesive energy calculations, *Phys. Rev. B* **21**, 2222 (1980).
- [93] D. Ceperley and B. Alder, Ground State of the Electron Gas by a Stochastic Method, *Phys. Rev. Lett.* **45**, 566 (1980).
- [94] J. Perdew and A. Zunger, Self-Interaction correction to density-functional approximations for many-electron systems, *Phys. Rev. B* **23**, 5048 (1981).
- [95] J. A. Pople, Nobel Lecture: Quantum chemical models, *Rev. Mod. Phys.* **71**(5), 1267 (1999).
- [96] G. Onida, L. Reining, and A. Rubio, Electronic excitations: density-functional versus many-body Green’s-function approaches, *Rev. Mod. Phys.* (2002).
- [97] F. Della Sala and A. Görling, Open-shell Localized Hartree-Fock approach for an efficient effective exact-exchange Kohn-Sham treatment of open-shell atoms and molecules, *J. Chem. Phys.* **118**, 10439 (2003).

- 
- [98] G. Mahan, *Many Particle Physics*, Plenum Publishing Corporation, 2000.
- [99] D. Langreth and M. Mehl, Easily Implementable Nonlocal Exchange-Correlation Energy Functional, *Phys. Rev. Lett.* **47**(6), 446 (1981).
- [100] D. Langreth and M. Mehl, Beyond the local-density approximation in calculations of ground-state electronic properties, *Phys. Rev. B.* **28**(4), 1809 (1983).
- [101] J. Perdew, Accurate Density Functional for the Energy: Real-Space Cutoff of the Gradient Expansion for the Exchange Hole, *Phys. Rev. Lett.* **55**, 1665 (1985).
- [102] J. Perdew and W. Yue, Accurate and simple density functional for the electronic exchange energy: Generalized gradient expansion, *Phys. Rev. B* **33**, 8800 (1986).
- [103] J. Perdew, Atoms, molecules, solids, and surfaces: Applications of the generalized gradient approximation for exchange and correlation, *Phys. Rev. B* **46**, 6671 (1992).
- [104] C. Lee, W. Yang, and R. Parr, Development of the Colle-Salvetti correlation-energy formula into a functional of the electron density, *Phys. Rev. B* **37**, 785 (1988).
- [105] A. Becke, Density-functional thermochemistry. III. The role of exact exchange, *J. Chem. Phys.* **98**(7), 1372 (1993).
- [106] A. Becke, Density-functional exchange-energy approximation with correct asymptotic behavior, *Phys. Rev. A* **38**, 3098 (1988).
- [107] J. Perdew, Density-functional approximation for the correlation energy of the inhomogeneous electron gas, *Phys. Rev. B* **33**, 8822 (1986).
- [108] J. Perdew, M. Ernzerhof, and K. Burke, Rationale for Mixing Exact Exchange with Density Functional Approximations, *J. Chem. Phys.* **105**, 9982 (1996).
- [109] J. Perdew, Density-functional approximation for the correlation energy of the inhomogeneous electron gas, *Phys. Rev. B* **33**, 8822 (1986).
- [110] F. Della Sala and A. Goerling, Efficient localized Hartree-Fock methods as effective exact-exchange Kohn-Sham methods for molecules, *J. Chem. Phys.* **115**(13), 5718 (2001).

- [111] F. Della Sala and A. Goerling, The asymptotic region of the Kohn-Sham exchange potential in molecules, *J. Chem. Phys.* **116**(13), 5374 (2002).
- [112] C.-O. Almbladh and U. von Barth, Exact results for the charge and spin densities, exchange–correlation potentials, and density–functional eigenvalues, *Phys. Rev. B* **31**(6), 3231 (1985).
- [113] E. Runge and E. Gross, Density–functional theory for time–dependent systems, *Phys. Rev. Lett.* **52**, 997 (1984).
- [114] N. Maitra, K. Burke, and C. Woodward, Memory in time–dependent density functional theory, *Phys. Rev. Lett.* **89**, 23002 (2002).
- [115] R. van Leeuwen, Causality and Symmetry in Time-Dependent Density-Functional Theory, *Phys. Rev. Lett.* **80**, 1280 (1998).
- [116] N. Maitra and K. Burke, Demonstration of initial state dependence in time–dependent density functional theory, *Phys. Rev. A* **63**, 42501 (2001).
- [117] D. Papconstantopoulos, *Electronic Structure Database* <http://cst-www.nrl.navy.mil/ElectronicStructureDatabase/>, Center for Computational Materials Science (CCMS), Washington, DC, 1999.
- [118] D. Papaconstantopoulos, *Handbook of the band structure of elemental solids*, Plenum Press, New York, 1986.
- [119] A. Yanson, G. Rubio Bollinger, H. van den Brom, N. Agraït, and J. van Ruitenbeek, Formation and manipulation of a metallic wire of single gold atoms, *Nature* **395**, 783 (1998).
- [120] C. Untiedt, A. Yanson, R. Grande, G. Rubio-Bollinger, Agraït, N. Vieira, and J. van Ruitenbeek, Calibration of the length of a chain of single gold atoms, *Physical Review B* **66**(8), 085418 (2002).
- [121] K. Hansen, S. Nielsen, M. Brandbyge, E. Lægsgaard, I. Stensgaard, and F. Besenbacher, Current-voltage curves of gold quantum point contacts revisited, *Applied Physics Letters* **77**(5), 708 (2000).
- [122] G. Rubio-Bollinger, C. de las Heras, E. Bascones, N. Agraït, F. Guinea, and S. Vierira, Single-channel transmission in gold one-atom contacts and chains, *Phys. Rev. B* **67**, 121407(R) (2003).
- [123] H. Mehrez, A. Wlasenko, B. Larade, J. Taylor, P. Grütter, and H. Guo, I-V characteristics and differential conductance fluctuations of Au nanowires, *Phys. Rev. B* **65**, 195419 (2002).

- 
- [124] B. Ludolph, M. Devoret, D. Esteve, C. Urbina, and J. van Ruitenbeek, Evidence for Saturation of Channel Transmission from Conductance Fluctuations in Atomic-Size Point Contacts, *Phys. Rev. Lett.* **82**(7), 1530 (1999).
- [125] R. Smit, C. Untiedt, and J. van Ruitenbeek, The high-bias stability of monatomic chains, *Nanotechnology* **15**, S472 (2003).
- [126] M. Brandbyge, E. Lægsgaard, I. Stensgaard, and F. Besenbacher, Conduction channels at finite bias in single-atom gold contacts, *Phys. Rev. B* **60**(24), 17064 (1999).
- [127] J. Palacios, A. Pérez-Jiménez, E. Louis, E. SanFabián, and J. Vergés, First-principles approach to electrical transport in atomic-scale nanostructures, *Phys. Rev. B* **66**, 035322 (2002).
- [128] H.-W. Lee, H.-S. Sim, D.-H. Kim, and K. Chang, Towards unified understanding of conductance of stretched monoatomic contacts, *Phys. Rev. B* **68**, 75424 (2003).
- [129] M. Di Leo, Stromfluss durch organische Moleküle: Herstellung und Charakterisierung von Einzelmolekülkontakten, Master's thesis, Fachhochschule München, Germany, 2002.
- [130] J. Tour, L. Jones II, L. Pearson, J. Lamba, T. Burgin, G. Whitesides, D. Allara, A. Parikh, and S. Atre, Self-Assembled Monolayers and Multilayers of Conjugated Thiols,  $\alpha,\omega$ -Dithiols, and Thioacetyl-Containing Adsorbates. Understanding Attachments between Potential Molecular Wires and Gold Surfaces, *Journal of the American Chemical Society* **117**(37), 9529–9534 (1995).
- [131] F. Evers, F. Weigend, and M. Koentopp, Coherent transport through a molecular wire: DFT calculation, *Physica E* **18**, 255 (2003).
- [132] F. Evers, F. Weigend, and M. Koentopp, Conductance of molecular wires and transport calculations based on density-functional theory, *Phys. Rev. B* **69**, 235411 (2004).
- [133] J. Stokbro, K. Taylor and M. Brandbyge, Do Aviram–Ratner Diodes Rectify?, *J. Am. Chem. Soc.* **125**, 3674 (2003).
- [134] K. Stokbro, J. Taylor, M. Brandbyge, J.-L. Mozos, and P. Ordejn, Theoretical study of the nonlinear conductance of Di-thiol benzene coupled to Au(1 1 1) surfaces via thiol and thiolate bonds, *Comp. Mat. Sci.* **27**(1-2), 151 (2003).

- [135] P. Damle, T. Rakshit, M. Paulsson, and S. Datta, Current-voltage characteristics of molecular conductors: two versus three terminal, *cond-mat/0206328* (2002).
- [136] Y. Xue and M. Ratner, Microscopic study of electrical transport through individual molecules with metallic contacts: I. "Band" lineup, voltage drop and high-field transport, *cond-mat/0303179* (2003).
- [137] J. Seminario, A. Zacarias, and P. Derosa, Analysis of a dinitro-based molecular device, *J. Chem. Phys.* **116**(4), 1671 (2002).
- [138] S. Pantelides, M. Di Ventra, and N. Lang, First-Principles Simulations of Molecular Electronic, *Ann. N.Y. Acad. Sci.* **960**, 177 (2002).
- [139] J. Wuerfel and R. Ochs, personal communication.
- [140] G. Rubio-Bollinger, S. Bahn, N. Agrait, K. Jacobsen, and S. Vieira, Mechanical Properties and Formation Mechanisms of a Wire of Single Gold Atoms, *Physical Review Letters* **87**(2), 026101 (2001).
- [141] D. Krüger, H. Fuchs, R. Rousseau, D. Marx, and M. Parrinello, Pulling Monatomic Gold Wires with Single Molecules: An Ab Initio Simulation, *Physical Review Letters* **89**, 186402 (2002).
- [142] D. Krüger, R. Rousseau, H. Fuchs, and D. Marx, Towards Mechanochemistry: Mechanically Induced Isomerizations of Thiolate-Gold Clusters, *Angew. Chem. Int. Ed.* **42**, 2251 (2003).
- [143] D. Krüger, H. Fuchs, D. Marx, R. Rousseau, and M. Parrinello, Interaction of short-chain alkane thiols and thiolates with small gold clusters: Adsorption structures and energetics, *J. Chem. Phys.* **115**(10), 4776 (2001).
- [144] H. Sellers, A. Ulman, Y. Shnidman, and J. Eilers, Structure and binding of alkanethiolates on gold and silver surfaces: implications for self-assembled monolayers, *J. Am. Chem. Soc.* **115**, 9389 (1993).
- [145] E. Emberly and G. Kirczenow, Multi-terminal Molecular Wire Systems: A Self-consistent Theory and Computer Simulations of Charging and Transport, *cond-mat/0303179* (2003).
- [146] E. Emberly and G. Kirczenow, Comment on "First-Principles Calculation of Transport Properties of a Molecular Device", *Phys. Rev. Lett.* **87**, 269701 (2001).
- [147] K. Burke, R. Car, and R. Gebauer, Density functional theory of dissipative systems, *cond-mat* **0410352** (2004).

- 
- [148] G. Vignale and W. Kohn, Current-Dependent Exchange-Correlation Potential for Dynamical Linear Response Theory, *Phys. Rev. Lett.* **77**(10), 2037 (1996).
- [149] S. Yaliraki and M. Ratner, Interplay of Topology and Chemical Stability on the Electronic Transport of Molecular Junctions, *Ann. N.Y. Acad. Sci.* **960**, 153 (2002).
- [150] M. Mayor, M. Büschel, K. Fromm, J.-M. Lehn, and J. Daub, Electron Transfer Through Bridging Molecular Structures, *Ann. N.Y. Acad. Sci.* **960**, 16 (2002).
- [151] M. Mayor, H. Weber, J. Reichert, M. Elbing, C. von Hänisch, D. Beckmann, and M. Fischer, Electric Current through a Molecular Rod - Relevance of the Position of the Anchor Groups, *Angewandte Chemie Int. Ed.* **42**(47), 5834 (2003).
- [152] M. Mayor and H. Weber, Molecular Electronics — Integration of Single Molecules in Electronic Circuits, *Chimia* **56**(10), 494 (2002).
- [153] J. Reichert, *Leitfähigkeitsmessungen an einzelnen organischen Molekülen*, PhD thesis, Universität Karlsruhe, Germany, 2003.
- [154] S. Kubatkin, A. Danilov, M. Hjort, J. Cornil, J.-L. Brédas, N. Stuhr-Hansen, P. Hedegård, and T. Bjørnholm, Single-electron transistor of a single organic molecule with access to several redox states, *Nature* **425**, 698 (2003).
- [155] P. Barbara, T. Meyer, and M. Ratner, Contemporary Issues in Electron Transfer Research, *J. Phys. Chem.* **100**, 13148 (1996).
- [156] V. Balzani, *Electron Transfer in Chemistry*, Wiley-VCH, 2001.
- [157] A. Kuznetsov and J. Ulstrup, *in Electron transfer in chemistry and biology*, Wiley, Hamburg, 1996.
- [158] B. Larade and A. Bratkovsky, Current rectification by simple molecular quantum dots: An ab initio study, *Phys. Rev. B* **68**, 235305 (2003).
- [159] J. Kushmerick, C. Whitaker, S. Pollack, T. Schull, and R. Shashidar, Tuning current rectification across molecular junctions, *Nanotechnology* **15**, S489 (2004).
- [160] F. Zahid, A. Ghosh, M. Paulsson, E. Polizzi, and S. Datta, Charging induced asymmetry in molecular conductors, *cond-mat*, 0403401 (2004).
- [161] R. Metzger, Electrical Rectification by a Molecule: The Advent of Unimolecular Electronic Devices, *Acc. Chem. Res.* **32**, 950 (1999).